RUPRECHT-KARLS-UNIVERSITÄT HEIDELBERG

Frank Bigiel

Search for Exclusive Photoproduction of ω-ϕ Vector Meson Pairs at HERA

Diploma Thesis

HD-KIP-04-13

KIRCHHOFF-INSTITUT FÜR PHYSIK

Search for Exclusive Photoproduction of ω-ϕ Vector Meson Pairs at HERA

This diploma thesis has been carried out by Frank Bigiel at the
University of Heidelberg
Kirchhoff-Institut für Physik
Faculty of Physics and Astronomy
under the supervision of
Prof. Dr. Karlheinz Meier

Abstract

Simultaneous exclusive photoproduction of ω- and ϕ-vector mesons at HERA was examined in this analysis. It covers data recorded with the H1 detector from 1996 to 2000 at an average γp center-of-mass energy of 200 GeV. This reaction is a possible signature for Pomeron-Odderon fusion, where the Odderon is the C=P=-1 partner of the Pomeron and is required by non-perturbative QCD.
Several preceding analyses failed to find evidence for Odderon induced reactions, i.e. exclusive photoproduction of π^0- and tensor mesons. One possible explanation is that the coupling of the Odderon to the γ-meson vertex is a lot smaller than assumed. To circumvent this difficulty, the process $\gamma\mathrm{p} \to \omega\phi\mathrm{X}$ was chosen. Here, the above vertex is replaced by the well-known diffractive γ-Pomeron-vector meson vertex. Thus, in this double-diffractive process the Odderon couples in turn to the proton and fuses with the Pomeron at the third vertex to create another vector meson: the ϕ.
The ω-meson has been reconstructed via its decay into photons: $\omega \to \pi^0\gamma \to 3\gamma$, the ϕ-meson via its decay $\phi \to \mathrm{K}^+\mathrm{K}^-$.
Evidence for this process could not be found. Thus, an upper limit on the cross-section, which refers to the limited phase-space expressed in terms of the laboratory frame rapidity Y ($3.8 \leq \mathrm{Y}_\phi \leq -2.7$ and $-1.7 \leq \mathrm{Y}_\omega \leq 1.7$), has been determined. It was found to be $\hat{\sigma}(\gamma\mathrm{p} \to \omega\phi\mathrm{X}) < 107.1\,\mathrm{nb}$ (95% CL).

Zusammenfassung

In dieser Arbeit wurde die gemeinsame exklusive Photoproduktion von ω- und ϕ-Vektor-Mesonen bei HERA untersucht. Die analysierten Daten wurden mit dem H1-Detektor zwischen 1996 und 2000, bei einer mittleren γp-Schwerpunktsenergie von 200 GeV, erfasst. Der untersuchte Prozess stellt eine mögliche Signatur für Pomeron-Odderon-Fusion dar. Das Odderon ist dabei der C=P=-1 Partner des Pomerons und wird im Rahmen nicht-perturbativer QCD-Modelle gefordert.
Vorangegangene Analysen konnten keinen Beleg für Odderon induzierte Reaktionen, d.h. exklusive Photoproduktion von π^0- und Tensormesonen, finden. Eine mögliche Erklärung ist, dass die Kopplung des Odderons an den γ-Meson Vertex erheblich schwächer ist als angenommen. Um dieses Problem zu umgehen, wurde der Prozess $\gamma p \to \omega\phi X$ ausgewählt. Hier wird der oben genannte Vertex durch den wohl bekannten diffraktiven γ-Pomeron-Vektor-Meson Vertex ersetzt. Bei diesem doppelt-diffraktiven Prozess koppelt das Odderon an das Proton und fusioniert mit dem Pomeron an einem dritten Vertex, an dem ein weiteres Vektormeson erzeugt wird: das ϕ.
Das ω-Meson wurde über den Zerfall: $\omega \to \pi^0\gamma \to 3\gamma$ rekonstruiert, das ϕ-Meson über seinen Zerfall $\phi \to \mathrm{K}^+\mathrm{K}^-$.
Es konnte kein Beleg für den oben genannten Prozess gefunden werden. Daher wurde eine obere Grenze für den Wirkungsquerschnitt von $\hat{\sigma}(\gamma\mathrm{p} \to \omega\phi\mathrm{X}) < 107.1\,\mathrm{nb}$ (95% CL) bestimmt. Dieser bezieht sich auf einen begrenzten Phasenraum der in Rapiditätseinheiten im Laborsystem Y ausgedrückt wird ($3.8 \leq \mathrm{Y}_\phi \leq -2.7$ und $-1.7 \leq \mathrm{Y}_\omega \leq 1.7$).

Contents

List of Figures

List of Tables

Introduction

Scattering experiments are approved means in order to develop and evaluate models and theories in elementary particle physics. In order to gain information on the type and the dynamics of the underlying physical processes, the particles that are created in such scattering experiments are examined. The resolution capabilities that are necessary to do so are limited by the provided energy. At the storage ring HERA at DESY, electrons, positrons respectively, and protons are brought to collision at an energy of 27.5 GeV, 820 GeV respectively. This results in a center-of-mass energy of $\approx 300\,\mathrm{MeV}$ which corresponds to a resolution of $10^{-18}\,\mathrm{m}$. This is far below the size of a nucleon.
In this analysis, the electrons will be used as a source for high-energetic photons. A measure for the virtuality is the transferred four-momentum squared Q^2. At $Q^2 \approx 0$, the exchanged photon is quasi-real and the reaction is called photoproduction. The reactions that are examined in this analysis are of such type. In contrast, if a highly virtual photon is exchanged, one speaks of deep inelastic scattering (DIS).
Vector mesons have the same quantum numbers as the photon ($J^{PC} = 1^{--}$). Thus, the photon is able to fluctuate into such and interact hadronically with the proton. In photoproduction one finds diffractive reactions. They are mediated by the exchange of a colorless object named Pomeron. In such reactions, no further particles are produced. The proton can be excited and dissociate into multiple hadrons.
Two theories are able to explain such exclusive vector meson production. A phenomenological description based on Regge-theory and calculations from perturbative QCD[1]. Measurements so far indicate that a transition exists from a regime where Regge-theory makes valid predictions to a regime where QCD does so. This transition depends on two quantities: the mass of the vector meson and the virtuality Q^2 of the exchanged photon. At the very low Q^2 in this analysis, Regge-theory has to be applied.
Regge-theory now demands a 'partner-trajectory' to the Pomeron, named Odderon. In contrast to the Pomeron, this new trajectory has to have P=C=-1. Theory also predicts that the Odderon-trajectory should become visible when comparing total proton-proton- and proton-antiproton-cross-sections to each other, namely in terms of a finite difference between just these two. This hasn't been observed so far at hadron-hadron-colliders and is unlikely to happen in the future, since measuring total cross-sections at large energies is rather difficult and suitable accelerators are not available.
As described above, HERA, as a source of quasi-real photons, offers the possibility to study strong interaction and also search for the Odderon. Unlike the vector

[1] Quantum Chromodynamics

mesons in Pomeron-induced reactions, those induced by the Odderon should lead to exclusive production of tensor- and pseudo-scalar mesons, due to the different C- and P-parity of the Odderon. Analyses of such type have been carried out in the H1-group at the Kirchhoff-Institute for Physics at the University of Heidelberg. These analyses searched for elastic π^0-production (O.Nix [1], T.Golling [2]) and tensor meson-production (C.v.Cube [3], T.Berndt [4]). No evidence of such processes was found though. Upper limits have been determined that disproved theoretical predictions which had been made by theorists O.Nachtmann and H.G.Dosch [5, 6]. One possible explanation is that the coupling of the Odderon to the γ-meson vertex is a lot smaller than assumed [51]. Thus, the idea arose to look for Pomeron-Odderon fusion. One so obtains the well understood 'γ-vector meson-Pomeron' vertex and the Odderon coupling to the proton. By fusion of an Odderon and a Pomeron another vector meson could be created. This led to the present thesis, where the process $\gamma p \to \omega\phi X$ is examined, where X is the scattered proton or its fragments in case of excitation.
The thesis is devided into 5 parts. Chapter 1 deals with the theoretical background. It describes kinematic terminology as well as variables and basic ideas of Regge-theory, where the concepts of Pomeron and Odderon are introduced. Remarks on how strong interaction can be studied at HERA and on the specific event signature close this chapter. The second chapter describes HERA, and in particular the H1 detector with most of its components. Special emphasis is put on the components that were applied for this analysis. Chapter 3 gives an overview on the used Monte Carlo generators before chapter 4 shows in detail how the actual analysis was performed. Starting with the reconstruction of kinematic variables it describes as well detector acceptances and data selection. The last chapter presents the results. This comprises mass- and other control-spectra as well as the determination of an upper limit on the cross-section within a certain fiducial volume in phase-space and some sources for systematic errors.

Chapter 1

Theory

This chapter describes the theoretical basis for this analysis. First off, kinematic variables that will be used throughout the thesis are introduced. Then, the terms 'photoproduction' and 'diffraction' will be explained. Fundamentals of Regge-theory and objects named 'Pomeron' and 'Odderon' are discussed thereafter. Finally is explained, why and how strong interaction can be studied at a lepton-hadron collider, namely HERA. This chapter finishes with introducing the specific event signature.

1.1 Kinematic Variables and Expressions

At HERA, electrons and protons are brought to collision. The electrons thereby emit photons which in turn interact with the proton. In order to describe these scattering processes, those kinematical quantities will be introduced that will be used throughout this analysis. From now on, the natural unit system will be applied, in particular $\hbar = \mathrm{c} = 1$.
Let k be the four-momentum of the incoming electron e and p the four-momentum of the incoming proton P, k' and p' be the four-momenta of the respective outgoing particles[1]. The four-momentum of the virtual photon that is emitted by the electron be defined as q=k-k'. The eP-center-of-mass (cms) energy squared

$$s := (k+p)^2 \approx 4E_e E_P \tag{1.1}$$

is defined by the HERA electron- and proton beam energies. The cms-energy $\sqrt{\mathrm{s}}$ amounts to $\approx 300\,\mathrm{GeV}$ for the period 1996 to 1998. From 1999 to 2000, due to a rise of the proton energy, $\sqrt{\mathrm{s}}$ changed to 318 GeV.
The 'virtuality' of the photon is defined as

$$Q^2 := -q^2 = -(k-k')^2 = 4E_e E'_e cos^2\left(\frac{\Theta'}{2}\right) > 0, \tag{1.2}$$

hence the negative of the four-momentum transfer squared from the electron to the virtual photon. $\Theta' := \measuredangle(\mathrm{k}, \mathrm{k}')$ is the scattering angle of the electron. The term virtuality refers to the fact that for a real photon Q^2 vanishes. Due to the Heisenberg

[1] Primed quantities in this section will always refer to quantities of respective outgoing particles, i.e. after the scattering process.

uncertainty principle, Q^2 is a measure for the resolution power in such a scattering event which is proportional to $\sqrt{1/Q^2}$.
The fraction of the electron energy that is transferred to the proton is called inelasticity and obtained via

$$y := \frac{q \cdot p}{k \cdot p} = 1 - \frac{E'_e}{E_e} sin^2\left(\frac{\Theta'}{2}\right). \tag{1.3}$$

In elastic scattering processes, i.e. if no quantum numbers are exchanged besides energy, momentum and angular momentum, the four-momentum squared at the proton vertex, thus the analog to q^2 at the electron vertex, can be of interest. This variable is defined as

$$t := (p - p')^2 = -2E_P E'_P(1 - cos\Omega'), \tag{1.4}$$

where $\Omega' := \measuredangle(p, p')$ is the angle by which the proton is deflected in the scattering process.
A central quantity to characterize a single particle is the 'rapidity'

$$Y = \frac{1}{2} ln\left(\frac{E + p_z}{E - p_z}\right). \tag{1.5}$$

The momentum component along the proton beam is referred to as p_z. Rapidity can be used to describe the phase space occupied by a particle in one dimension. The entire rapidity range at HERA in the cms is -7 to 7. Rapidity is not Lorentz-invariant, differences are though. This means a rapidity spectrum has the same shape in any other system that is obtained by a Lorentz-boost along the beam-axis. If one lets the ratio m/E or m/p go to zero, an approximation for rapidity is obtained which is called 'pseudo-rapidity' η. In this approximation, the particle's mass is ignored.

$$\eta = \frac{1}{2} ln\left(\frac{p + p_z}{p - p_z}\right) = -ln\, tan\left(\frac{\Theta}{2}\right). \tag{1.6}$$

The advantage of η is that its determination is reduced to an angle measurement. The approximation of Y by means of pseudo-rapidity η gets better, the smaller the ratio m/E becomes.

1.2 Photoproduction

The term photoproduction has been introduced into particle physics a long time before HERA. It referred to reactions, where real photons ($Q^2 = 0\,GeV^2$) are shot at targets. At HERA, as explained in the preceding section, the less the electron is deflected the more the photon virtuality Q^2 approaches 0. The regime of photon virtualities $Q^2 << 1\,GeV^2$ is called photoproduction here. Due to the low virtuality, one also speaks of quasi-real photons.
Thus, HERA allows to examine elastic and diffractive (more in 1.3) photon-proton interactions to study several aspects of strong interaction. In order to characterize this photon-proton system, the variable

$$W^2 := (q + p)^2 = q^2 + 2qp + m_P^2 \tag{1.7}$$

describes the center-of-mass energy in the γp-system. This analysis deals with photoproduction events only.

1.3 Diffraction

The term 'diffraction' which is used in the title of this analysis actually stems from classical optics and denotes bending of light around the edges of an opaque obstacle. Hence, light penetrates into the geometric shadow, and outside the shadow an alternating pattern of bright and dark fringes occurs. Classically, one distinguishes 'Fraunhofer-diffraction', where the incoming light is assumed to be parallel and the image plane is assumed to be at a very large distance compared to the diffractive object. Dropping these assumptions leads to the more general case of 'Fresnel-diffraction', where a general discription is quite challenging mathematically. Intensity distributions for both cases are illustrated in figure 1.1.

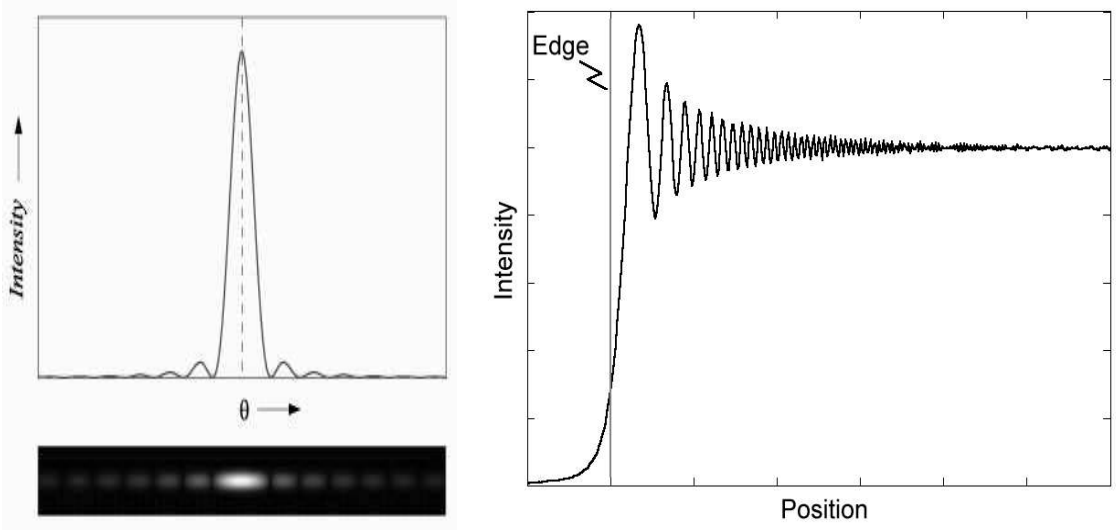

Figure 1.1: *Classical diffraction. The left distribution illustrates Fraunhofer-diffraction at a single slit. The top diagram shows the intensity distribution, the lower picture depicts the diffraction pattern for light, as seen on a screen behind the slit.* Θ *is the azimuthal angle between the slit and the diffraction pattern on the screen. The right plot shows the generalized case of Fresnel-diffraction, that is diffraction at an opaque obstacle, i.e. edge here where the light comes from above. 'Position' denotes the distance qualitatively. The diffraction pattern includes light which penetrates into the geometric shadow (left) and an alternating pattern of bright and dark fringes outside the shadow (right).*

The left plots demonstrate the intensity distribution for Fraunhofer-diffraction at a single slit, the right plot pictures Fresnel-diffraction at an opaque obstacle, i.e. edge in this case. These distributions allow direct conclusions on the structure of the obstacle.
The Fresnel-like distribution has a direct connection to nuclear and particle physics. When going to particles, one has to use suitable variables though. The kinematic

variable t (see equation 1.4) describes the scattering angle between the two protons by means of the four-momentum transfer. The intensity is replaced by the cross-section as a measure for the interaction probability.
When studying the differential cross-section $d\sigma/d|t|$ of elastic nucleon-nucleon scattering or scattering of two nuclei, one finds structures therein that look just like the diffraction pattern in classical optics, due to the wave-nature of the particles. Figure 1.2 shows this angular distribution of the cross-section for the case of proton-proton scattering. The bigger the scattering center is, the steeper is the t dependence of

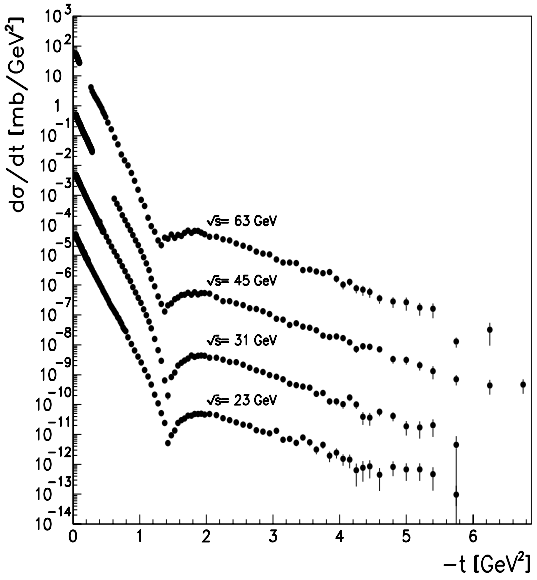

Figure 1.2: *t-spectrum in elastic pp-scattering for different center-of-mass energies. Each curve has been scaled by a factor of* 10^{-2} *with respect to the one above to improve comparability.*

the cross-section and the sharper becomes the diffraction pattern. The similarity of these diffraction patterns to the classical ones is the reason for the naming of such processes in particle- and nuclear physics.
The figure shows how quickly the cross-section drops with t. This is due to the fact that in mainly peripheral elastic scattering only little momentum is transferred between the two protons. Thus, they populate opposite regions of phase-space, e.g. in rapidity. This phenomenon is referred to as 'rapidity-gap' and serves to identify diffractive events. Diffraction in particle physics is actually a synonym for elastic, including quasi-elastic events as well. An event is called quasi-elastic, if one or both of the scattering particles are excited 'diffractively', i.e. the quantum numbers of the excited state are the same as for the ground state. Spin and angular momentum can change though. An example of such diffractive excitement would be $p \rightarrow N^*$, which can actually occur in the process that is examined in this analysis.
Figure 1.3 visualizes diffractive scattering and rapidity-gaps. Shown are graphs and qualitative rapidity distributions for non-dissociative-, i.e. elastic-, single-dissociative- and double-dissociative diffractive events. The more, a typical non-diffractive and non-elastic event is symbolically depicted. Speaking of dissociation

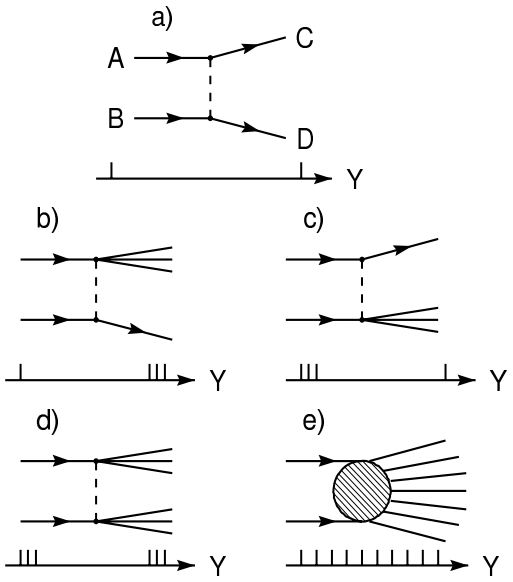

Figure 1.3: *a) to d) show diffractive scatterig processes, whereas e) is neither diffractive nor elastic. Indicated below the respective diagrams is the distribution in rapidity-space which show the occurrence of so-called rapidity gaps. a) is purely elastic, the scattering particles are not excited. b) and c) are called single-dissociative and d) double-dissociative.*

means exciting a particle into a higher mass-state which finally merges into a multi-hadronic final state under conservation of all quantum-numbers.

1.4 Regge-Theory

1.4.1 Fundamentals and the Pomeron

In the particle picture, interactions are described in terms of particle exchanges, namely photons in case of QED[2] and pions in the early Yukawa-theory to describe the interaction between nucleons. These models for strong interaction are often subsumed under the term 'one-particle-exchange' models (OPE).
Exchange of merely one particle is not able to describe all observed phenomena. A new ansatz was made by Tullio Regge [7, 8] in 1959 and G.F. Chew in the 1960's. Regge proposed to treat angular momentum as a continuous complex variable, although physically observable states must clearly have integral or half-integral angular momentum. Chew applied Regge's ideas finally to high energy physics. The path of a scattering amplitude in this plane of complex angular momentum as a function of energy is called a 'Regge-trajectory'.
Regge-theory [9] describes such a scattering process no longer by the exchange of a

[2]Quantum Electrodynamics

single particle, but by the exchange of a set of particles. These particles do all have the same quantum numbers B,S,I,G (baryon number, strangeness, isospin, G-parity) and are part of the Regge-trajectory. Practically, one can think of a hadron-hadron interaction as an exchange of a whole trajectory. This will now be put in a more formal context.
Mathematically, the complex scattering amplitude for a two-particle scattering process can be expanded in partial waves with angular momentum l

$$\Lambda(s,t) = \frac{1}{16\pi}\sum_{l=0}^{\infty}(2l+1)\Lambda_l(s,t)P_l(cos\Theta_t). \tag{1.8}$$

The scattering angle in the cms is expressed by Θ_t, and $P_l(x)$ are the Legendre-polynomials.
Regge-theory shows [13] that for large center-of-mass energies $s \to \infty$ and fixed t this scattering amplitude $\Lambda(s,t)$ goes to

$$\Lambda(s,t) \propto \left(\frac{s}{s_0}\right)^{\alpha(t)}. \tag{1.9}$$

s_0 is a scaling parameter that has been determined experimentally to $\approx 1\,\mathrm{GeV}^2$. The function $\alpha(t)$ is the Regge-trajectory.
If several quantum numbers play a role for a specific interaction, the corresponding trajectories have to be summed over.
There is a pleasant way though to picture these trajectories, namely by projecting them from this sophisticated complex space onto the $J - m^2$-plane, where J is the angular momentum and m denotes the mass. Such a diagram is called a Chew-Frautschi-plot and is shown in figure 1.4. One finds a linear dependence on t for these trajectories. In other words, particles with the same quantum numbers B,S,I,G (see above) are on straight lines in such a plot. These straight lines can be parametrized as

$$\alpha(t) = \alpha_0 + \alpha' t, \tag{1.10}$$

where α_0 denotes the intercept, and α' is the slope of the trajectory. The term Regge-trajectory however is used in either context: when referring to this object in 'Regge-space' as well as for the straight lines in the Chew-Frautschi-plot.
Figure 1.5 visualizes how t becomes positive, i.e. why t can be identified with m^2, in 1.4. If one goes from the s- to the t-channel, the scattering process $ab \to cd$ goes to $b\bar{d} \to c\bar{a}$ in the t-channel. This procedure is called 'crossing' and explains the identification of t with m^2 for the exchanged particle in the t-channel.
In order to derive an expression for the s-dependence of the total cross-section, on has to apply the optical theorem [8]

$$\sigma^{tot} = \frac{1}{s} Im\left(\Lambda(t=0)\right). \tag{1.11}$$

It links the imaginary part of the forward scattering amplitude to the total cross-section. Plugging equation 1.9, the approximation of the scattering amplitude for large energies, into the optical theorem (equation 1.11) gives the desired expression for the total cross-section

$$\sigma^{tot} \propto \left(\frac{s}{s_0}\right)^{\alpha_0 - 1}. \tag{1.12}$$

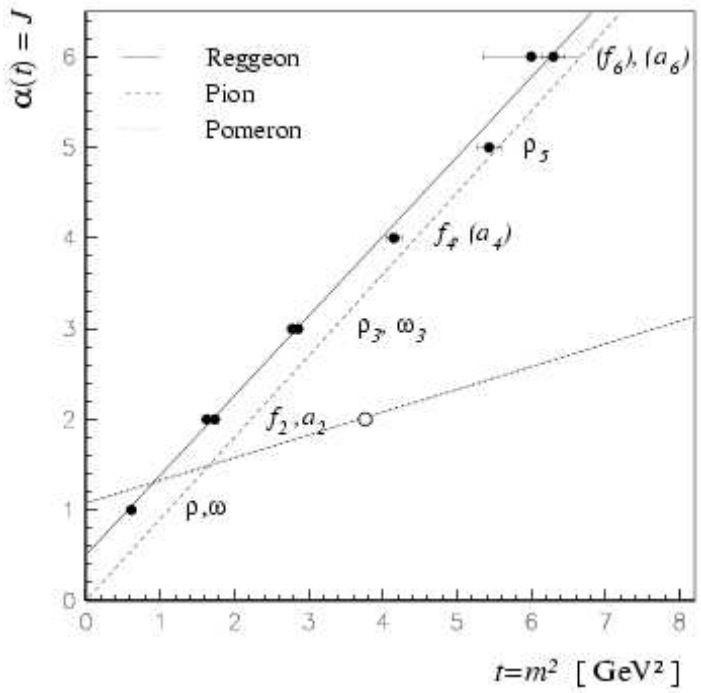

Figure 1.4: *Chew-Frautschi plot. Drawn is the spin J of the particles versus their mass squared. Depicted are the ρ- and ω-, here named Reggeon-, the pion- and the Pomeron-trajectory (see text) as well as a glueball candidate (see text also) thereon. The identification of t with m^2 is explained in the text. α(t) is explained in equation 1.10.*

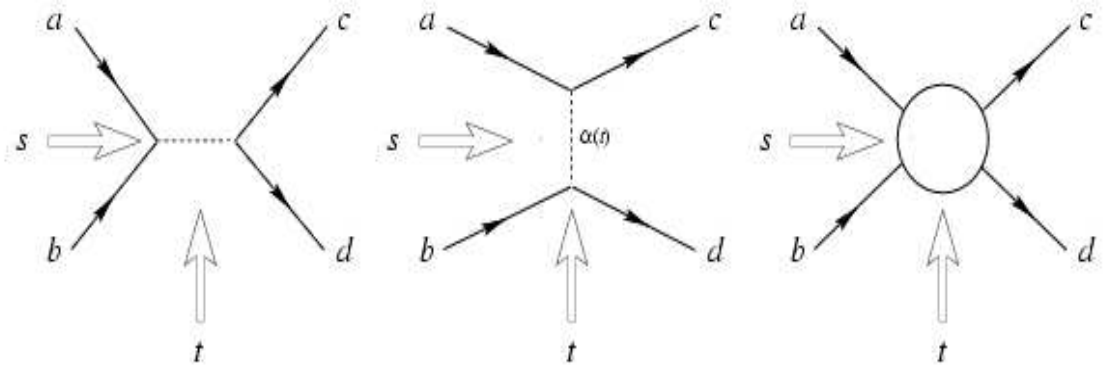

a) b) c)

Figure 1.5: *Possible hadron-hadron interaction types characterized via the Mandelstam-variables s and t. a) shows the process $a + b \rightarrow c + d$ in the so-called s-channel, where an intermediate state is created. b) shows the same process in the t-channel where a particle, a trajectory respectively, is exchanged. c) shows the scattering process in general.*

This holds for the case that only one tajectory is exchanged. Otherwise, the contributions of all participating trajectories have to be summed up.
The elastic cross-section is also provided by [8] and holds again for s $\rightarrow \infty$:

$$\frac{d\sigma^{el}}{d|t|} \propto \frac{|\Lambda(s,t)|^2}{s^2} = F(t) \left(\frac{s}{s_0}\right)^{2\alpha(t)-2} . \tag{1.13}$$

F(t) can however not be predicted by theory. Experimental measurements show for most hadronic cross-sections an exponential decrease with |t| though. Concludingly one obtains a bold maximum at t $\approx$ 0 which corresponds to scattering under small angles. One therefore calls this the 'forward peak'.
Assuming now an exponential dependence for F(t), namely $F(t) = e^{b_0 t}$, equation 1.13 turns into

$$\frac{d\sigma^{el}}{d|t|} = \left.\frac{d\sigma^{el}}{d|t|}\right|_{t=0} e^{bt}, \tag{1.14}$$

with the slope parameter $b := 2(b_0 + \alpha' \ln(s/s_0))$. The increase of b with the center-of-mass energy is referred to as 'shrinkage', as the 'forward peak' gets narrower with increasing energy. This has been measured for instance in [10].
Considering the total cross-section in equation 1.12 again, one sees that in case several trajectories are exchanged, the one with the largest intercept at t=0 dominates the cross-section for s $\rightarrow \infty$. The Regge-trajectories of all known particles have an intercept $\alpha(0) < 1$. Even the trajectories with the largest known intercept, therefore called 'leading trajectory', the ρ- and the ω-trajectory, which cannot be distinguished within the experimental precision, have an intercept of ≈ 0.5 (see figure 1.4).
This leads to a problem, as an intercept smaller than one implies a decrease of the total hadronic cross-section with the center-of-mass energy. Experimentally one observes a slight increase however, as shown in figures 1.6 and 1.7.
In order to explain this experimental result, an additional trajectory was postulated named 'Pomeranchuk[3]-trajectory' or 'Pomeron' with an intercept $\alpha(0) = 1+\epsilon, \epsilon > 0$ and a slope $\alpha' = 0.25$. The Pomeron carries the quantum numbers of the vacuum, namely Q=B=S=I=0 and P=C=+1. As the Pomeron has per definition the largest intercept of all trajectories (see figure 1.4), it will be the dominant exchange mechanism for diffractive events for s $\rightarrow \infty$.
Donnachie and Landshoff [11] combined all meson-trajectories to one universal trajectory. Under the assumption that interactions can be described by only the universal- and the Pomeranchuk-trajectory, they obtained from their fits to the data an intercept for the Pomeron of $\alpha_P(0) = 1.0808$.
Until today, there haven't been found any particles that lie on the Pomeranchuk-trajectory. 'Glueballs' would be expected to lie on this trajectory though. Glueballs are colorless bound states of two or more gluons. One glueball candidate with a mass of 1.9 GeV and J=2 [12], which has been measured by the WA91-collaboration, is indicated in figure 1.4.

[3]Named after the Russian physicist Isaak Jakowlewich Pomeranchuk

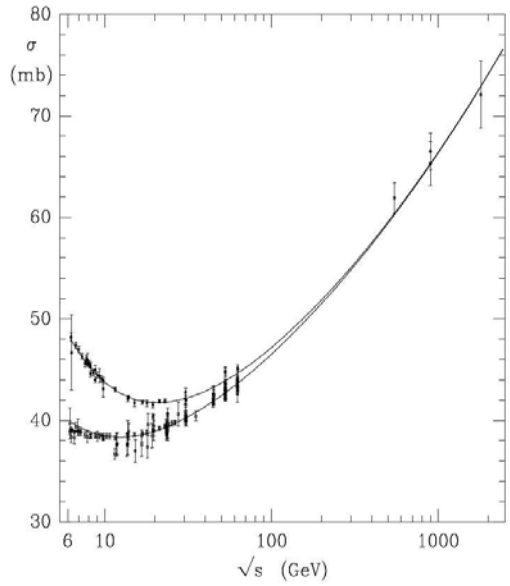

Figure 1.6: *Total pp- and $\overline{p}p$-cross-section with applied fits. The upper curve represents the $\overline{p}p$-cross-section, the lower curve the respective pp one. An increasing cross-section with increasing center-of-mass energy $\sqrt{s}$ is evident for both cases.*

1.4.2 The Odderon

When considering pp- and $\overline{\text{p}}$p-cross-sections as shown in figures 1.6 or 1.7, one finds that both cross-sections get close to each other with increasing center-of-mass energy. In fact, within the huge error bars they are identical at high energies.

It is first of all easily understandable that there are differences between both cross-sections for low and medium energies, since the $\overline{\text{p}}$p-case allows annihilation in the s-channel. This leads to a higher total cross-section for $\overline{\text{p}}$p-collisions. The higher the center-of-mass energy gets though, the more unlikely annihilation gets due to the 1/s-dependence. The so-called 'Pomerantschuk-theorem' [13] now states that the difference between these cross-sections vanishes asymptotically with increasing center-of-mass energies:

$$\lim_{s\to\infty} (\sigma_{tot}(pp) - \sigma_{tot}(\overline{p}p)) \to 0.$$

To put this again in a more formal context, a short interlude on further elements from Regge-theory is necessary.

Every trajectory, meson-trajectories as well as the Pomerantschuk-trajectory, is assigned a sign called 'signature' which depends on the C-parity of the trajectory. In case the signature of the exchanged trajectory is negative, the corresponding scattering amplitude changes sign when going from pp- to $\overline{\text{p}}$p-scattering.

The pomeron-trajectory (C=+1) has a positive signature. Consequently, the scattering amplitude does not flip sign when going from pp- to $\overline{\text{p}}$p-scattering. It contributes thus equally to either cross-section.

Two theorists finally, Lukaszuk and Nicolescu [14], postulated the existence of a

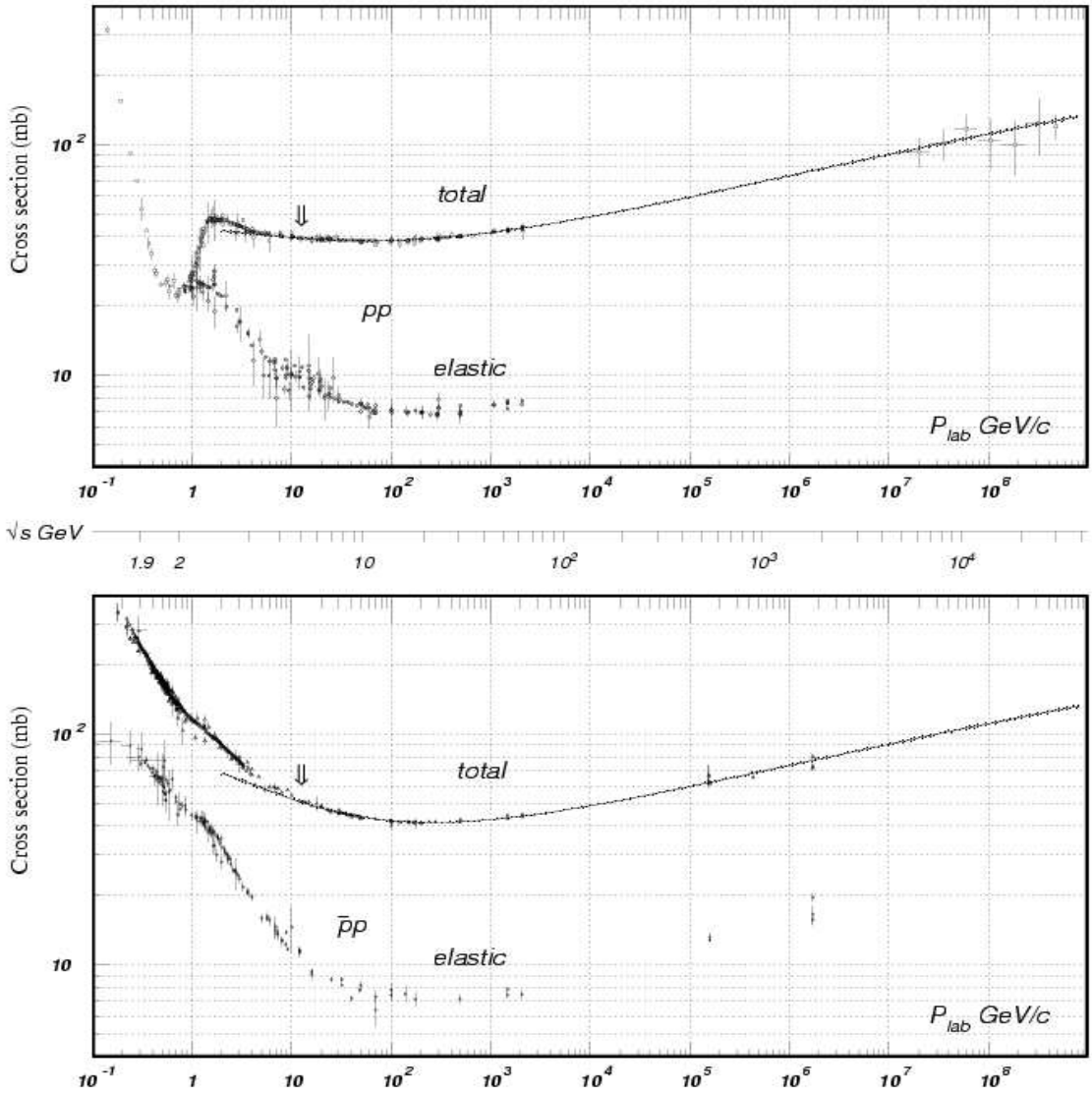

Figure 1.7: *Total pp- (upper plot) and $\overline{p}p$ (lower plot)-cross-section with applied fits. The significant rise in the $\overline{p}p$-cross-section with decreasing energy at low energies comes from annihilation in the s-channel.*

C=P=-1 trajectory, the so-called 'Odderon[4]-trajectory', or just 'Odderon'. It is expected to have the same slope and intercept as the Pomeron, and it is also demanded by non-perturbative QCD.
Like for the Pomeranchuk-trajectory, glueballs could also be candidates for particles on the Odderon-trajectory. In contrast to the Pomeron, these glueballs have to comprise three or more gluons in this case.
The Odderon has C=-1, in contrast to the Pomeron. This leads to a negative signature and finally to a flip of the sign of the scattering amplitude when going from pp- to $\overline{\mathrm{p}}$p-scattering. Thus, the Odderon contributes differently to both processes and a finite difference for $\sigma_{\mathrm{tot}}(\mathrm{pp}) - \sigma_{\mathrm{tot}}(\overline{\mathrm{p}}\mathrm{p})$ would so be expected which contradicts the Pomeranchuk-theorem. Considering figure 1.7 though, differences of the two cross-sections at large energies are not evident. One also recognizes that tiny differences would be drowned in the errors.
HERA offers now another possibilty to search for evidence of the Odderon. Why it is possible at all to study strong interaction at HERA and what kind of events one has to look for there will be discussed in detail in the following chapter.
The idea is, however, that after introducing the Pomeron and the Odderon, besides processes where just one of these is exchanged, one can also think of processes where two Pomerons, two Odderons or one Pomeron and one Odderon are emitted and merge in one interaction and thereby create another particle. Since both do not carry quantum numbers besides energy, momentum and angular momentum, the particles that could be created so are defined by considering the respective C-parities. Concrete examples for such combinations, along with the corresponding C-parities, as well as the specific signature this analysis deals with are presented in detail in the following chapter, section 1.6. How one can determine a cross-section for such double-diffractive processes in principal is presented in 3.1.

1.5 Strong Interactions at HERA

As discussed in the preceding paragraphs, it might even not be possible at all to find evidence for the Odderon at hadron-hadron-accelerators. This section now describes the alternative possibilities HERA offers to circumvent these problems. First, the next subsection answers the question why it is possible after all to study strong interactions at a lepton-hadron-collider. The next part of this chapter then briefly describes a speciality about HERA that has to be considered for cross-section determinations.

1.5.1 The 'Hadronic Photon'

Photoproduction processes in photon-hadron scattering show strong analogy to hadron-hadron scattering. Thus, one also speaks of the 'hadronic photon'. This indicates that the photon can be considered as a superposition of an electromagnetic field with a hadronic component. More precisely, this superposition consists of an electromagnetic, a lepton-antilepton-, a quark-antiquark- and their bound states,

[4]Odd-under-crossing-Pomeron

namely mesons. In quantum-mechanical notation, this could be expressed qualitatively via

$$|\gamma\rangle = |\gamma_{electromagnetic}\rangle + |\gamma_{l\bar{l}}\rangle + |\gamma_{q\bar{q}}\rangle + |\gamma_{meson}\rangle. \tag{1.15}$$

The index electromagnetic refers to the point-like photon interacting only electromagnetically, $l\bar{l}$ refers to a lepton-antilepton pair, $q\bar{q}$ stands for quark-antiquark respectively. All quantum numbers of this hadronic component $|\gamma_{\text{hadronic}}\rangle$ must now match the respective quantum numbers of the photon, i.e. Q=B=S=0, $J^{PC} = 1^{--}$. For the group of mesons, this leaves only the vector mesons, like e.g. ρ^0, ω, ϕ, J/ψ. As the lepton-antilepton-pairs can only interact electromagnetically and weakly, and as the non-bound quark-antiquark pairs have shorter lifetimes than the bound meson-states, both only contribute marginally to the γp-cross-section.
Hence, the so-called Vector Meson-Dominance-Model (VDM) (see [15] for further explanations) describes the hadronic component of the photon in terms of a superposition of all neutral vectormesons, namely

$$|\gamma\rangle = N|\gamma_{electromagnetic}\rangle + \sum_V \frac{e}{\gamma_V}|V\rangle. \tag{1.16}$$

Here, N serves scaling reasons, e denotes the elementary charge and $|V\rangle$ stands for the neutral vector mesons in quantum mechanical notation whose coupling constants are the $1/\gamma_V$.
One can picture the process $\gamma p \rightarrow Vp$ as the photon fluctuating into a vector meson and being elastically scattered on the proton during a certain time interval which is given by the uncertainty principle. The virtual vector meson can merge into a real vector meson by exchanging a Pomeron, i.e. by exchanging energy and momentum to lift the virtual particle onto the mass-shell. The cross-sections for some exemplary processes of such kind are shown in figure 1.8. Figure 1.9 provides a schematic overview.
Figure 1.8 shows as well that the ρ-cross-section itself already contributes roughly 10% to the total cross-section for photoproduction. The significantly steep energy dependence of the J/ψ-meson is interpreted as, due to the big mass of this meson, leaving the regime of soft hadronic interactions and thereby also leaving the regime where Regge-theory is applicable.

1.5.2 The Connection between ep- and γp-Cross-Sections

As described in the preceding subsection, at low scattering angles the electron can be seen as a source of quasi-real photons. Furthermore was described, how the actual interaction takes place between this photon and the proton. This subsection now describes the factors that come into play when connecting the γp-cross-section to the ep-cross-section.
For photoproduction (low Q^2), it can be assumed that all photons are polarized transversely and the photons can be treated as quasi-real. In this case, the connection between the two cross-sections is given as [17]

$$\frac{d^2\sigma_{ep}}{dydQ^2} = \frac{d^2 f_{\gamma/e}}{dydQ^2}\,\sigma_{\gamma p}, \tag{1.17}$$

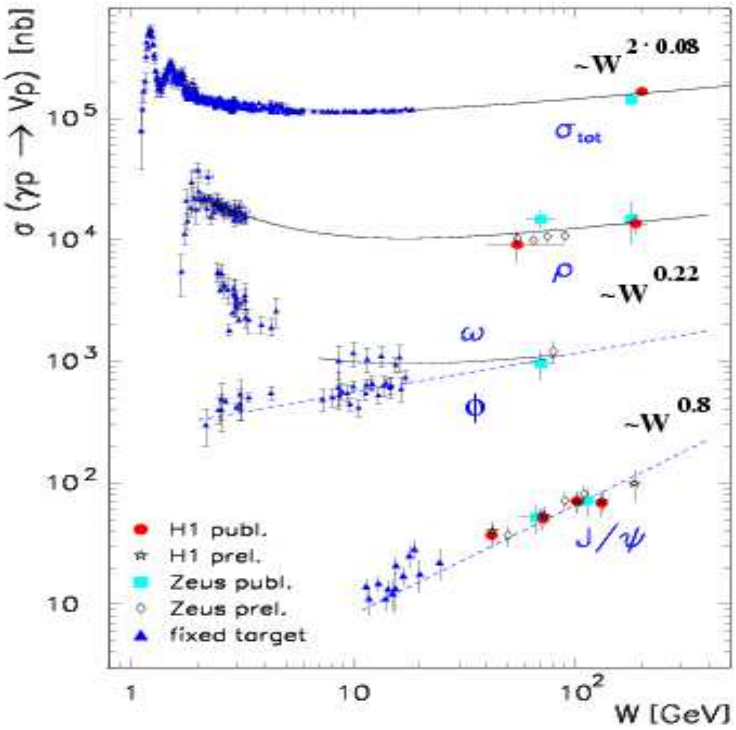

Figure 1.8: *Cross-sections for elastic photoproduction of vector mesons and applied fits as well as the total cross-section. W denotes the center-of-mass energy in the γp-system. These are reactions of the type $\gamma p \to Vp$, where a Pomeron is exchanged between the vectormeson and the proton. Diagram from [16].*

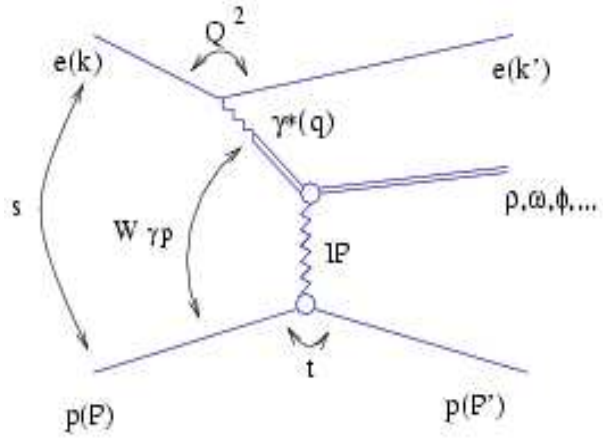

Figure 1.9: *Schematic diagram of vector meson production. The virtual vectormeson merges, under exchange of a Pomeron with the proton, into a real vector meson.*

where $f_{\gamma/e}$ is the so-called photon flux-factor, or 'equivalent photon-flux'. This factor describes the probability that the electron emits a photon with Q^2 and $y \approx E_\gamma/E_e$. The so-called 'Weizsäcker-Williams-Approximation' (WWA), and a more precise modern recalculation shown in [18]-[20], deliver for this flux-factor

$$\frac{d^2 f_{\gamma/e}}{dydQ^2} = \frac{\alpha_{em}}{2\pi y Q^2}\left(1 + (1-y)^2 - 2(1-y)\frac{Q^2_{min}}{Q^2}\right). \tag{1.18}$$

$Q^2_{min}(y) = m_e^2 \frac{y^2}{1-y}$ hereby denominates the kinematically smallest photon virtuality at given y, and α_{em} is the fine-structure constant.
The integral over the kinematic regime for this analysis, i.e. $0.3 < y < 0.7$ and $Q^2 < 0.01\,\mathrm{GeV}^2$, yields for the photon flux-factor

$$F_{\gamma/e} = \int_0^{0.01}\int_{0.3}^{0.7} \frac{d^2 f_{\gamma/e}}{dydQ^2} dydQ^2 = 0.0136. \tag{1.19}$$

1.6 Event Signature

This section deals with some properties of the ϕ-vector meson, the quasi-real photon which is emitted by the electron fluctuates into, as well as the concrete signature of the events that have been searched for in this analysis.

1.6.1 Properties of the ϕ-Meson

With a mass of 1.0195 GeV, the ϕ-meson is just above the $s\bar{s}$-threshold. It is reconstructed via its dominant decay into two charged kaons

$$\phi \longrightarrow K^+K^-. \tag{1.20}$$

The mass of the kaons sums up to $2 \cdot m_{K^+-} \approx 988\,\mathrm{MeV}$. Hence, the mass difference

meson	quark constituents	mass [MeV]	lifetime [s]	decay width [MeV]	dominant decay channels	branching ratio
ϕ	$s\bar{s}$	1019.46	$15 \cdot 10^{-21}$	4.3	K^+K^-	49.2%
					$K^0_L K^0_S$	33.7%
					$\rho\pi + \pi^+\pi^-\pi^0$	15.5%
K^+	$u\bar{s}$	493.68	$12.38 \cdot 10^{-9}$		$\mu^+\nu_\mu$	63.4%
					$\pi^+\pi^0$	21.1%
					$\pi^+\pi^+\pi^-$	5.58%

Table 1.1: *Properties of the ϕ- and K^+-meson, including dominant decay channels and branching ratios. The same numbers and respective decays hold for the K^-. Positive charges are then replaced by negative ones. Data taken from [42].*

between twice the kaon- and the phi-mass yields

$$m_\phi - 2 \cdot m_{K^{+-}} \approx 32\,\text{MeV}.$$

This small difference implies that the decay-kaons have rather small average momenta of $\approx 127\,\text{MeV}$ [42] in the rest frame of the ϕ, which leaves only little phase-space the decay kaons can populate. Accordingly, the natural width of the ϕ is small, namely 4.3 MeV (see 1.1).

1.6.2 The ω-ϕ Signature

The decay-channel which is used to identify the ϕ-meson has been discussed in detail in the preceding subsection, namely two kaon-tracks. The entire signal this analysis searches for consists of more. An ω-meson is demanded, too.
As already indicated in the introduction of this thesis, the coupling of the Odderon to the photon-vector meson-vertex could be a lot smaller than assumed [51]. In order to bypass this undesired vertex, one can go to 'double-diffractive' processes and look for Pomeron-Odderon fusion. The reaction of choice is $\gamma p \to \omega\phi X$, where X is the scattered proton or its fragments in case of excitation, as the above vertex is replaced by the well-known diffractive vertex γ-Pomeron-vector meson. The Odderon couples in turn to the proton and fuses with the Pomeron at a third vertex where also vector mesons could be created. Figure 1.10 displays this process.

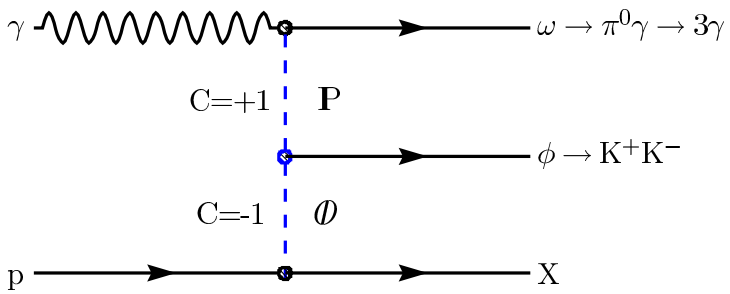

Figure 1.10: *The ω-ϕ event signature.*

The reason why this very process has been chosen to look for evidence for the Odderon in double-diffraction is its clear signature. Altogether, one looks for three photons from the ω-meson, two tracks from the decay-kaons from the ϕ-meson, and the scattered electron in the electron tagger at 33 m. The latter condition ensures that all events are in the desired kinematic regime of $Q^2 < 0.01\,\text{GeV}^2$, i.e. photoproduction (see 1.2 and 4.7.2 for detailed explanations). The decay of the ω-meson into three photons immediately reflects the C-parity of the ω. Technically, the CJC (see 2.2.2) is used to detect the tracks, and the SpaCal (see 2.2.3) is used to detect the three photons.
Figure 1.11 shows additional double-diffractive processes. The possible combinations of mesons at the backward and the central vertex are listed in the table. The type of meson that can be obtained at a vertex is fixed by considering the respective C-parities.

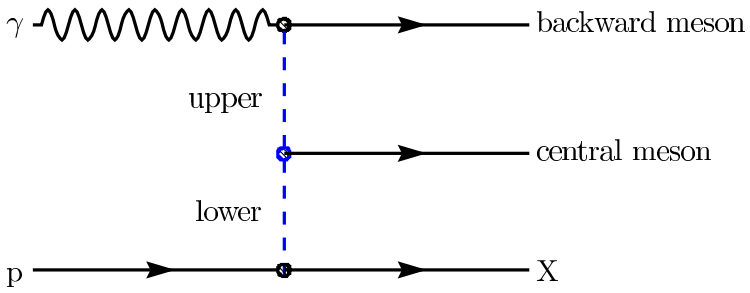

upper vertex	lower vertex	backward meson	central meson
$I\!P$	$I\!P$	$C = -1 : \rho^0, \omega, \phi, \ldots$	$C = +1 : f_0, f_2, \ldots$
$I\!R$	$I\!P$	$C = +1 : \pi^0, \eta, \eta', \eta_c, f_2, a_2, \ldots$	$C = -1 : \omega, \phi, \ldots$
$\boxed{I\!P}$	$\boxed{I\!R}$	$\boxed{C = -1 : \rho^0, \omega, \phi, \ldots}$	$\boxed{C = -1 : \omega, \phi, \ldots}$
$I\!R$	$I\!R$	$C = +1 : \pi^0, \eta, \eta', \eta_c, f_2, a_2, \ldots$	$C = +1 : f_0, f_2, \ldots$

Figure 1.11: *Other possible double-diffractive events. The possible combinations of backward and central mesons are indicated in the table. Depending on the exchanged trajectory, Pomeron or Odderon respectivley, the C-parity defines what kind of mesons are obtained at the vertices. The marked row in the table represents the Pomeron and Odderon exchanges as they are in the event signature this analysis looks for.*

What such a signal would look like in the H1 detector is shown in figure 1.12. The event was generated with the ToyGen event generator [35]. One finds in this figure the above described event signature, namely two central tracks and three 'clusters' in the calorimeter SpaCal.

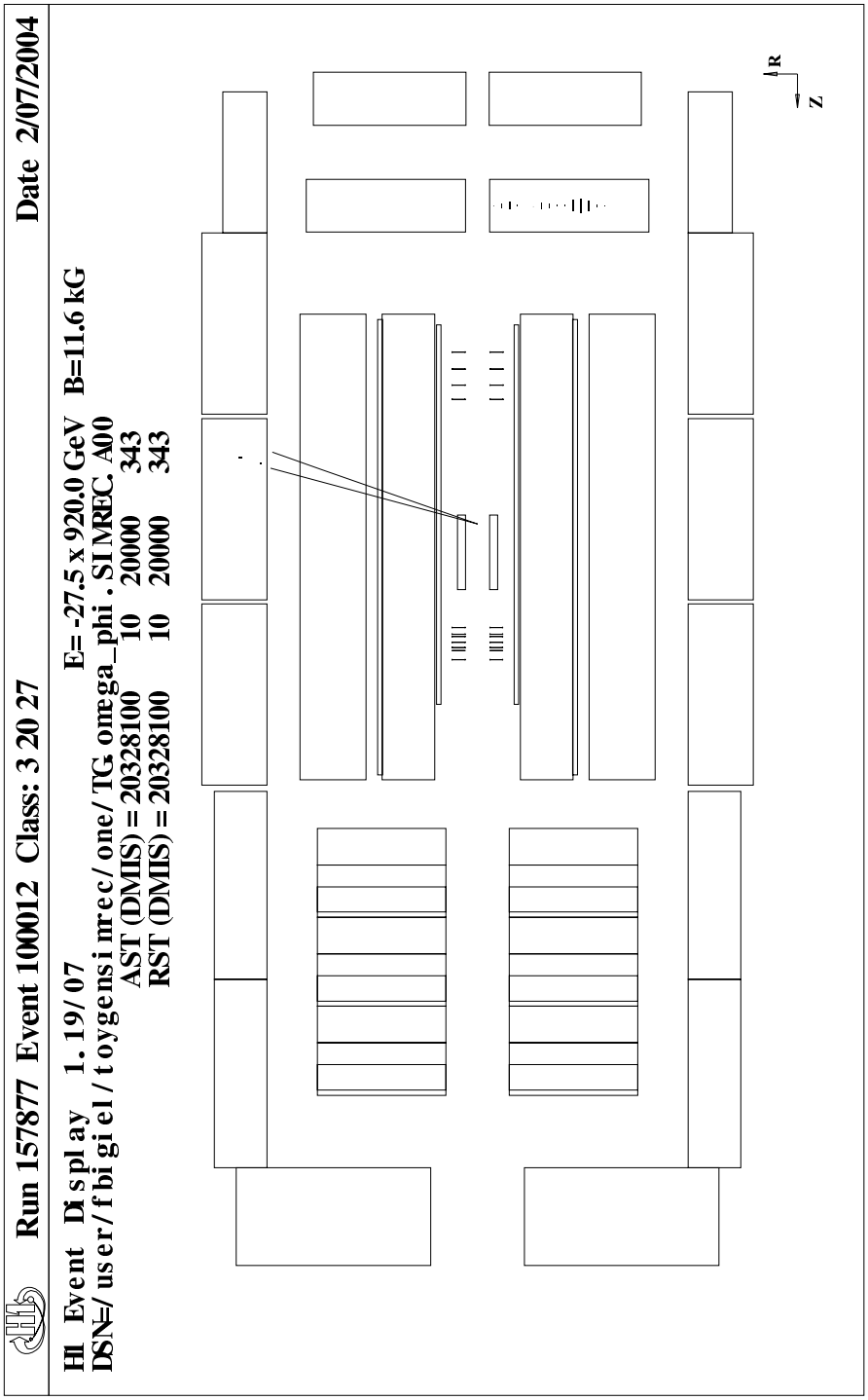

Figure 1.12: *Exemplary event in the H1 detector. One clearly recognizes the two narrow tracks from the kaons in the central trackers and deposited energy in the SpaCal calorimeter. The energy distribution in the SpaCal can vaguely be separated visually into three 'clusters', one from each photon that belongs to the final state of the decayed ω-meson. The specific detector components are explained in figure 2.3.*

Chapter 2

The HERA Accelerator and the H1 Detector

2.1 The Electron-Proton Storage Ring HERA

HERA[1] [21] is the only collider worldwide where electrons[2] and protons are brought to collision (figure 2.1). This happens at a center-of-mass energy of 301 GeV. The ad-

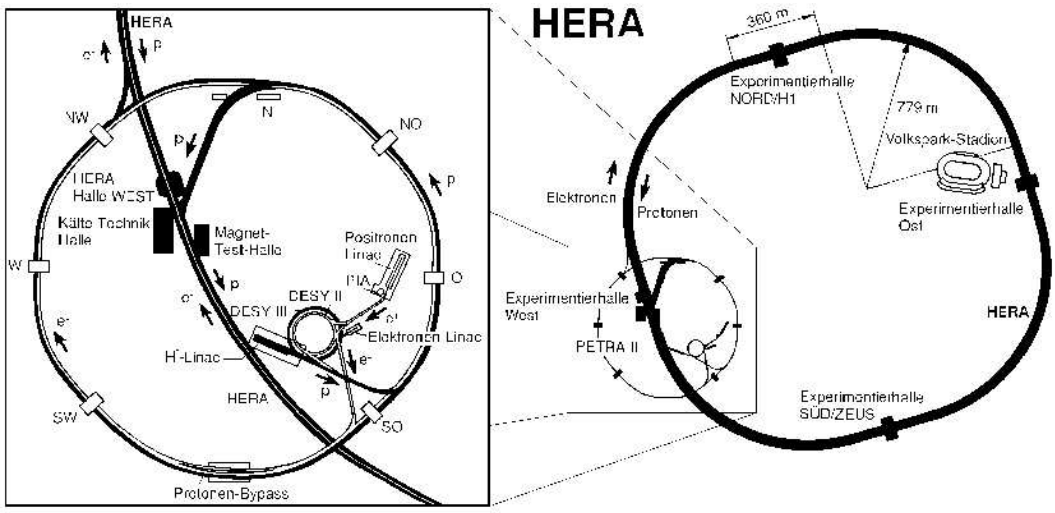

Figure 2.1: *The HERA storage ring facility and its pre-accelerators*

vantage of the colliding-beam technique is evident: A fixed-target experiment where accelerated electrons hit protons at rest could only operate at this center-of-mass energy with an electron beam-energy of 50.6 TeV. At HERA, a proton beam-energy of 820 GeV[3] and an electron beam-energy of 27.5 GeV are sufficient.

[1]Hadron-Elektron-Ring-Anlage. In the following, the situation before the upgrade in 2000 will be described.

[2]From 1994 to 1997 and from 1999 to 2000: e^+. From 1998 to 1999: e^-. The term electron will be used from now on, referring to both, e^+ and e^-.

[3]Raised to 920 GeV in 1998.

HERA is the main collider at DESY[4]. Its construction was finished in 1991 and HERA has been in operation since. It consists of two independent parallel storage rings, both placed in a tunnel with a circumference of 6.3 km and 10-25 m below ground level.
Figure 2.1 also shows the various pre-accelerators. Electrons coming from a linear accelerator LINAC at energies of ≈ 450 MeV are accelerated up to 7.5 GeV in DESY II and then stored in PETRA II. After gathering 60 electron bunches together, they are accelerated to 12 GeV and then injected into the electron-ring. The free protons are obtained by shooting negatively charged hydrogen ions at an energy of 50 MeV onto a thin foil which strips off the electrons. The remaining protons are accelerated up to 7.5 GeV in DESY III and to 40 GeV in PETRA II before being injected into the proton-ring. Only by the time that HERA is completely filled, main acceleration will be started. The particles do not come in a continuous beam though. They are injected in bunches containing 10^{10} to 10^{11} particles each. The bunches are accelerated in the straight line sections (see figure 2.1). To keep the particles on track when moving through the curves, superconducting magnets are needed for the protons with a magnetic field of up to 4.5 T. For the electrons, conventional dipole magnets with a magnetic field of 0.17 T serve the purpose. Finally, 220 bunches, where only 180 of them are filled with particles, are spread over the ring, following one another with a delay of 96 ns. This corresponds to an interaction rate of ≈ 10 MHz at the interaction points. The extensions of the bunches are $\sigma_x \approx 280\,\mu$m, $\sigma_y \approx 60\,\mu$m, and $\sigma_z \approx 1$ cm for electrons and $\sigma_x \approx 180\,\mu$m, $\sigma_y \approx 60\,\mu$m and $\sigma_z \approx 11$ cm for protons.
In order to keep the rate of interactions of the beam particles with gas residues inside the pipe at the lowest level possible, a high vacuum is maintained constantly ($\approx 10^{-9}$ hPa). The limiting factor for the beam energies in case of the protons is the magnetic field of the superconducting deviation magnets. The electrons' beam energy is limited due to synchrotron radiation. The energy loss can be determined to 150 MeV per particle per circulation. 13 MW radio-frequency cavity-resonators are used to counteract. To be able to determine the influence of beam-gas interactions, 'pilot-bunches' are injected regularly. They do not have corresponding bunches to collide with and thus serve to estimate the above effects.
Three experiments are being run at HERA. The fixed-target experiment HERMES uses the electron beam to examine the spin-structure of the proton. ZEUS and H1 work as colliding-beam experiments. Both mainly examine the structure of the proton.
HERA-B used to be another fixed-target experiment and was shut down in 2003. It was designed to study CP-violation in the neutral B-meson system.

2.2 The H1 Detector

A sketch of the H1 detector is shown in figure 2.2. Its mass amounts to 2800 t at a size of $12 \times 10 \times 15\,\mathrm{m}^3$. The electrons enter from the left and are defined to travel

[4]Deutsches Elektronen-Synchrotron

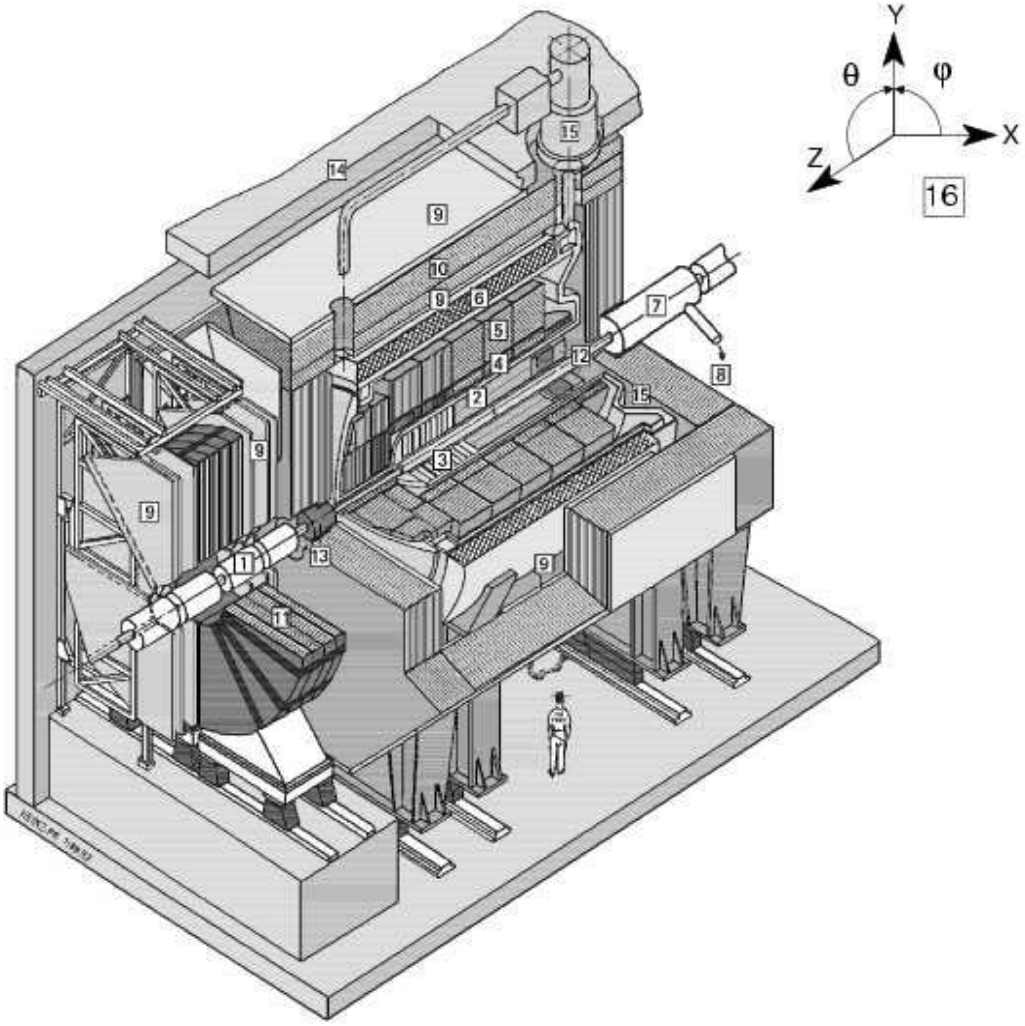

1 Beam pipe and beam magnets
2 Central track detectors
3 Forward track detectors
4 Electromagnetic LAr calorimeter
5 Hadronic LAr calorimeter
6 Superconducting coil (1.15 T)
7 Compensating magnet
8 Helium supply for 7
9 Muon chambers
10 Instrumented iron yoke
11 Forward muon toroid
12 SPACAL and Backward DC
13 Plug calorimeter
14 Concrete shielding
15 Liquid argon cryostat
16 H1 coordinate system

Figure 2.2: *The H1 detector and its components*

in backward direction. The protons consequently move in forward direction from right to left and define the positive z-axis of the H1 coordinate system. The positive x-axis points toward the center of the accelerator ring, whereas the positive y-axis points upwards, out of the plane defined by the HERA ring. The polar scattering angle Θ is measured with respect to the forward direction (see [16], figure 2.2). The interaction point is located nearby the origin of the coordinate system (see small mark near [2]).
In order to get the most complete picture possible of the observed ep-interaction, the H1 detector is equipped with a wide variety of different components (more than a dozen), surrounding the interaction point in multiple layers. The tracking system hereby forms the innermost part. For charged particles, the track curvature, due to an applied magnetic field, allows to measure the particles' momenta. The next outer layer are the calorimeters. They measure the particles' energy deposition. Particles penetrating all these inner parts (basicly muons) are dealt with in the outermost area: The central muon system. As the beam energies from electrons and protons differ greatly, the center-of-mass system is boosted in forward direction. Therefore, the detector is equipped with additional devices in forward direction. Following up, an overview of most of the detector components will be presented. Only the most relevant parts to the analysis will be dealt with in greater detail. For a complete discription of the detector see [22] and [23].

2.2.1 Time-of-Flight Measurement

The time-of-flight system (ToF) consists of a number of scintillators. In backward direction, they are situated in the end caps of the return yoke and in forward direction they are located close to the beam pipe. The SpaCal calorimeter contributes with time-of-flight information, too. The system's purpose is to get rid of background events, i.e. beam-gas and beam-wall interactions that happen outside of the detector. Particles originating in such background processes usually have a different arrival time than those coming from the interaction point inside the detector. The HERA clock delivers precise information at what exact time a bunch-crossing took place. Time-of-flight measurement allows to decide whether or not certain events lie within a pre-defined time-window and thus are accepted, or whether they are assumed to be background and get rejected.
The forward-ToF (also called 'Plug'-ToF) is situated at $z = +7\,\mathrm{m}$ and $z = +5.3\,\mathrm{m}$ whereas the backward-ToF is located at $z = -3.2\,\mathrm{m}$. Furthermore, 'veto-walls' are installed at $z = -6.5\,m$ and $z = -8.1\,m$. Since these components have a time resolution of 1 ns, they can clearly verify an event being within or outside of a defined time-window, as the time between two bunch-crossings is 96 ns.

2.2.2 The Tracking Detectors

The tracking devices make up the innermost part of the detector. Their purpose is reconstruction of tracks, determination of vertices, measurement of particles' momenta and their identification. Moreover, some tracking components are used for triggering.

To obtain a curvature for the tracks of scattered particles, which is vital to deter-

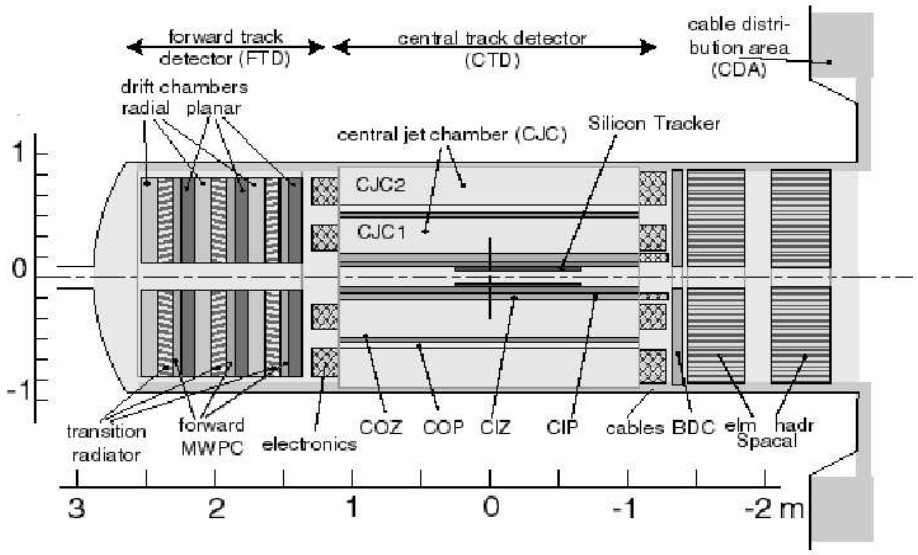

Figure 2.3: *y-z-view of H1's tracking devices*

mining the transverse momenta p_t and the charge sign, a magnetic field is applied in z-direction. It is created by a solenoid with a length of 5.75 m and a diameter of 6.08 m. The homogeneous magnetic field amounts to 1.15 T. The tracking system is devided into a forward, central and a backward part. The locations of the tracking devices are illustrated in figure 2.3. Only the central part has been made use of in this analysis.

Central Trackers

In order to reconstruct centrally produced tracks ($20° < \Theta < 160°$) four drift chambers are available. They are located concentrically around the beam pipe. The major task is carried out by the two central jet chambers (CJC1 and CJC2). At a length of 2.2 m, they consist of 2640 signal wires arranged parallel to the beam pipe. CJC1 is made of 30 cells with 24 signal wires each, CJC2 consists of 60 cells, carrying 32 wires each. The drift cells are tilted by 30° against the radial direction. This is illustrated in figure 2.4. Thus, the ionisation electrons drift perpendicularly to the tracks. This improves track resolution and reduces ambiguities. A spatial resolution of 170 μm in the x-y-plane (equivalent to $r - \varphi$-plane) can be achieved. The z-component can also be measured via charge separation with an accuracy of 2 cm.
When penetrating the chamber gas, energy deposition can be measured with a precision of $\sigma_{dE/dx} \approx 7\%$ which allows particle identification. This 'dE/dx-measurement' determines the energy deposition per length of charged particles via ionisation.
To improve spatial resolution in the z-direction, two other thin drift chambers are adapted to the inside, respectively to the outside of CJC1: CIZ and COZ. Their

wires run perpendicularly with respect to the pipe. The afterall z-resolution can thus be improved to 260 μm. The overall momentum resolution for all four chambers results in $\sigma(p_t)/p_t < 0.01\, p_t/\text{GeV}$.

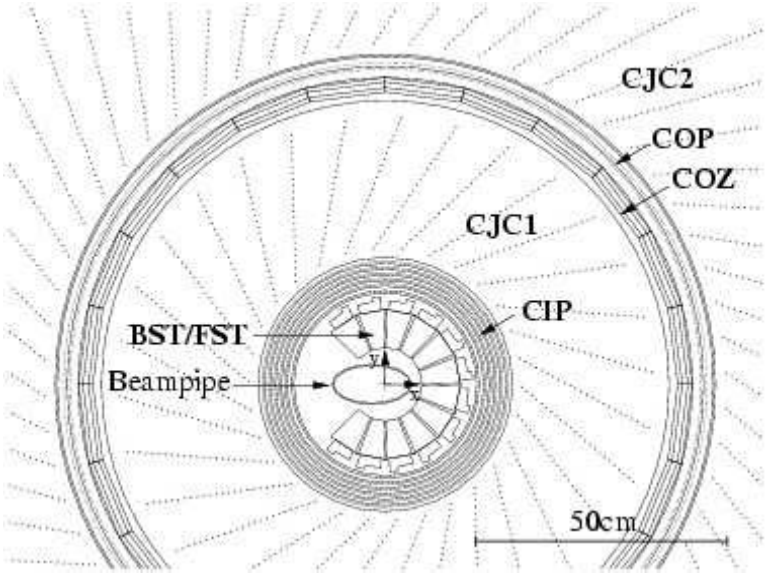

Figure 2.4: *r-φ-view of the central trackers*

Central Proportional Chambers

Furthermore, multi-wire proportional chambers (MWPC) are available. Their purpose is to deliver a fast tracking signal which is necessary for the first level trigger to come to fast decisions. The inner chamber CIP neighbours CIZ on the inside, whereas the outer chamber COP resides inbetween the COZ and CJC2. CIP and COP consist of 60, respectively 18 sections along the z-axis, and 16 sectors in φ (azimuth). The signal is delivered with a time resolution of 21 ns which is far less than the 96 ns interval between two bunch-crossings.

Additional Devices

Tracking devices are also available in forward direction ($5° < \Theta < 25°$), consisting of drift chambers, proportional chambers (FPC) and transition radiation detectors. In backward direction, the BDC (backward drift chamber) supports track detection. Also two silicon trackers are avilable at H1: The Central Silicon Tracker (CST) since 1996 and the Backward Silicon Tracker (BST) since 1998. They improve resolving the actual interaction position. As neither one of the above devices was used in this analysis, further description is omitted here (see [22] for further details).

2.2.3 Calorimeters

Calorimeters serve to measure the energy and to some extent also the position of a particle. In order to examine electromagnetically and hadronically interacting particles, they mostly consist of two parts: An electromagnetic part in the front, i.e. closer to the vertex, and a hadronic part in the back. This is necessary as the hadronic interaction length is much bigger than the electromagnetic radiation length in the same material. An illustration of the available calorimeters at H1 is given in figure 2.5.

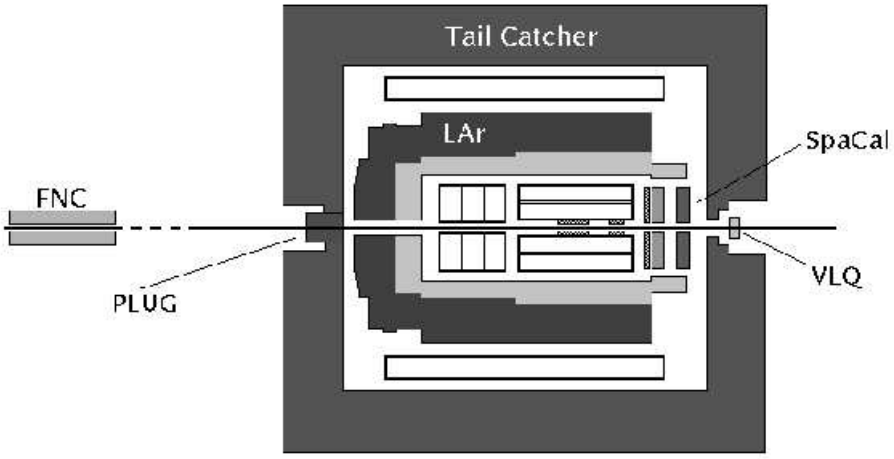

Figure 2.5: *Schematic overview of the H1 calorimeters*

The Liquid Argon Calorimeter

The main calorimeter of H1 is the Liquid Argon Calorimeter (LAr). It covers the angular region $4° < \Theta < 153°$ (pseudo-rapidity range $-1.4 < \eta < 3.6$, see equation 1.6) and consists of absorber plates and liquid argon as the active material. As indicated above, the LAr consists of two major parts to obtain precise results for the energy of electron, photons or hadronic jets: An inner electromagnetic part(4 in figure 2.2) and an outer hadronic part (5). The electromagnetic part consists of alternating 2.4 mm layers of lead plates as absorber material and the liquid argon. This part so corresponds to 20-30 radiation lengths and the electromagnetic relative energy resolution is $\sigma_{\mathrm{E}}/\mathrm{E}=11\%/\sqrt{E/GeV}$. In the hadronic part, the lead plates are replaced with plates of stainless steel. The hadronic energy resolution amounts to $\sigma_{\mathrm{E}}/\mathrm{E}=50\%/\sqrt{E/GeV}$. Altogether, the LAr has a depth of 4.5-7 interaction lengths.

The Backward Calorimeter SpaCal

The SpaCal[5] (12 in figure 2.2) is crucial to this analysis. It is used here to identify ω-mesons in a 3γ final state, i.e. to detect photons (also see 1.6). Its position in the detector is indicated in figure 2.6.

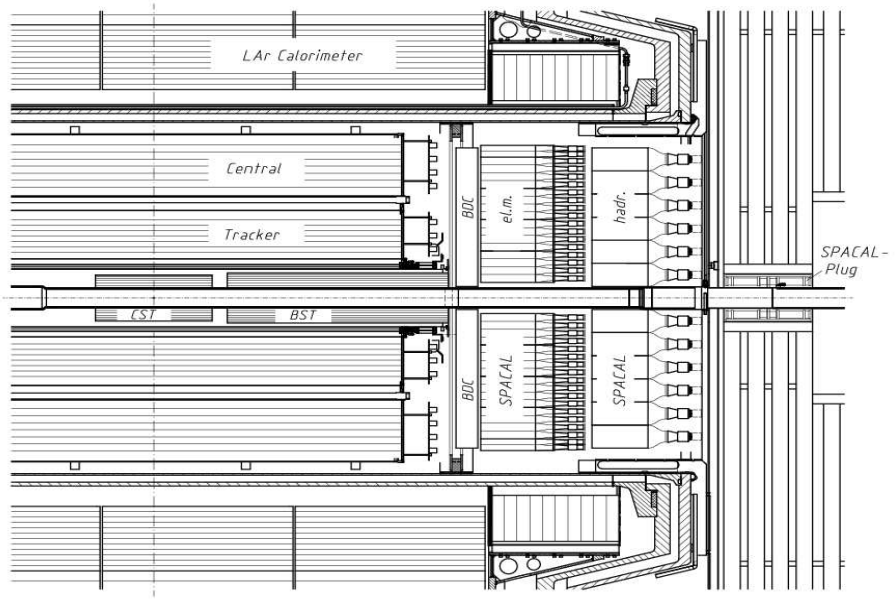

Figure 2.6: *Side view of the detector's backward section*

With a diameter of 160 cm, the SpaCal consists of lead absorbers and scintillating fibres and covers the backward angular region $155° < \Theta < 178°$ ($-3.82 < \eta < -1.42$). This calorimeter consists also of an electromagnetic section with a depth of 28 radiation lengths, followed by a hadronic part. Altogether, the calorimeter is two interaction lengths deep. A major difference between these two parts is the ratio lead-to-fibre: it is higher for the hadronic part. The more, segmentation is a lot finer for the electromagnetic part. This section, which is the important one for this analysis as mentioned above, consists of 1192 cells, $4 \times 4\,\mathrm{cm}^2$ each. Each cell is read out through its own photo-multiplier. The hadronic part is made up of 128 cells, $12 \times 12\,\mathrm{cm}$ each. This cell-structure is illustrated in figure 2.7.
The relative energy resolution for the electromagnetic part is $\sigma_\mathrm{E}/\mathrm{E} \approx 7\%/\sqrt{\mathrm{E/GeV}}$ [24, 25], and the relative uncertainty of the energy scale is 4% for energies between 0.2 GeV and 10 GeV, decreasing to 1% for larger energies. The spatial resolution can be determined to $\sigma(\mathrm{x,y}) = 4.4\mathrm{mm}/\sqrt{\mathrm{E/GeV}}$ [26]. For the hadronic part, the relative energy resolution amounts to $\sigma_\mathrm{E}/\mathrm{E} \approx 56\%/\sqrt{\mathrm{E/GeV}}$ [24, 25]. Moreover, the SpaCal capabilities also include time-of-flight measurements, as its time resolution is as good as 1 ns (for further information on the time-of-flight systems refer to 2.2.1).

Figure 2.8 illustrates the excellent spatial- and energy-resolution abilities of this calorimeter. Displayed is the invariant $\gamma\gamma$-mass spectrum. The invariant mass of

[5] 'Spaghetti Calorimeter'

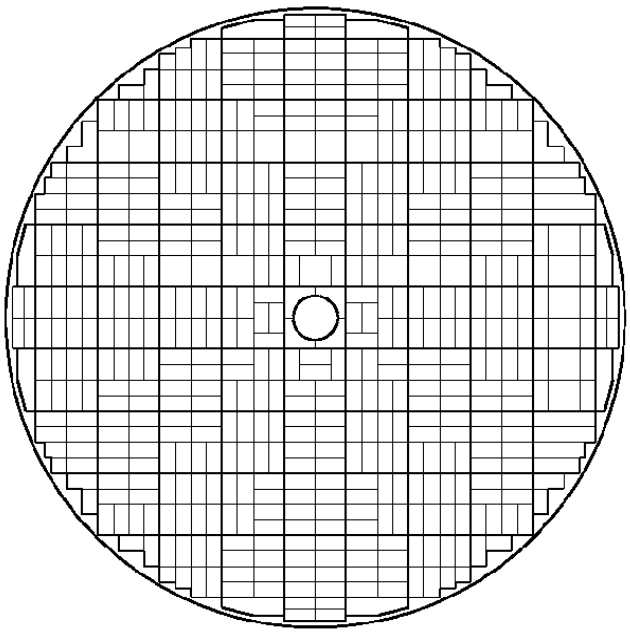

Figure 2.7: *r-φ-view of the electromagnetic part of the SpaCal. Individual cells, equipped with one photo-multiplier each, are merged together to build two-cell structures (thin lines). Eight two cell-structures make up 16-cell 'modules' (thick lines).*

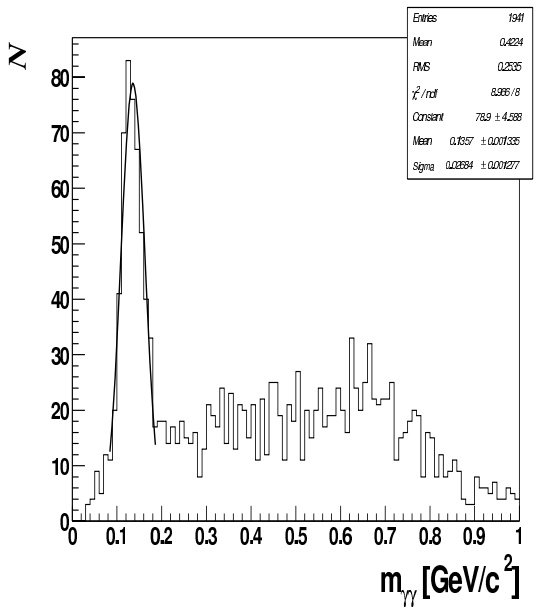

Figure 2.8: *Invariant $\gamma\gamma$-mass spectrum measured with the SpaCal. A Gaussian fit is applied to the π^0-peak.*

two photons is obtained by adding and squaring their four-momenta. They are reconstructed via their energy deposition in the electromagnetic part of SpaCal ('clusters'). The π^0-meson can clearly be recognized with almost no background. The applied Gaussian fit delivers a mass resolution of $\approx 0.027\,\text{GeV}$ (see fit parameters in figure 2.8). This resolution documents the extraordinary measurement capabilities of the SpaCal.

Further Calorimeters

Two other calorimeters complete the angular and particle coverage at H1: the Forward Neutron Calorimeter (FNC) at z=+107m. Just like the SpaCal, the FNC is built of layers of lead and scintillating fibres. Its purpose is to detect high energetic neutrons in forward direction which leave the interaction region under very small angles.
The second calorimeter is the so-called 'Plug' sampling calorimeter. It closes the gap inbetween the LAr and the beam pipe in forward direction in order to minimize loss of particles at very small polar angles.

2.2.4 Muon Systems and the Forward Section

The central muon system is shown in [10]. Inside the iron yoke, guiding back the magnetic flux from the solenoid, plastic streamer chambers can be found organized in four major components. Altogether, they cover a range of $4° < \Theta < 175°$. This allows detection of muons with energies larger than 1.2 GeV. To complete the central muon system, there are three further drift chambers ([9]) available, forming the outermost detection system of the central part of the H1 detector. Another three of these muon chambers reside down the very front, just outside the toroidal magnet [11]. Concerning muon detection, the forward section is completed by another device: The Forward Muon Detectors FMD. The main purpose of this forward muon spectrometer [27] is to measure the momentum of high energetic muons (p>5 GeV) from collision events. It therefore sits just outside the massive iron yoke.
The forward section does not merely consist of muon systems though. One of the numerous other components is the PRT (Proton Remnant Tagger), situated at z=+26m. It measures hadrons from the proton remnants at $0.06° < \Theta < 0.25°$ ($5.1 < \eta < 7$) and comprises seven double-layers of plastic scintillators, each one shielded with lead, working in coincidence. For further details, see [28].
In order to enable H1 to detect protons under rather small angles ($\approx 3\,\text{mrad}$), the Forward Proton Spectrometer (FPS) was installed. Its four[6] components, the 'Roman Pots', are located at z=63, 80, 81 and 90m.
Another purpose of detector components with acceptances reaching down to rather small polar angles is to distinguish between elastic and proton-dissociative events.

[6]Since 1997. Before, only the pots at 81m and 90m were available.

2.2.5 The Luminosity System

The luminosity $\mathcal{L}$ is defined via

$$N = \sigma \int \mathcal{L}(t)\, dt = \sigma\, L. \tag{2.1}$$

The number of events is denoted with N, σ is the interaction cross-section and L is the integrated luminosity. The luminosity $\mathcal{L}$ so connects the rate of interactions with a cross-section. By picking a process with a precisely known cross-section and measuring the rate of interactions, the luminosity can be determined in turn.
To measure luminosity at H1, the 'Bethe-Heitler' process, i.e. electron-bremsstrahlung, ep $\rightarrow$ epγ is used. The cross-section is well known from QED and big enough to be used for normalization. As indicated in figure 2.9, the luminosity system consists of a dedicated calorimeter for electron detection[7] (electron tagger) and another one to detect the photons (photon tagger). In operation, both calorimeters operate in coincidence. Only the photon-detector is used to determine $\mathcal{L}$, the e-tagger primarily serves to estimate the systematics. Since $\mathcal{L}$ strongly depends on the beam condition, it is measured simultaneously to data-taking.

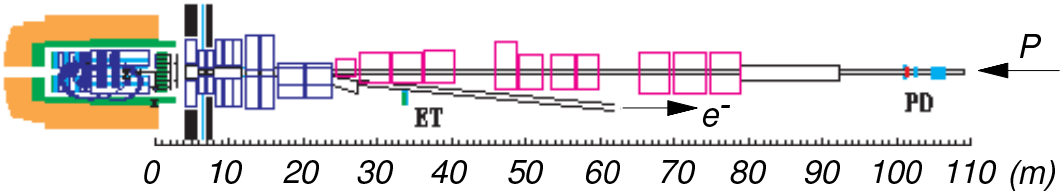

Figure 2.9: *The luminosity system*

The calorimeters are situated close to the beam pipe, as Bethe-Heitler electrons and photons are mainly emitted under small angles with respect to the electron beam. Both taggers are Cherenkov-calorimeters and consist of TlCl- and TlBr- scintillator crystals. They are located at z=-33 m in case of the electron tagger, covering an area of 154×154 mm, and at z=-103 m in case of the photon tagger, being sensitive to a 100×100 mm area. The e-tagger used in this analysis is capable to measure electron energies between 5.5 GeV and 22 GeV. To shield the photon-tagger from synchrotron radiation, a lead-layer of two radiation lengths is applied as well as a water Cherenkov-counter that serves as a veto.

2.2.6 Trigger System

As the incoming amount of data is enormous, data reduction is absolutely crucial at experiments in particle physics. It is the job of a multi-level trigger system to smartly select events that should be stored permanently.

[7] Altogether four electron detectors are available: at z=-7m, z=-8m, z=-33m and z=-44m. For this analysis, the one at z=-33m will be used.

Seeing the high rate of bunch crossings of $\approx 10\,\mathrm{MHz}$ as well as a rate of background events of $10 - 100\,\mathrm{kHz}$, and in contrast the limitation on the rate for data storage to 10 Hz, evidently smart hard- and software is necessary to manage event selection. In order to keep the dead-time (the time in which the detector cannot take data) as low as possible, a pipeline architecture appears necessary.
Hence, following the 'first-in-first-out' principle, the data coming in from all the subdetector components is pipelined with a depth of $2.6 - 3.4\,\mu\mathrm{s}$ (27-35 BC) [22]. In order for the trigger system to reduce the rate of event candidates to 10 Hz, four on-line and one off-line levels are available. The structure of this trigger system is shown in figure 2.10. The allocated time for event processing increases with depth.

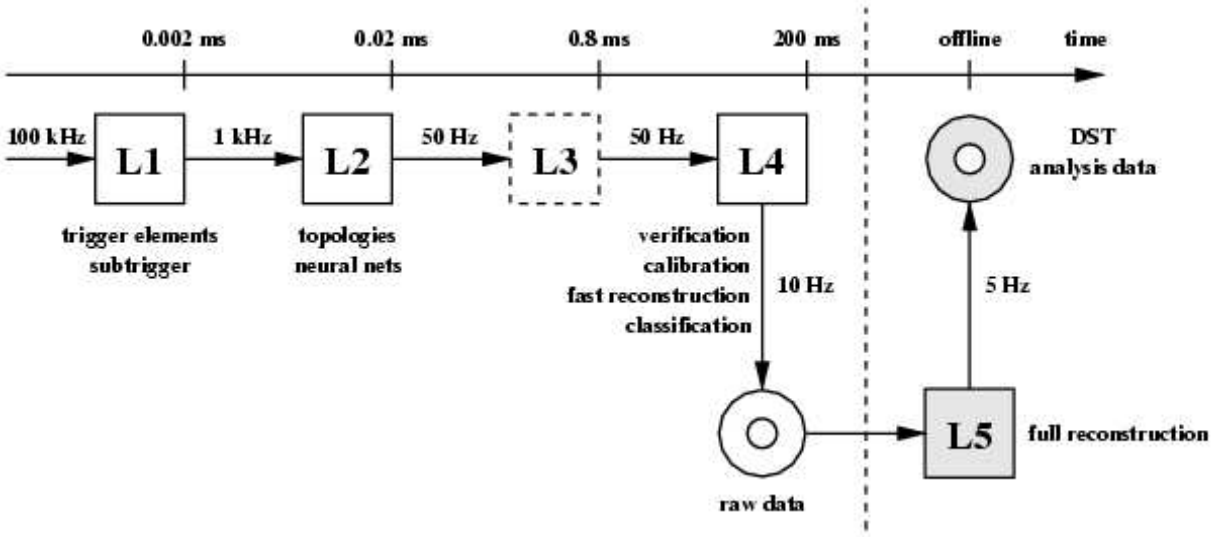

Figure 2.10: *The H1 trigger system. Displayed are on-line trigger levels L1-L4, their maximum incoming data rate and processing time. The off-line level L5 is illustrated, too.*

First Level - L1

Corresponding to the minimum depth of the pipeline of 27 BC, the first level has to come to its decision whether or not to keep the event candidate within $2.3\,\mu\mathrm{s}$. To do so, two tasks have to be completed:

Recognizing non-empty events reduces the rate to 10-100 kHz. The majority of all events are background events.

Preselection of potential 'physics events'. Here, some first event properties are examined to separate background from interesting events.

At this stage, most subdetectors of H1 provide simple but fast information which is used by the trigger. A combination of different requirements on these provided information (trigger-elements) is called a subtrigger. The central trigger logics on level one (CTL1) offers 128 of such subtriggers. They are dedicated to specific event

topologies or physics areas. The subtrigger used in this analysis will be dealt with in greater detail in section 4.3. As soon as one of the L1-subtriggers fires ('L1-Keep'), the pipeling is interrupted and the dead time begins.

Second Level - L2

If 'L1-Keep' occurs, level two has 20μs to reduce the rate of background events on a more sophisticated level ('L2-Reject'). In contrast to CTL1, L2 is supplied with more detailed information from the various subdetectors. To stick to the limit of 20 μs, these calculations are performed in parallel by two systems, namely the 'L2TT' ('L2-Topological-Trigger', see [29]) and the 'L2NN' ('L2-Neural-Network-Trigger', see [30, 31, 32]).

Fourth Level - L4

As level three is not implemented, the trigger hierarchy continues with L4. Here, full detector information is available. As soon as the read-out is completed, the data are stored in an event buffer and the detector is re-enabled to data-taking. L4 is realized as a multiprocessor-farm with 20 Power-PC cards. Each card processes one single event, whereby first off the tracks are be reconstructed and the calorimeter cells are collected to clusters. Until 1997, only such events were kept that fit in so-called 'physics classes'. Each class hereby stands for a specific field of interest for certain groups at H1. As luminosity rose steadily, the old algorithms did not satisfy the demands on the processing rate anymore. Since 1997 thus, the strategy how to determine background and how to categorize events to certain physics regimes has been changed. To achieve higher reduction of the data rate, i.e. faster and more effective processing, so-called 'physics-finders' were introduced. These routines try to verify certain conditions in an event. Only if at least one of these finders accepts the event it will be written on tape. The output at this stage is referred to as 'raw data'.
Furthermore, level four serves as a monitoring tool for data taking and for the online calibration of detector components.
As long as the incoming data rate remains below the currently processible 50 Hz, this L4-trigger works without dead time.

Fifth Level - L5

This off-line level runs the full event reconstruction. Besides, it serves also calibration purposes and classifies events into so-called 'physics classes', according to their physics signature. Events have to be verified to belong to one of these classes in order to be accepted.
All data is finally stored on magnetic tapes called 'physics output tapes' (POT). For faster access, the data is compressed and stored on hard-disk drives, so-called DST's ('data summary tapes'). This is the starting point for any analysis.

Chapter 3

Monte Carlo Generators

Monte Carlo generators are of great importance in the entire field of particle physics. They serve to study detection probabilities, resolution effects, or background behavior (see section 3.2).
In principle, several steps are neccesary to obtain a proper set of Monte Carlo data. First of all the actual interaction process is simulated. This is referred to as 'generator level'. In this part, the actual 'physics', i.e. interaction, is modelled. As a result, all the four-momenta of the so-created particles are calculated and relayed to 'simulation' which is the second step. This detector simulation in turn calculates the interaction of the particles with the detector material, including production of secondary particles and showers. All the technical properties of the detector and its various components play a major role here. At H1, the official program H1SIM [33] based on the GEANT package [34] performs this task. The output has exactly the same format like real data. Thus, the same reconstruction program can be applied for Monte Carlo generated events as for real data. H1REC is the official H1-specific reconstruction program.
Two Monte Carlo generators come to use in this analysis. ToyGen was employed to generate double-diffractive ω-ϕ-events, thus served as the signal-Monte Carlo. Moreover, ToyGen was used to determine the detector acceptance which will be dealt with in chapter 4.6. PYTHIA in turn simulates all possible processes in γp-interactions. It was applied here to describe the background.

3.1 ToyGen

ToyGen [35] is the first Monte Carlo generator that, even though unpublished, offers the possiblity to simulate double-diffractive events with Pomeron- and/or Odderon-exchange ($I\!P, O$ respectively). Single-diffractive processes are implemented as well. ToyGen was designed to provide processes on a more qualitative level rather than enabling calculation of cross-sections, as matrix elements haven't been implemented yet. Hence, it mainly serves to estimate efficiencies and acceptances. The processes which are simulated are of the kind

$$ep \to (e' + \gamma)p \to (e' + [\gamma \to M_{bw} + I\!P_1])(p' + I\!P_2) \overset{I\!P_1 + I\!P_2}{\longrightarrow} e' M_{bw} M_{cen} p', \qquad (3.1)$$

where M_{bw}, M_{cen} refer to the backward- and central-mesons respectively, and $I\!T$, symbolizing a unspecified trajectory here, indicates either Pomeron- or Odderon-exchange, as well as exchange of meson-trajectories. Only the exchange of Pomeron- and Odderon-trajectories is of interest for this analysis though. A more graphical depiction of these processes is given in 1.6.
The two major distributions that are incorporated into ToyGen and come to use here are the photon- and the pomeron/odderon-flux. They form the physical basis of this program. In the 'Weizsäcker-Williams-Approximation' (WWA), the photon emitted by the electron can be described by a two-dimensional probability density function (pdf) $f_{\gamma/e}(y, Q^2)$. This is described explicitly in 1.5.2 in the theory chapter.
The second implemented distribution is the flux for $I\!P$-$I\!P$-exchange. More precisely, one has to deal with two fluxes: One at the upper vertex and one at the lower vertex. Here, two important assumptions come in: Firstly, as the Odderon is thought to be the 'C=P=-1'-partner of the Pomeron, their fluxes are considered equal. Secondly, no distinction is made whether the $I\!P$, $I\!P$ respectively, couples to the photon- or the proton vertex. The flux model [36, 37] used in this analysis[1] to generate events however can be parametrized as

$$f_{I\!T/\gamma}(\xi, t) \;=\; f_{I\!T/p}(\xi, t) \;=\; \frac{1}{2}\frac{1}{2.3}\frac{1}{\xi}(6.38 \cdot e^{8t} + 0.424 \cdot e^{3t}). \tag{3.2}$$

Such a flux factor describes the probability to find a Pomeron or Odderon, respectively, inside the photon or proton, respectively, carrying the longitudinal momentum fraction ξ of the proton's or photon's momentum, where $\xi = 1 - x$ and x here denotes Feynman-x. $t = (p - p')^2$ is the corresponding Mandelstam variable. $\sqrt{t}$ can so be pictured as the mass of the exchanged Pomeron or Odderon, being imaginary though, as the exchange takes place in the t-channel. With these three flux factors, one can basicly describe such a double-diffractive process phenomenologically.
To derive a real cross-section for double-diffractive processes of this kind [38], one can make several assumptions to simplify the calculation. It has to be emphasized that this calculation has to be treated with care, as the flux-model 3.2 is just one possible parametrization. The following procedure is meant to show the way how to derive such a cross-section in principal. The models and values that are applied are not safe enough to derive predictions. A more thorough derivation of the following can be found in [39].
Assuming that the cross-section can be factorized, one basically needs to integrate the three fluxes introduced above over the kinematic range of interest and multiply with the cross-section that describes $I\!P$-$I\!P$-, $I\!P$-$I\!P$- or $I\!P$-$I\!P$-fusion which creates the central meson. Another point one has to take care of is the azimuthal dependence of the central meson production. For HERA, i.e. photoproduction, this gives

$$\frac{d^8\sigma}{dy dQ^2 dt_1 d\xi_1 d\varphi_1 dt_2 d\xi_2 d\varphi_2} = f_{\gamma/e}(y, Q^2)\, f_{I\!T_1/\gamma}(\xi_1, t_1)\, f_{I\!T_2/p}(\xi_2, t_2)\sigma'. \tag{3.3}$$

The quantity σ' is the cross-section for the fusion of $I\!P$ and $I\!P$ or other combinations thereof as described above. The UA8 collaboration [38] assumes this cross-section

[1] ToyGen provides numerous flux models to choose from.

to be constant, namely $\sigma' = 1\,\mathrm{mb}$.
The total cross-section comes out after integration to

$$\sigma_{tot} = 4\pi^2 F_{\gamma/e}\, F_{I\!P_1/\gamma}\, F_{I\!P_2/p}\, \sigma'. \tag{3.4}$$

The integrated fluxes are thereby

$$F_{\gamma/e} = \int dy \int dQ^2\, f_{\gamma/e}(y, Q^2) \quad \text{and} \quad f_{I\!P_{1,2}/\gamma,p} = \int d\xi \int dt f_{I\!P_{1,2}/\gamma,p}(\xi, t). \tag{3.5}$$

The factor of $4\pi^2$ is obtained by carrying out the φ-integrations and thus gaining a factor of 2π from each flux-factor. It has to be stated that ToyGen serves merely the purpose to determine acceptances. It was not designed and is in particular not tested to calculate cross-sections.
Table 3.1 shows the implemented limits for the Pomeron-, Odderon-flux variables for the generation of double-diffractive events with ToyGen. The limits hold for both, the upper and the lower vertex.

variable	value
ξ_{min}	10^{-8}
ξ_{max}	$5 \cdot 10^{-2}$
$\lvert t_{\mathrm{min}} \rvert$	$10^{-15}\,\mathrm{GeV}^2$
$\lvert t_{\mathrm{max}} \rvert$	$1\,\mathrm{GeV}^2$

Table 3.1: *Kinematical limits in ToyGen*

The plots in figure 3.1 give an idea of ω-ϕ-events generated with ToyGen and their kinematical properties. The variable p_t denotes the transverse momentum component with respect to the z-axis. ToyGen generates a flat mass-distribution for the ϕ-meson. It is therefore weighted with a suitable 'Breit-Wigner'-function afterwards in order to obtain the typical mass-spectrum that is shown in figure 3.1.

3.2 PYTHIA

As described in the introduction to this chapter, the PYTHIA generator [40, 41] is capable to simulate all kinds of reactions that occur in γp-interactions and makes predictions about the individual contributions to the overall cross-section. This analysis tries to find evidence for ω- and ϕ-mesons created simultaneously in photoproduction. PYTHIA simulates physics in all kinematical regimes though. By applying suitable cuts (see following paragraphs), the contribution to the regime that is dealt with in this analysis can be examined.
PYTHIA does not describe low-multiplicity states adequately though, as double-diffractive processes are not implemented. Thus, PYTHIA was used here to primarily estimate the contributions of the high-multiplicity photoproduction tails to the background.
PYTHIA uses a combination of two different models to describe these processes.

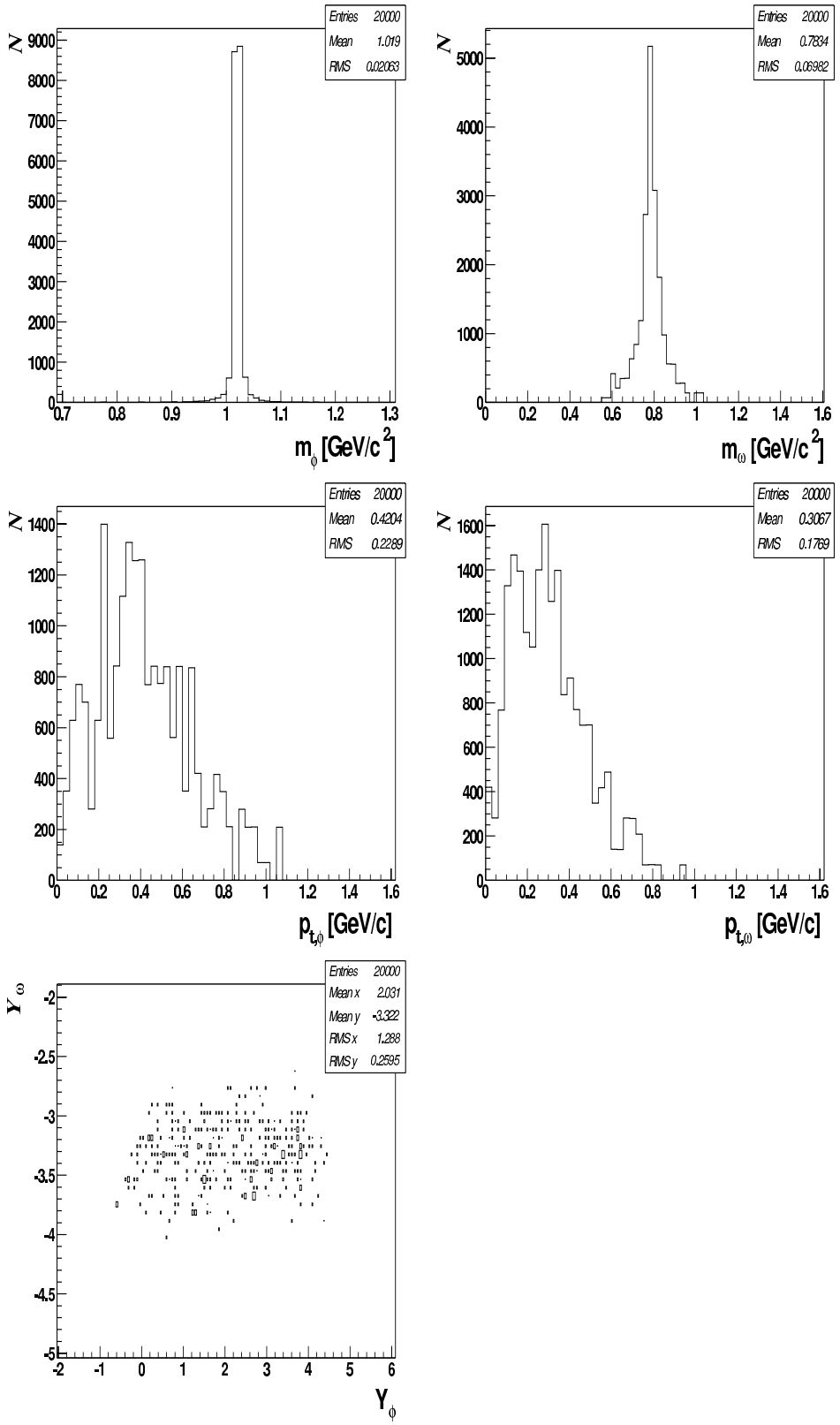

Figure 3.1: *Invariant mass-, p_t- and rapidity distributions of ToyGen-generated ω-ϕ-events.*

The so-called 'Vector Meson Dominance Model' (VMD) describes processes where the photon fluctuates into a vector meson before interacting with the proton. Hence the photon is treated like a hadron. This model is discussed in subsection 1.5.1 in the theory chapter. The other contributions describes the case where the photon interacts directly with a parton of the proton.
To remain within the e-tagger acceptance in order to model the experimental conditions, i.e.$0\,\mathrm{GeV}^2 \leq \mathrm{Q}^2 \leq 0.01\,\mathrm{GeV}^2$ and $0.25 \leq \mathrm{y} \leq 0.85$, generation was restricted to just these ranges. Furthermore, several cuts are applied at generator level. They ensure that the generated events have the desired signature (see 1.6), i.e. tracks in the central trackers and activity in the SpaCal calorimeter. The exact condition is:

$$N_{tracks,25-155} \leq 3 \quad \&\& \quad 1 \leq N_{tracks,10-155} \leq 4$$

$$\&\& \quad 2 \leq N_{SpaCal} \leq 9 \quad \&\& \quad N_{SpaCal,E} \geq 1.$$

The applied variables are:

$N_{tracks,25-155}$: Multiplicity of central tracks within $25° \leq \Theta \leq 155°$ and $\mathrm{p_t} > 0.1$ GeV.

$N_{tracks,10-155}$: Multiplicity of central tracks within $10° \leq \Theta \leq 155°$ and $\mathrm{p_t} > 0.1$ GeV.

N_{SpaCal}: Number of particles in the acceptance region of SPACAL.

$N_{SpaCal,E}$: Number of particles in the acceptance region of SpaCal, with $\mathrm{E_{particle}} > 1.5$ GeV and $\mathrm{R_{particle}}$(distance from beam pipe)> 18 cm.

Later on, the data are transformed from the format they are stored on the DST's (see 2.2.6) into a format that is easier to work with, as data are organized therein in numerous variables, each in turn filled event-wise. This format is called 'n-tuples', alluding to the file structure. The cuts which are performed after simulation and reconstruction, namely during n-tuple creation, are exactly the same as for data. Tables 4.1 and 4.2 in subsection 4.2 summarize them.
The luminosity of the generated PYTHIA data amounts to $28\,\mathrm{pb}^{-1}$. At last, 2.3×10^6 events survive the cuts explained above and remain for further analysis.
During final selection when working with PYTHIA-generated data, i.e. on user-level, one has to take special care of the e-tagger, since the e-tagger is not implemented in H1SIM (see 4.5), i.e. in simulation. For this analysis, the resolution of the e-tagger33 was estimated by 'smearing out' the energy of the generated electron. This has been done by employing a Gaussian distribution and randomly shuffle the so simulated tagger energy around this Gaussian. This is justified as this function corresponds well to the experimentally determined profile of this calorimeter.
After the final cuts at user-level (see 4.7) and applying the correct weights (see 4.4), the histograms in figure 3.2 are obtained. They depict a variety of distributions in order to get an idea of the contributions of PYTHIA-estimated background. Some of these distributions will be compared to data later on in section 5.1 in the final 'Results'-chapter.
The abbreviation 'track-track'-mass used in this context hereby refers to the invari-

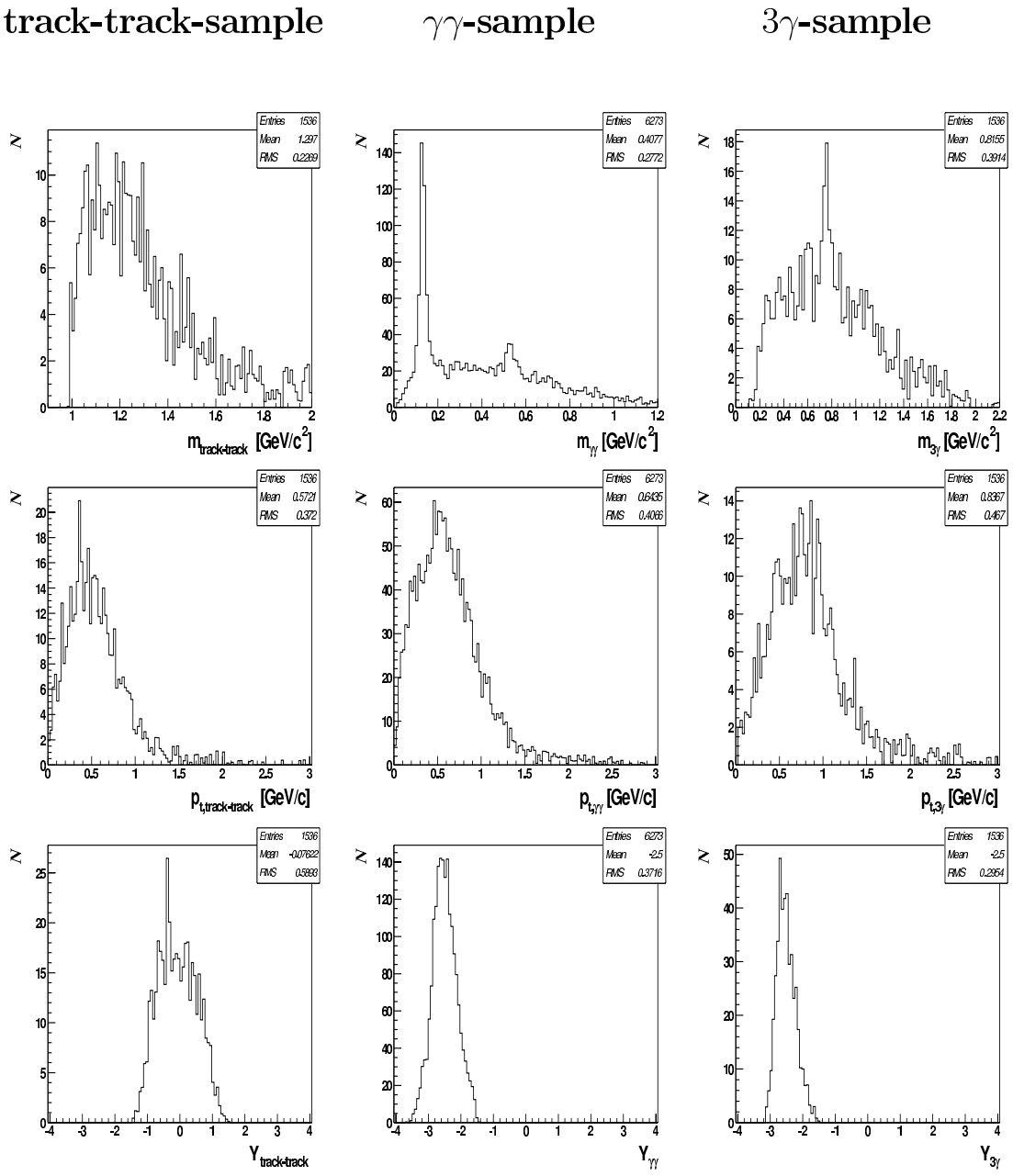

Figure 3.2: *Invariant mass-, transverse momentum p_t-, and rapidity Y distributions of PYTHIA-estimated background. The first column represents the track-track sample, columns two and three the $\gamma\gamma$- and 3γ- samples, respectively. The abbreviations 'track-track', '$\gamma\gamma$' and '3γ' are explained in the text. A clear π^0- and η-signal can be recognized in the $\gamma\gamma$-mass spectrum (nominal masses 135 MeV (π^0) and 547 MeV (η)). An ω-signal can be found in the 3γ-mass distribution (nominal mass 783 MeV).*

ant mass of two particles measured in the CJC which is obtained by adding their four-momenta. They are reconstructed via two tracks, applying the kaon-hypothesis, i.e. assuming these particles to be kaons. The kaon-hypothesis on the tracks ensures that contributions to a possible ϕ-signal could be picked out. $\gamma\gamma$-mass, 3γ-mass respectively, refers to the invariant mass of two or three photons, respectively, which is obtained by again adding their four-momenta. These are reconstructed via their energy deposition in the SpaCal ('clusters'). In case of the 3γ-mass, one of the three 2γ-mass combinations is required to lie within a 40 MeV mass-window around the nominal π^0-mass (see 4.7.4). These abbreviations will be used from now on. The same holds correspondingly for the labelling of the transverse momentum p_t and the rapidity Y. For further information on reconstruction of kinematic variables see 4.1. The mass-distributions clearly show a π^0- and η-signal in the $\gamma\gamma$-mass spectrum and a conspicuous ω-peak in the 3γ-sample. A significant ϕ-signal is in turn not visible in the track-track-mass spectrum. The rapidity distributions show for the track-track sample unambiguously central activity (acceptance region of CJC: $-1.7 \leq Y \leq 1.7$), whereas backward activity (acceptance region of SpaCal: $-3.5 \leq Y \leq -1.4$) is obvious for the other two samples.

Chapter 4

Analysis

This chapter collects all necessary ingredients for determining the cross-section in the next and final chapter. It covers the range from reconstruction of kinematic variables and data reduction via preselection of events and subtrigger, over efficiency and acceptance considerations to scaling factors on trigger levels one and four, and luminosities.

4.1 Reconstruction of the Kinematic Variables

It will be shown here how the applied kinematic variables introduced in 1.1 are reconstructed in this analysis. Since due to the e-tagger acceptance the average γp-center-of-mass energy is 200 GeV, the electron-, proton- and ω-masses will be neglected for the reconstruction.

4.1.1 Inelasticity y and Virtuality Q^2

The inelasticity y and the four-momentum transfer at the electron-photon vertex Q^2 are reconstructed via the electron which is measured in the e-tagger. Taking equations 1.2 and 1.3 in section 1.1,

$$y = 1 - \frac{E'_e}{E_e} sin^2\left(\frac{\Theta}{2}\right) \text{ and}$$

$$Q^2 = 4E_e E'_e cos^2\left(\frac{\Theta}{2}\right),$$

and taking into account the rather small scattering angles of the electron in the examined reactions, one can assume $\Theta \approx \pi$ and gets

$$y \approx 1 - \frac{E'}{E} \tag{4.1}$$

$$Q^2 \approx 0\, GeV^2. \tag{4.2}$$

Here, Θ denotes the scattering angle of the electron, E and E' are the energies of the incoming, outgoing respectively, energies of the electron.

4.1.2 Photon-Proton Center-of-Mass Energy W

Equation 1.7,

$$W^2 = q^2 + 2qp + m_P^2,$$

can be transformed by plugging equation 1.1 in equation 1.3. One finds 2qp=ys. Applying the approximations that were introduced in the preceding subsection, one obtains

$$W \approx \sqrt{ys}. \tag{4.3}$$

y can be calculated from equation 4.1.

4.1.3 Invariant mass $m_{3\gamma}$ of the 3-Photon System

This mass is obtained by summing up the four-momenta of the three photons

$$m_{3\gamma} = \sqrt{p_{3\gamma}^2}, \text{ with } p_{3\gamma} = p_{\gamma 1} + p_{\gamma 2} + p_{\gamma 3}. \tag{4.4}$$

4.1.4 Invariant Mass $m_{K^+K^-}$ of the 2-Kaon System

The mass is obtained as

$$m_{K^+K^-} = \sqrt{(p_{K^+} + p_{K^-})^2}, \tag{4.5}$$

where the p_K are the four-momenta of the two kaons.

4.2 Preselection

Seeing the huge amount of data gathered at the H1 experiment, it is clearly necessary to reduce them in order to come to processible as well as transferable amounts of data. This happens by preselecting events during n-tuple creation, where the emphasis is on selecting suitable tracks, and by choosing a subtrigger, where the emphasis is on suitable SpaCal activity, which is topic of the next section.
The following table 4.1 gives an overview of the applied cuts.

$8\,\text{GeV} \leq E_{etag33} \leq 20\,\text{GeV}$
One or more clusters in the electromagnetic section of SpaCal
Existence of a primary vertex
Exactly two central tracks fulfilling the quality criteria enumerated in table 4.2
No forward tracks
Run quality∈[good,medium]
Phase> 1

Table 4.1: *Summary of preselective cuts*

4.2.1 Scattered Electron

The first condition of the table assures to stay within the photoproduction regime. The electron needs to be detected by the e-tagger at 33 meters and the deposited energy has to be between 8 and 20 GeV. Having in mind relation 4.1

$$y \approx 1 - \frac{E_{electron}}{E_{beam}},$$

where y is the inelasticity, $E_{electron}$ the deposited energy of the scattered electron in the e-tagger at 33 m and E_{beam} the electron beam energy, one gets the covered inelasticity range[1] of $0.27 \leq y \leq 0.71$.

4.2.2 Backward Meson

As a hint for backward mesons in multi-photon final states, activity in the electromagnetic section of SpaCal would clearly serve. This is implemented as a condition that claims at least one cluster in the electromagnetic section of SpaCal.

4.2.3 Central Meson

A primary vertex is substantial for detecting two kaon-tracks, ϕ-mesons would decay into at this vertex. The more, these tracks have to be central and to fulfill certain quality criteria that are presented in greater detail in table 4.2. Principally, these tracks could also point in the forward direction. This analysis deals with central tracks only, as technical problems with the forward tracking devices did prevent reliable data to be gathered. Thus, forward tracks are excluded. The specific requirements for track candidates are presented in detail in table 4.2.

Variable	Value
Θ	$20° - 160°$
Minimum p_t	0.15 GeV/c
Maximum DCA	2 cm
Maximum Rstart	50 cm
Minimum track length ($\Theta < 150°$)	10 cm
Minimum track length ($\Theta > 150°$)	5 cm
Double track RPTPHTH	1

Table 4.2: *Technical cuts on tracks in preselection*

'DCA' hereby stands for 'distance of closest approach'. So, the track needs to get as close to the vertex as 2 cm to get accepted. 'Rstart' refers to the radius (distance from the beam pipe) of the first hit and 'Double track RPTPHTH' avoids double-counting of tracks.

[1] As in final selection (see section 4.7) this range will be further restricted to $0.3 \leq y \leq 0.7$, this range will be referred to in the following.

4.2.4 General Requirements

Another cut concerns the state of readiness of the detector systems. Periods when data are taken are categorized in so-called 'runs' which are labelled 'good', 'medium' or 'poor', according to the status of the most important detector components. For this analysis, only 'good' and 'medium' runs have been accepted. This ensures that the important components to this analysis, like CJC and SpaCal, were operational. The more, runs are subdivided in 'phases' from 1 to 4. As phase 1 refers to the beginning of a run, i.e. data-taking, when the storage ring has just been filled and the beam conditions are not yet ideal, the phase is required to be 2 at least. The more, the CJC is not operational in phase 1.

4.3 Subtrigger

4.3.1 Conditions

As described in 1.6, this analysis aims at three photons in the SpaCal and two central tracks. The central tracks, as well as the photons in the SpaCal, are not selective on photoproduction events though. To ensure this, one needs to make sure the electron is not scattered under angles that are large enough for the electron to end up in the detector. Thus, the electron is demanded to be detected in the electron tagger at 33 m ('tagged photoproduction'). This restricts the inelasticity y to $0.3 < y < 0.7$.
As indicated in 4.2, the emphasis for the subtrigger is on suitable SpaCal activity. A subtrigger that fulfills this requirement, selects photoproduction events efficiently and reduces background to a tolerable level, is S50 (see 2.2.6). This trigger is a pure SpaCal and e-tagger trigger. The most important elements on level one (L1) of the S50 definition are

$$eTAG \;\&\&\; (SPCLe\_IET > 1 \;||\; SPCLe\_IET\_Cen\_2), \tag{4.6}$$

where '&&' indicates logical 'and', whereas '||' stands for logical 'or'.
The condition 'eTAG' is true, if more than 4 GeV energy is deposited in the e-tagger at 33 m and if less than 2 GeV is deposited in the photon detector. This requirement so ensures an electron in the desired e-tagger and suppresses contributions from 'Bethe-Heitler'-overlap. The condition (SPCLe_IET $>$ 1 || SPCLe_IET_Cen_2) is true, if a cluster, i.e. a localized energy deposition, in the electromagnetic section of the SpaCal fulfills $E_{cluster} > 2\,GeV$.
The complete description of S50 includes time-of-flight conditions as well. This ensures that detected events originate in nominal bunch-crossings.
An additional condition belongs to S50 on level two (L2): SPCL_R20, SPCL_R30 respectively. This requirement performs a radius cut of 20 cm, 30 cm respectively since run number 198827, around the beam pipe. It was introduced to reduce the rate of low-Q^2 events overlapping with Bethe-Heitler ones.
Clearly, the sensitivity to measure mesons travelling in backward direction suffers from this radius cut, as high p_t are not too likely for the backward mesons.

4.3.2 Efficiency

In order to determine a cross-section, the trigger efficiency is one of the important factors. For this analysis, this does not include the electron tagger, since its acceptance function has been measured and is well known (see 4.5). To obtain the trigger efficiency, first of all 'control triggers' must be selected. At this stage, preselective cuts (see 4.2) have been made upon the employed data set, but clearly no subtrigger has been required yet. Practically, this was done by filling a histogram of subtriggers which are labeled by numbers, from 0 to 127. If an event causes a specific subtrigger to fire on level one and four, the appropriate bin gets incremented. Hence, quite a decent idea of which subtriggers contribute most to the statistics can be obtained. In figure 4.1 this has been done for the years 1996, 1997, 1999 and 2000. One can clearly see how these distributions differ from year to year, and that the selection of S50 is justified, as, besides fulfilling the desired conditions (see equation 4.6), it delivers good statistics.

The control-triggers shouldn't have much in common with S50, otherwise independent cross-checking of this subtrigger would clearly not be possible. As shown in the figure, the different distributions do require picking different control triggers for every year though. As shown in the appendix (A), neither one of the finally selected subtriggers has SpaCal conditions, and all of them are among the most active ones in their specific year concerning the event-signature in this analysis.

The efficiency of S50 should clearly depend mainly on the energy of the 'hottest cluster' (E_{HC}), i.e. the cluster with the highest deposited energy in the electromagnetic SpaCal, as this is the cluster whose energy has to exceed 2 GeV to cause S50 to fire (see S50 conditions, equation 4.6). To obtain the efficiency now as a function of E_{HC}, one has to devide the distribution of E_{HC} for the control trigger only (i.e. L1 and L4 activity is demanded only for the control trigger) by the distribution of E_{HC} where activity is claimed now for the control trigger as well as for S50. This procedure is illustrated for the year 1996 in figure 4.2.

Applying this procedure to the other years yields the corresponding efficiencies which are presented in figure 4.3. One can see that at a hottest cluster energy of $\approx 2.5\,\text{GeV}$ the efficiency for the SpaCal trigger requirements is almost 100 %. Thus, for this analysis an efficiency of 100 % will be assumed. A cut on the applied data set of 2.5 GeV on the hottest cluster energy is therefore performed during final selection (see 4.7.4).

4.3.3 Luminosities

The integrated annual luminosities after all weighting mechanisms, see subsection 4.4 for more details, one obtains for the S50 subtrigger are given in the table below. The luminosity system of H1 is explained in subsection 2.2.5.

1996	1997	1999	2000
$4.762\,\text{pb}^{-1}$	$3.516\,\text{pb}^{-1}$	$3.224\,\text{pb}^{-1}$	$7.427\,\text{pb}^{-1}$

Table 4.3: *Integrated S50 luminosities per year*

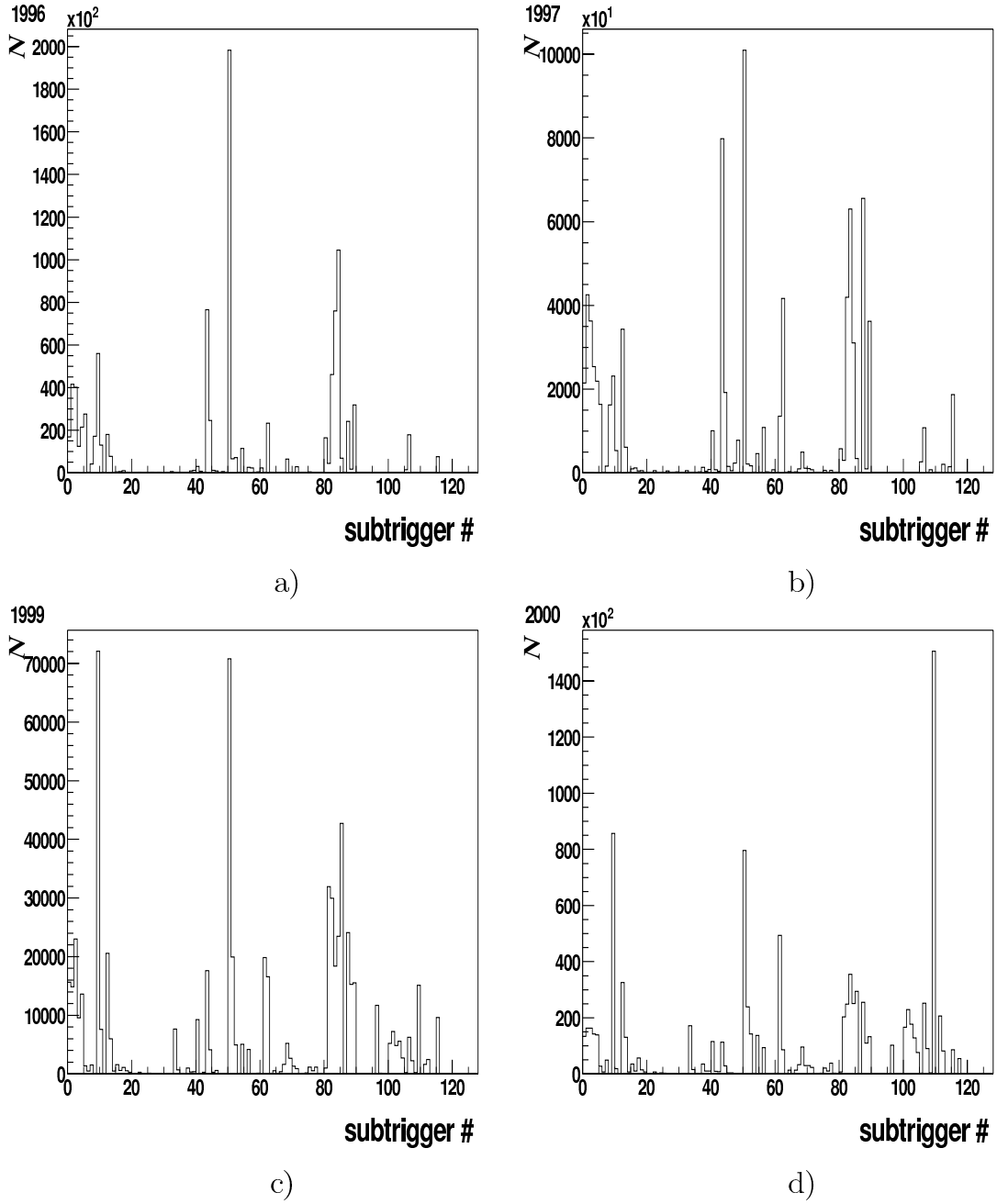

Figure 4.1: *Distribution of subtriggers from 1996, 1997, 1999 and 2000 data. Preselective cuts have been applied on the data beforehand (see 4.2).*

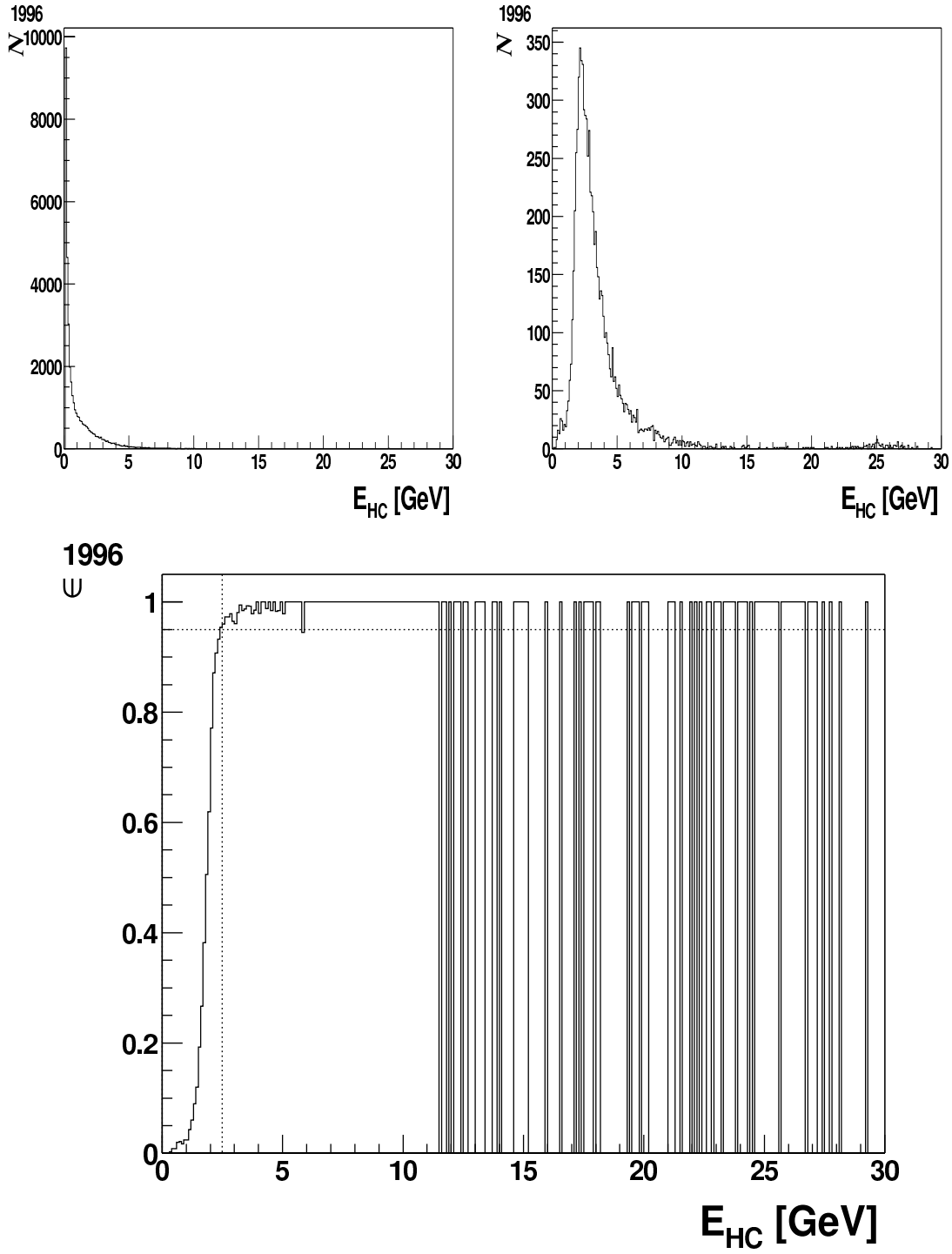

Figure 4.2: *'Hottest-cluster' energy (E_{HC}) distributions for the control trigger only (top left), for control trigger and S50 (top right) and the efficiency ϵ for S50 in 1996 (bottom) which is obtained by building the ratio of the top left- and the top right histograms. Marked are a hottest cluster energy of 2.5 GeV and an efficiency of 95 %.*

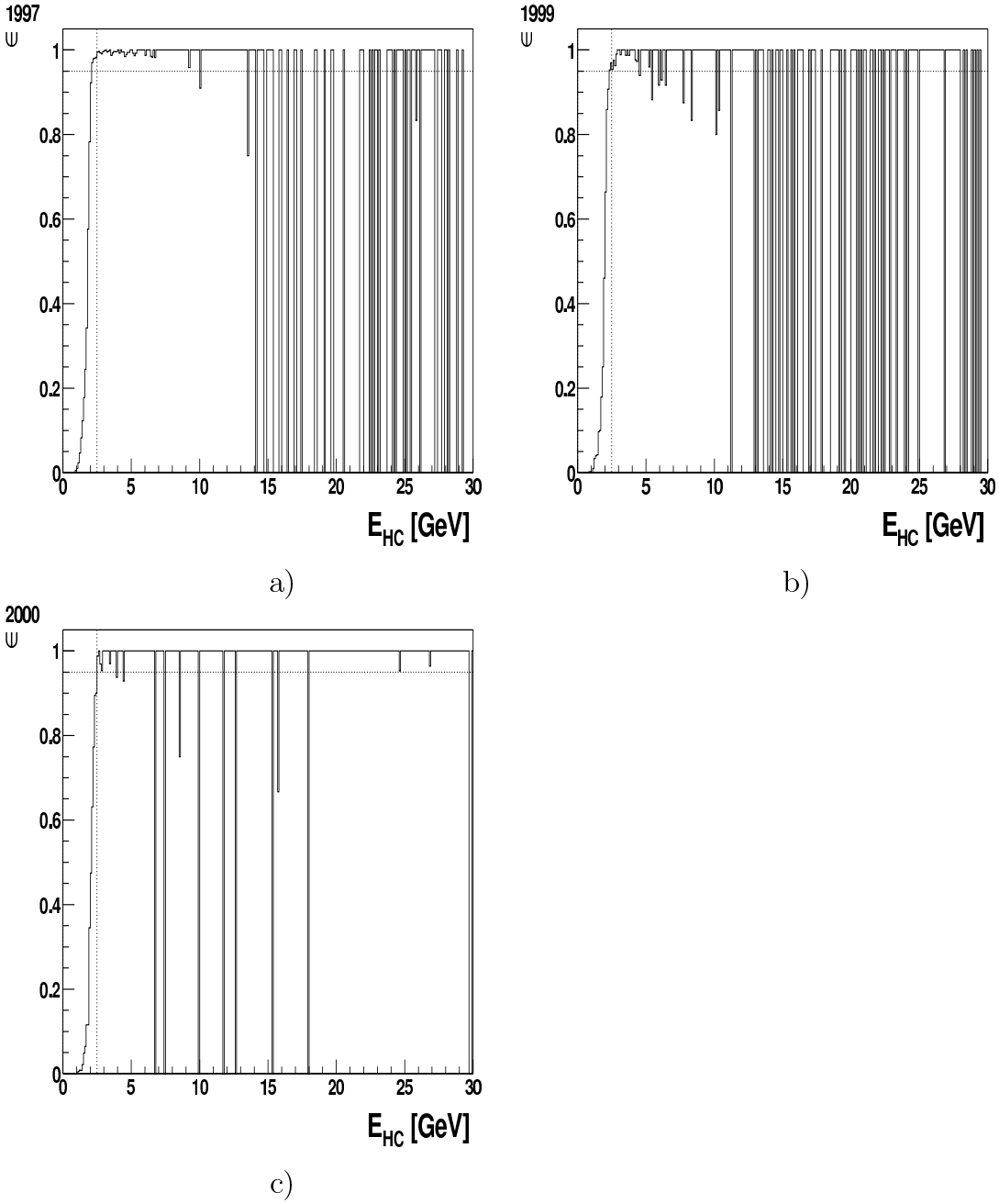

Figure 4.3: *Efficiency ϵ of the subtrigger S50 for the years 1997 (a), 1999 (b) and 2000 (c). The labelling of the histograms is explained in figure 4.2 showing the 1996 results.*

An overview of the most important quantities characterizing the H1 luminosity is given in figure 4.4. It depicts the integrated luminosity of HERA and H1, operation efficiencies, the mean dead time, the number of H1 runs per fill and the average time per run at H1 for the years 1996 to 2000, which is the period of time this analysis uses data of. The difference of the luminosity shown there to the S50 luminosities given in the table above are due to the so-called prescaling which is topic of the next section.

4.4 L1-Prescales and L4-Weights

Besides the specific requirements of S50 at all levels, another mechanism, closely connected to the choice of a particular subtrigger though, works at H1 to further sort out data. Two constraints necessitate the introduction of a weighting mechanism. Firstly the large cross-section for 'soft physics'. The contribution of photoproduction is large compared to deep-inelastic scattering (DIS) at higher Q^2. In order to balance the observed and recorded events, 'soft physics' events clearly need to be scaled down. Secondly the rate by which data is delivered to level four must not exceed 50 Hz, as the necessary steps for further processing cannot be taken otherwise (information on tasks performed by L4 can be found in 2.2.6).
Two measures intervene: At level one the so-called 'L1-prescaling', at level four the so-called 'L4-weights'. 'L1-prescaling' is realized as a hardware implemented run-dependent factor which denotes which ratio will be passed on to the next level. A factor of eight for instance hereby means every eighth event will be kept. All subtriggers are allocated a specific, usually different 'prescale factor', depending on their importance and the rate by which they fire on L1.
Practically, the term 'L1-raw' is used when referring to a subtrigger before prescaling, whereas 'L1-actual' refers to such after prescaling. Hence, 'L1-actual' decides whether or not to keep an event, passes on the event in case it is set and sets a flag ('L1-keep', 'L1-reject' respectively).
At L4, further downscaling takes place. At this stage, this is implemented via smart software, i.e. algorithms that scale the incoming events according to certain physics criteria. These weights are assigned event-wise.
Table 4.4 shows the L1 prescale-factors, the L4 weights, both averaged over each year, as well as the integrated annual luminosities for the S50 subtrigger.

	1996	1997	1999	2000
Lumin. before L1-prescaling $[pb^{-1}]$	5.663	15.233	13.254	45.7806
Average L1 prescale-factors	1.16	1.62	1.28	2.06
Lumin. after L1-prescaling $[pb^{-1}]$	4.9	9.42	10.317	22.2357
Average L4-weights	1.029	2.679	3.2	2.994
Lumin. after L1-and L4-scaling $[pb^{-1}]$	4.762	3.516	3.224	7.427

Table 4.4: *Averaged L1 prescale-factors and L4 weights for S50 per year, as well as the integrated yearly luminosities for S50.*

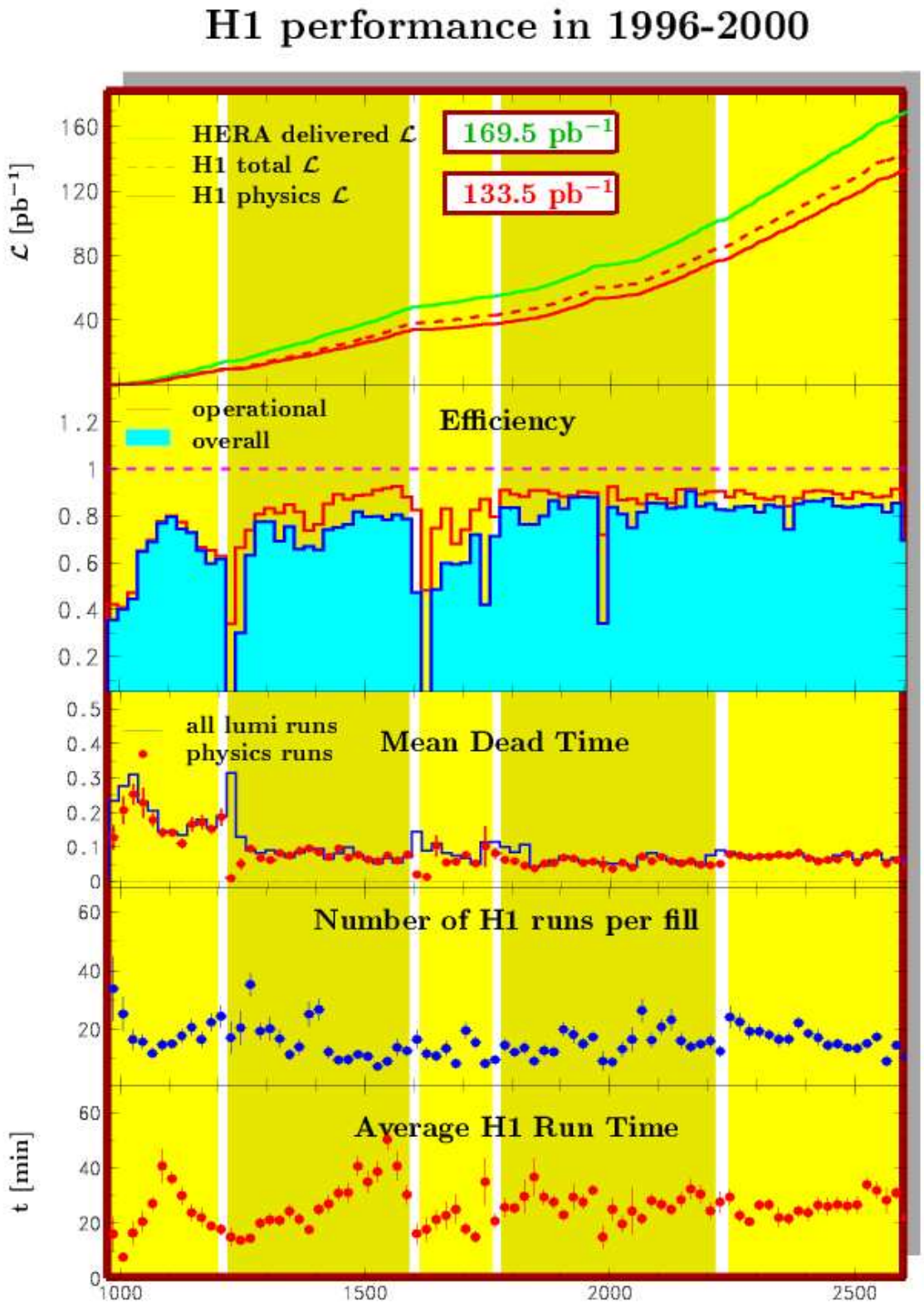

Figure 4.4: *H1 performance for the period 1996-2000. In particular the luminosities, efficiency, mean dead time, number of runs per fill and the average time per run is shown.*

Evidently, both factors have to be considered when finally determining a cross-section. The number of remaining events after all applied cuts has to be multiplied by these two factors to get the number of events that really occurred during the interactions.
Without the prescaling- and weighting mechanisms, the luminosity of the data amounts to $80\,\mathrm{pb}^{-1}$. Thereafter, $18.929\,\mathrm{pb}^{-1}$ remain.

4.5 Electron Tagger Acceptance

The acceptance of the electron tagger as a function of the inelasticity y is measured during data-taking and shown in figure 4.5. Depicted is this acceptance function for 1996 data. As one can see, due to poor acceptances below 0.3 and above 0.7 a cut of 0.3 and 0.7 on the data is well motivated. This domain in y defines the kinematical regime for the analysis. Each event is assigned the acceptance gained from this function. The acceptance has then to be considered for cross-section determination.

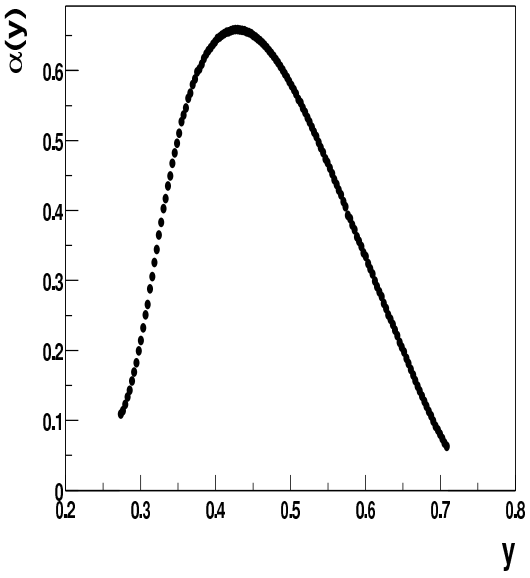

Figure 4.5: *Acceptance α of the e-tagger at 33 m as a function of the inelasticity y for 1996 data. Diagram from [4].*

It is important to take care that the shower does not get too close to the border of the calorimeter in order to keep losses of energy deposition low. To ensure a certain distance of the shower from the border, certain cuts are applied on the data. They are explained in detail in section 4.7.

4.6 Detector Acceptance

Detector acceptance first off means to determine what fraction of the events this analysis aims for (and nature generates) is actually detected by H1, i.e. by the

detector components that were used here. In this case, a method had to be worked out to determine the acceptance of the central trackers (CJC) and the SpaCal.
The idea is to generate ω-ϕ-events via ToyGen (see 3.1) and examine the populated phase-space, characterized by the rapidity Y of the ω- and the ϕ-meson. Practically, each event corresponds thus to an entry in a two-dimensional histogram, where the two axes represent the rapidity of the ω-, the ϕ-meson, respectively. A good reason for choosing rapidity to examine this phase-space is its form-invariance under Lorentz-transformations along the beam axis ('boosts'). Thus, rapidity differences are Lorentz-invariant.
In a second step, these events are simulated and reconstructed (simrec[2]). Hence, for this analysis, the SpaCal and CJC responses to these events are obtained. The population of phase-space now is compared to the population before simrec. Evidently, by building the ratio of the number of entries in such a histogram after simrec and the number of entries before simrec one obtains an overall acceptance.
The crucial point however is the determination of the so-called 'fiducial volume'. This term refers to a volume in the $Y_\omega - Y_\phi$-plane, introduced above, which we count events in, before and after simrec, to build the ratio and obtain the acceptance after all. This acceptance however is assumed to be flat over the fiducial volume. This has been verified by changing the kinematical parameters that are incorporated in ToyGen (see section 3.1).
In order to determine a reasonable fiducial volume, in a first step every photon originating in the ω-meson as the mother particle has been verified to hit the SpaCal detector, by demanding that its pseudo-rapidity η is within the acceptance region of SpaCal. If this is the case for all three photons from the ω, and if they deposit more than 100 MeV in SpaCal each[3], the reconstructed ω-ϕ event is entered in histogram (a) in figure 4.6. Since $2{\cdot}10^4$ events have been generated, as a first conclusion one can state that only a fraction of $\frac{7139}{20000} = 35.7\%$ of all events has the three photons from the ω end up in the SpaCal. For these entries, one can be sure that the ω-mesons can be reconstructed. The so-chosen rapidity spread for the fiducial volume is indicated in histogram (a) as horizontal dashed lines covering a range of $-3.8 \leq Y_\omega \leq -2.7$.
In principal, one could repeat this procedure for the ϕ-meson, the two kaon-tracks respectively, as well. As said before, the kaon tracks will be close to each other, i.e. a small angle is expected between the two tracks. If one track hits the CJC thus, it is quite likely for the other track to do so, too. Thus, the acceptance region of the CJC ($-1.7 \leq Y_\phi \leq 1.7$) is the range of choice. It is also indicated in figure 4.6 as vertical dashed lines.
As step number two, histogram (b) depicts the remaining events after simrec. As these 29 events are all within the fiducial volume defined above, marked by dashed lines, migration of events does not occur. This proves the chosen volume to be reasonable. The term 'migration' here alludes to the fact that if the fiducial volume is not determined properly, it might actually happen that for events where the three photons do hit the SpaCal in fact, the reconstructed ω does not appear inside this volume, thus migrate out. Vice versa, events can also migrate into the fiducial vol-

[2]The term 'simrec' will be used from now on to refer to simulation and reconstruction

[3]This is important, as during final selection, see 4.7, this 100 MeV cut on the cluster energy in the electromagnetic section of SpaCal is carried out and would therefore drop events with lower deposited energy, hence falsify the acceptance eventually.

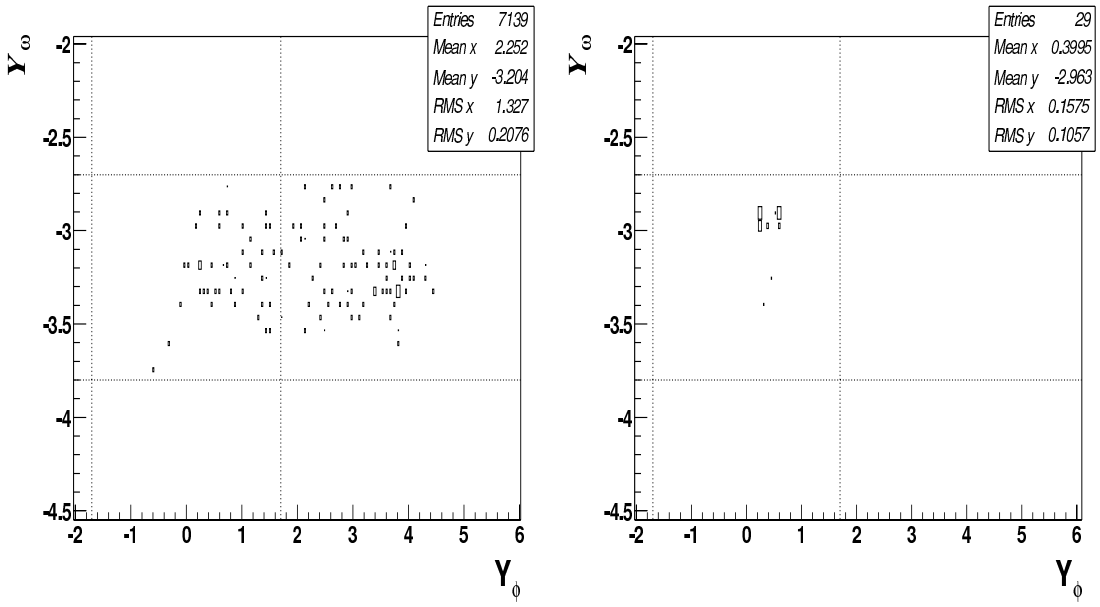

a) b)

Figure 4.6: *Phase-space distribution of ω-ϕ events generated with ToyGen. (a) displays the distribution on generator level, where the three photons coming from the ω-meson are required to hit the SpaCal. The marks indicate the hereby determined 'fiducial volume'. (b) displays the remaining events after simulation and reconstruction.*

ume. Either way, the value one obtained for the acceptance would clearly not be correct. The same argumentation holds for the ϕ-meson, respectively.

Considering the whole generated sample now, i.e. no demandments are made for the photons, the ratio of events after simrec, depicted in histogram (b) figure 4.6, and the number of events before simrec but within the above fixed fiducial volume, see histogram (a) in figure 4.7, yields the overall detector acceptance for events with $-3.8 \leq \mathrm{Y}_\omega \leq -2.7$ and $-1.7 \leq \mathrm{Y}_\phi \leq 1.7$, namely

$$\alpha_{\mathrm{det}} = \frac{29}{1190} = 2.4\%$$

with an uncertainty of 0.45 %. Histogram (b) in figure 4.7 shows which part of the data lies within the just determined fiducial volume. One has to be aware that due to this procedure the cross-section which will be presented in 5.2 refers to this region in phase-space only.

4.7 Final Selection

This section summarizes the final cuts that have been applied on the data in order to select the desired events. General conditions are discussed in the following subsection, whereas quality cuts on track-candidates and such on photon-candidates will be discussed in their respective subsections.

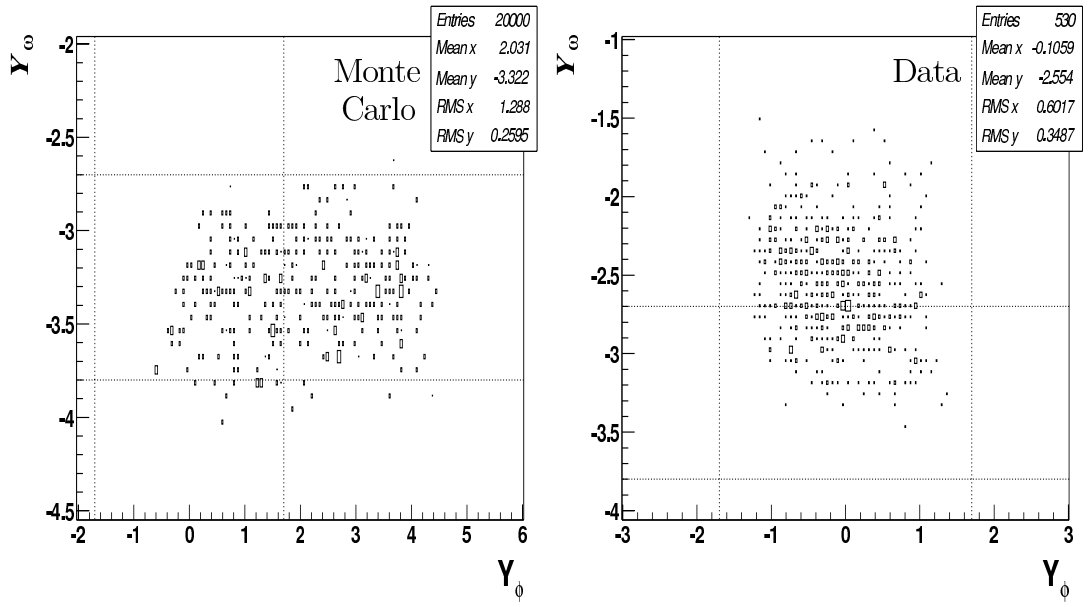

a) b)

Figure 4.7: *Phase-space distribution of ω-ϕ events generated with ToyGen, where no demandments are made for the photons coming from the ω-meson are shown in (a). The finally determined fiducial volume marked in the Y_ϕ-Y_ω-distribution of data is shown in histogram (b). This is the part of data, the cross-section, which has yet to be determined, refers to.*

4.7.1 Run Ranges

Several runs have to be excluded right away, namely those when H1 ran either in 'minimum bias'- or 'shifted vertex' mode. The term 'minimum bias' refers to runs when only a few specific triggers with specific 'minimum bias' conditions are selected. 'In shifted vertex' mode, the nominal vertex is shifted along the z-axis. Hence, the kinematic region which is covered by most detector components is different. The excluded run intervals are thereby

$$200444 < run\# < 201520, \quad 259487 < run\# < 261349 \quad \text{and}$$

$$278687 < run\# < 278978.$$

Furthermore, in 1998 and 1999 a number of runs were performed with electrons instead of positrons. As these runs lead to problems in simulation, they are excluded as well:

$$231721 < run\# < 241650.$$

The more, some of the first runs in 1996 are to be dropped, as the S50 conditions were varied drastically several times. The excluded run period is

$$run\# < 157877.$$

4.7.2 Electron Candidate

To ensure that all events are in the desired kinematic regime of

$$0.3 < y < 0.7 \quad \text{and} \quad \mathrm{Q}^2 < 0.01\,\mathrm{GeV}^2,$$

a cut is applied on the inelasticity y, which is motivated in section 4.5. The requirement on Q^2 is ensured via the geometrical acceptance of the e-tagger.
As explained in 4.5, it is necessary to take care that the shower caused by an electron in e-tagger33 does not get too close to the border of the calorimeter in order to minimize energy losses. To ensure this, a cut on the x-coordinate of the cluster in this calorimeter is performed:

$$|X_{eTag33}| < 6.5\,cm.$$

To get rid of so-called overlap-events, which are events where two ep-interactions take place in one bunch-crossing, two cuts have been applied. Firstly, if one of these two interactions is Bethe-Heitler-like, the scattered electron may look like a photoproduction event in the e-tagger33. To prevent this, a cut on the maximum deposited energy in the photon tagger

$$E_{pTag} < 2\,GeV$$

is implemented. Secondly, if both of these events are created in photoproduction, one electron can be scattered in the e-tagger at 33 m, the other one in the etagger at 44 m. To remove these events, the energy deposited in the e-tagger44 is limited:

$$E_{eTag44} < 5\,GeV.$$

Another variable a cut is applied upon is

$$\Sigma := \sum_i (E - p_z)_i. \tag{4.7}$$

This sum covers all measured particles in the final state. The variable is designed to find out if final state particles which have nothing to do with the proton rest escaped detection. This is of special interest for this analysis, as it aims at an exclusive measurement. Due to energy- and momentum conservation, the relation

$$\Sigma = \Sigma_{final} = \Sigma_{initial} = (E - p_z)_e + (E - p_z)_P = 2 \cdot 27.5\,GeV + 0 = 55\,GeV$$

obviously holds. 55 GeV would hence be the expected value for fully exclusive processes where all particles in the final state are detected.
As the desired events for this analysis consist in the final state exclusively of two charged tracks, three photons, the scattered electron and the proton rest, the latter relation turns into

$$50\,GeV < \sum_{e',\gamma_i,track_i} (E - p_z) < 60\,GeV.$$

The sum does not include the proton rest, since its contribution cancels.

4.7.3 Track Candidates

As most of the criteria for suitable track candidates are requested at preselection level (see subsection 4.2), namely two central tracks meeting various quality criteria, at this stage only two additional conditions are asked for. Firstly

$$q_{track\,\#1} \neq q_{track\,\#2},$$

where q_{track} denotes the charge of a track. This cut is required, as the process this analysis tries to verify implies the decay $\phi \rightarrow K^+ K^-$.
Secondly, the z-coordinate of the vertex has to fulfill

$$-35\,cm < z_{vtx} < 35\,cm.$$

As depicted in figure 5.4 in subsection 5.1.2, this cut affects the data only marginally, as the majority of vertices lies within these boundaries. Nevertheless, this cut ensures dropping events stemming from secondary interactions like for instance collisions of electrons with satellite bunches. These satellite bunches are proton bunches that are separated up to 70 cm in z-direction from the majority of other bunches. This occurs due to mismatches of the proton bunch position in the accelerating cavities.

4.7.4 Photon Candidates

The mesons in backward direction are detected via their decay into photons. To connect the clusters in the electromagnetic section of the SpaCal detector to photon-candidates, i.e. to get rid of clusters that do not originate in photons, several cuts have been applied.
As the examined decay channel of the ω-meson delivers a final state of three photons, the number of clusters clearly has to be three or above:

$$3 < N_{Clusters} < 10.$$

The upper limit has been found empirically (see figure 4.8). No significant improvement could be found when further in- or decreasing this upper limit.
To ensure that the shower caused by an incoming photon is entirely contained in the SpaCal, a distance cut of

$$8\,cm < D_{Cluster} < 75\,cm$$

is performed. $D_{Cluster}$ here denotes the radial distance of the cluster from the beam pipe.
Another condition clusters have to satisfy is a cut on their radius:

$$R_{Cluster} < 3\,cm.$$

As the lateral extensions of hadronic showers are larger than the extensions of electromagnetic showers, this cut serves to get rid of events where hadrons, charged pions basically, cause such showers in the electromagnetic part of SpaCal.
A further condition to suppress background from hadrons is an upper limit on the

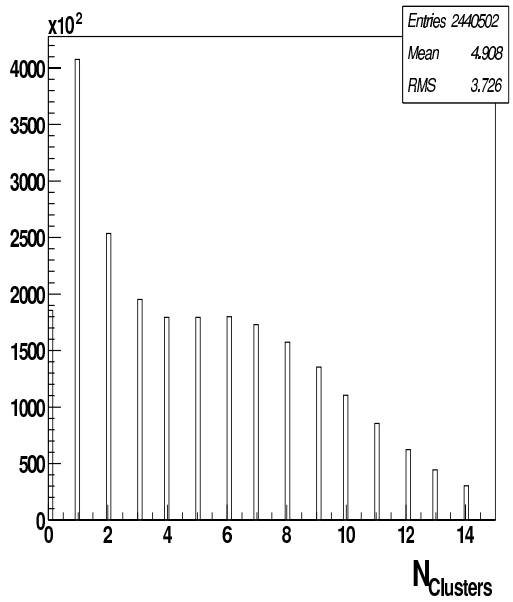

Figure 4.8: *Number of clusters in the electromagnetic section of SpaCal per event before final selection.*

relation energy deposited in the hadronic part of SpaCal to energy deposited in the electromagnetic part:

$$\frac{E_{had}}{E_{em}} < 1\%.$$

Figure 4.9 depicts this ratio. Here, all cuts on the run ranges and the electron candidate besides $E - p_z$ are applied. The cuts on the track- and the photon candidates are not performed. The figure shows that the cut is well justified. It reduces the number of events with hadrons in backward direction, as photons deposit their energy almost entirely in the electromagnetic section. The so-created showers do not reach into the hadronic part of the calorimeter.
As described in 4.3.2, a cut of

$$E_{HC} \geq 2.5\,GeV$$

on the hottest-cluster energy E_{HC} of the electromagnetic section of the SpaCal is performed. This ensures an efficiency of $\approx 100\,\%$ of the SpaCal trigger requirements. If any of the above conditions is violated, the whole event will be discarded. If one of the following two statements is not fulfilled however, only the respective cluster will be removed, whereas the event itself will be kept.
As shown in [43] via testbeams, a threshold of 30 MeV is enough to reject noise clusters. To be on the safe side, the condition used in this analysis was chosen to be

$$E_{Cluster} > 100\,MeV.$$

As the probability for two neighboring cells to fluctuate above the noise threshold is rather low, an effective cut on such noise clusters is

$$N_{cells/cluster} > 1.$$

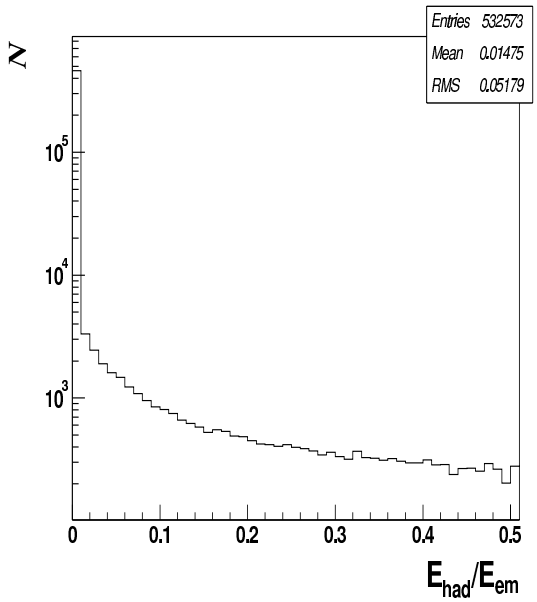

Figure 4.9: *Relation E_{had} to E_{em} of SpaCal-clusters. E_{had} denotes the energy of a cluster deposited in the hadronic part of the SpaCal, E_{em} the energy of the same cluster deposited in the electromagnetic part. One finds that all events with a significantly low ratio are concentrated in the lowest bin which ranges from 0 to 1%.*

This demands that a cluster has to consist of more than one cell (for details on the SpaCal structure refer to 2.2.3). Besides, minimum ionizing particles (mips) usually deposit their energy in merely one cell. Hence, this serves as a cut on clusters caused by mips, too.
Altogether, exactly three clusters need to pass all the quality conditions mentioned above. These are the three required photon candidates.
The next step is to examine whether the event contains a neutral pion π^0. This can be done by calculating the invariant masses of the three two-photon pairs. Such a pair counts as a pion candidate, if

$$|m_{\pi^0} - m_{\gamma\gamma}| \leq 40\,MeV$$

is fulfilled, where $m_{\pi^0} = 135\,\mathrm{MeV}$ hereby is the nominal mass of the neutral pion (see [42]).
Thus, at least one of these three two-photon combinations has to yield a pion candidate:

$$N_{\pi^0} \geq 1.$$

Chapter 5

Results

This chapter finally presents the results on the process this thesis deals with:

$$\gamma p \longrightarrow \omega\phi X.$$

First off, the simulated background (via the PYTHIA event-generator) will be compared to the data. Then, the cross-section will be determined and finally the sources for the most important systematic uncertainties will be discussed.

5.1 Comparison of Monte Carlo Simulated Events and Data

5.1.1 Invariant Mass-Spectra

The histograms in figure 5.1 show the invariant $\gamma\gamma$-mass. All cuts from final selection (see 4.7) have been applied besides the ones on the π^0-mass window and the number of pion-candidates. To the 3γ- and track-track-mass distributions in figures 5.2 and 5.3, all cuts of final selection have been applied.

In the $\gamma\gamma$-mass spectrum, one clearly recognizes the sharp π^0-signal at 135 MeV and the η-peak at 547 MeV (nominal masses). Besides, very good agreement of data and Monte Carlo[1] has to be stated. Both signals, as well as the contributions to the background, are very well described by the Monte Carlo.
One notices in the 3γ-mass spectrum again quite good agreement in general of data and Monte Carlo. Boldly visible is the ω-peak at 783 MeV (nominal mass).
Quite satisfying agreement is achieved for the track-track-mass distribution, too. Most importantly, a clear ϕ-signal cannot be verified in the data. The signal would be expected close to the threshold of $2 \cdot m_{K^{+-}} \approx 988\,\mathrm{MeV}$, thus right at the lower limit of the depicted mass-spectrum, as the nominal ϕ-mass is $\approx 1.02\,\mathrm{GeV}$. This part of the distribution in particular is in very good agreement with PYTHIA.

[1]The term Monte Carlo will be used in this chapter to refer to the events that have been generated with the PYTHIA event generator, as well as to the generator itself.

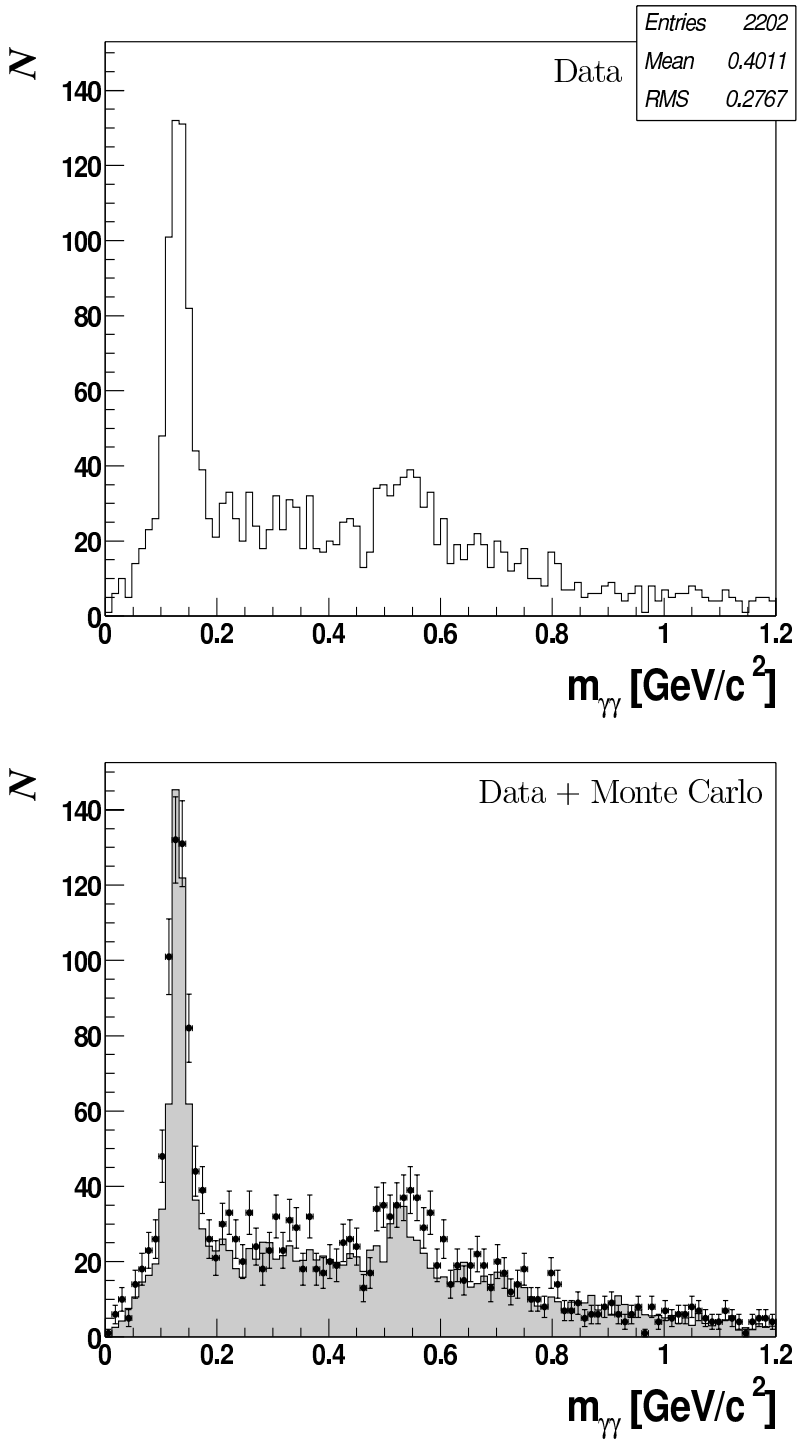

Figure 5.1: *Invariant $\gamma\gamma$-mass spectrum. For better visibility, the upper histogram shows merely the data, whereas the lower histogram compares data to PYTHIA-generated events. The dots with error bars represent the data, the grey histogram shows the distribution of the PYTHIA-events. Event selection and PYTHIA parameters are explained in the respective sections. Clearly visible are the π^0- and the η-signals (nominal masses 135 MeV, 547 MeV respectively).*

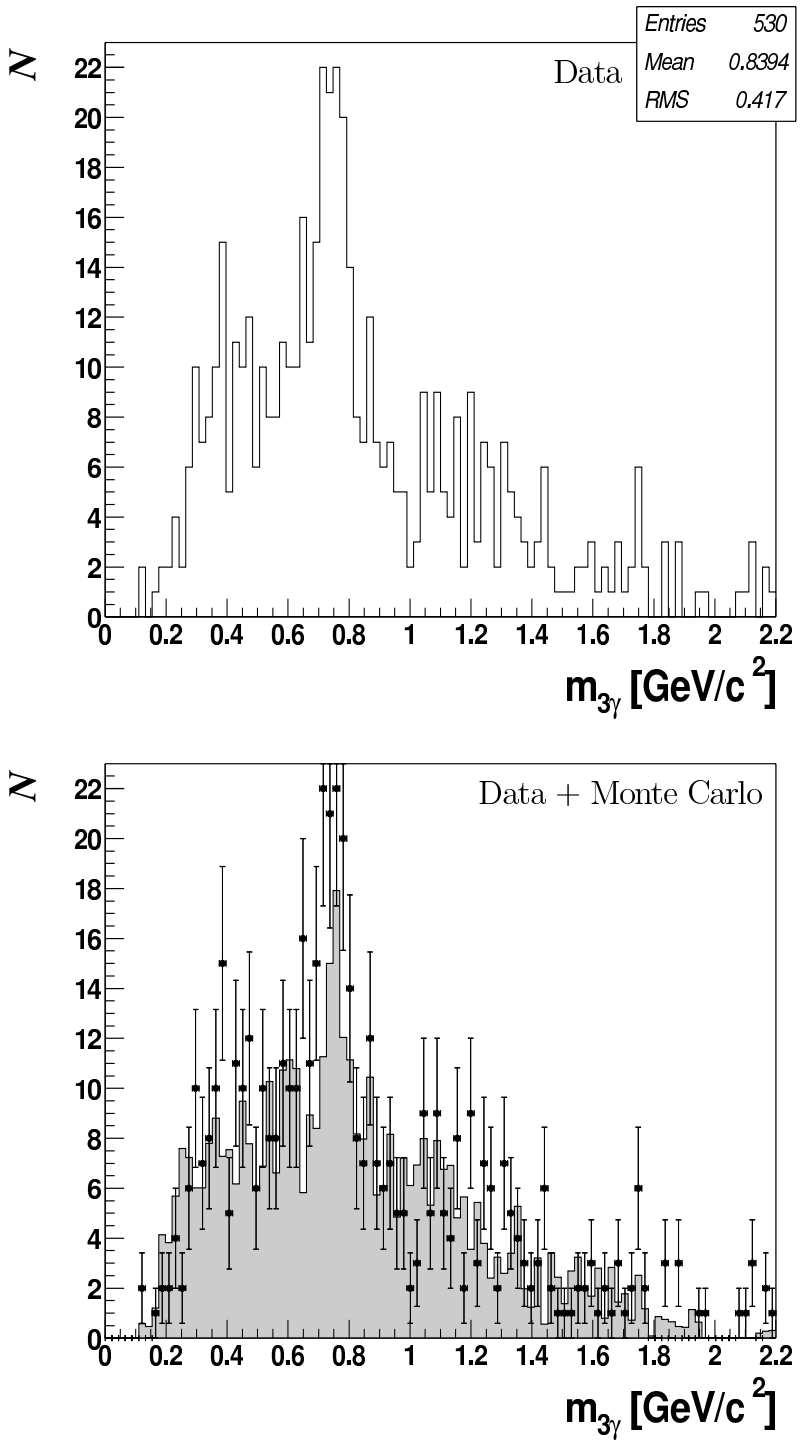

Figure 5.2: *Invariant 3γ-mass spectrum. The labelling is explained in figure 5.1. The ω-signal is well identifiable (nominal mass 783 MeV).*

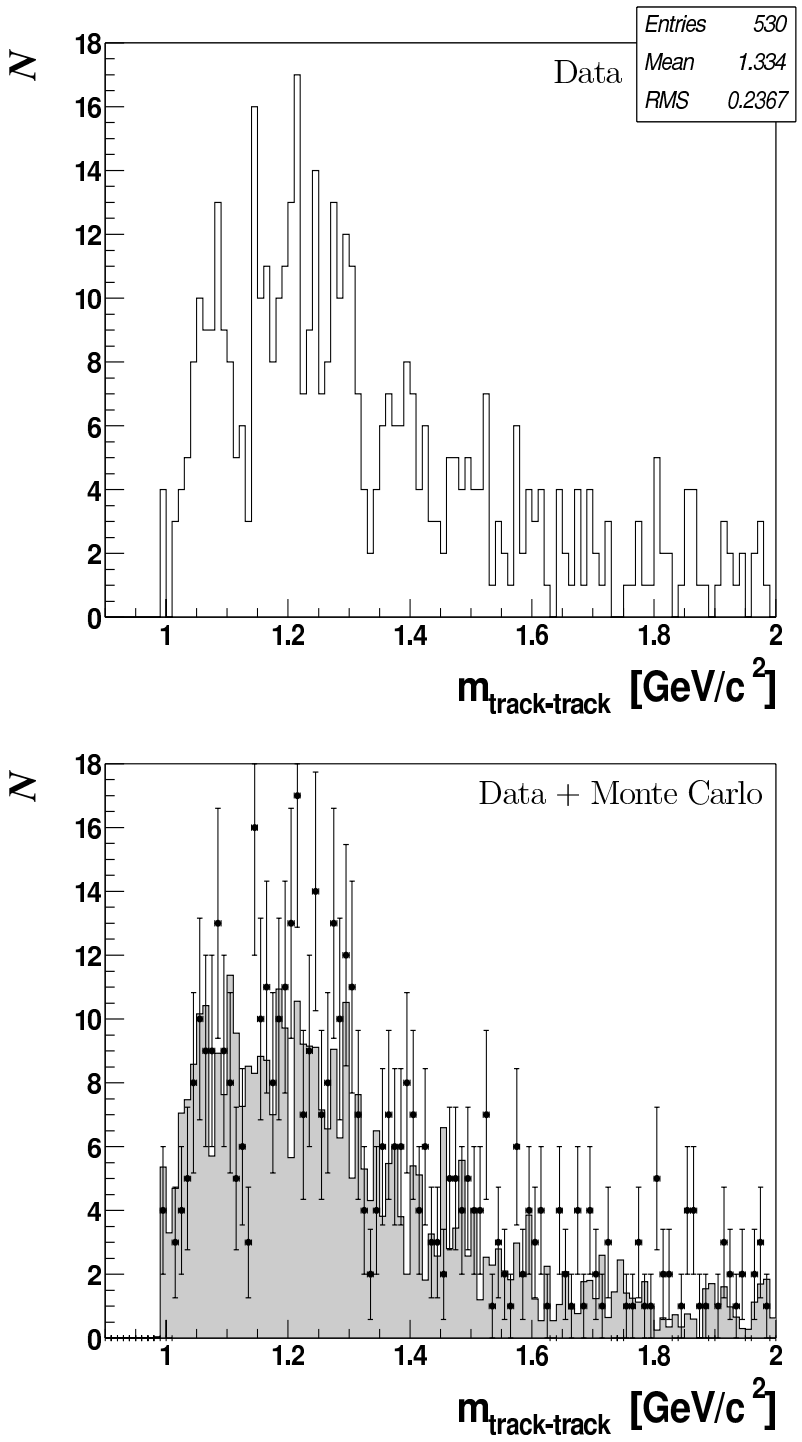

Figure 5.3: *Invariant track-track-mass spectrum. The labelling is explained in figure 5.1. The four-momenta of the two track-candidates, by which the invariant track-track-mass is obtained, are constructed assuming the kaon-hypothesis, i.e. assuming the tracks to originate from kaons. A significant ϕ-signal cannot be seen (nominal mass 1.02 GeV).*

5.1.2 Further Distributions

In figure 5.4, three more representative histograms are presented that support the good consistency of data and Monte Carlo that could already be found when comparing the mass-distributions in the preceding subsection.

Histogram (a) shows the distribution of the energy of clusters in the electromagnetic section of the SpaCal. Applied are the cuts from final selection on the run ranges (see 4.7.1) and the electron candidate (see 4.7.2) except '$E - p_z$'. The cuts on the track- and the photon candidates (see 4.7.3 and 4.7.4) are not performed. Considering the large number of clusters with energies below 125 MeV, i.e. the first bin, one can see how big the fraction of noise clusters is. Therefore, a cut of 100 MeV is performed on this cluster energy (see 4.7.4). The rise at 2.5 GeV occurs due to the trigger threshold that is set at this energy.

The z-coordinate distribution of the interaction vertex is shown in histogram b. Here, all cuts from final selection except '$E - p_z$' and the one on the z_{vertex}-coordinate itself are applied. The small accumulation of entries at the upper end of the data spectrum can be explained by electrons colliding with proton satellite-bunches (see 4.7.3).

Histogram c finally shows the $(E - p_z)$ distribution. All cuts besides the one on $(E - p_z)$ itself are performed. This variable is explained in detail in 1.1. Ideally, i.e. when all particles that are created in an interaction are actually detected and perfectly measured, it is supposed to peak at 55 GeV here. As this is almost the case, data peaks at roughly 54 GeV. This shows that the applied cuts serve well to select data where the complete final state, i.e. all particles, are detected. A slight deviation is noticable however between data and Monte Carlo. This is due to a miscalibration of the SpaCal energy in 1996.

In general, one finds as for the invariant mass-spectra good consistency of data and PYTHIA-generated events.

5.2 Determination of the Cross-Section

The invariant mass-distributions presented in the preceding section do not give evidence for significant ω-ϕ signals. In particular, a ϕ-peak in the invariant track-track mass sample does not show up. Still, one does not know for sure what these events actually are. Conservatively, one can assume that all of such events are in fact signal-events and determine an upper limit on the cross-section thereof. This is done by isolating ω-ϕ candidates. These are events where the ω- and the ϕ-meson lie withing suitable respective mass ranges.

Firstly the mass-constraints on the invariant 3γ-mass will be discussed. In order to meet the 3γ-invariant mass resolution of the SpaCal, a range of 200 MeV around the nominal ω-mass of 782 MeV was assumed. This generous definition ensures that possible ω-candidates are inside the so-defined window. Histograms (a) and (c) in figure 5.5 display the cut.

Secondly, also a reasonable mass-range for the invariant track-track-mass has to be selected. ToyGen (see 3.1) has been used to generate a 'narrow' ϕ. By putting this signal through H1-simulation and -reconstruction, one finds an estimate of the

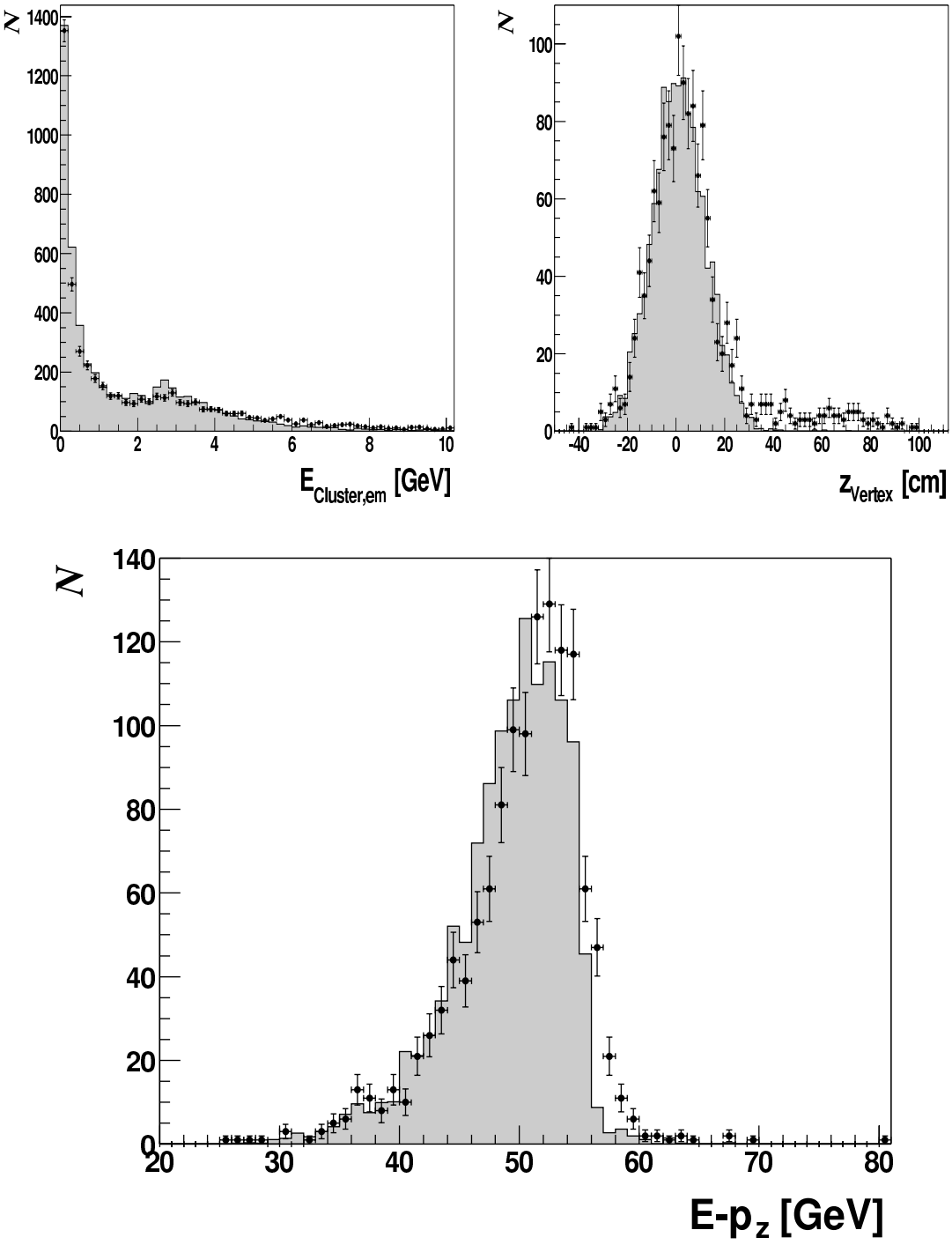

Figure 5.4: *Further control-distributions. Shown are the energy distribution of clusters in the electromagnetic section of the SpaCal, the distribution of the z-coordinate of the interaction vertex and the distibution of the $(E - p_z)$ variable (see 4.7.2 for details on this variable). All quality cuts besides the respective plotted ones have been applied beforehand.*

detector resolution, i.e. the width of the obtained signal, for track-track masses. From these results, the mass window has been fixed from the threshold for K^+K^--production $\approx 2 \cdot m_{K^+-} = 988\,\text{MeV}$ to 1.05 GeV. Histograms (b) and (c) in figure 5.5 illustrate the cut on the track-track-mass.

Applying these two cuts on the respective masses, histogram (d) illustrates the remaining 8 candidates within the mass-window.
An algorithm by Cousins and Feldman [44] has been applied in order to convert these candidates into an upper limit. More precisely, their method determines an interval for the number of signal-events within a given confidence limit. Further explanations and comments on this method are also presented in the appendix of [2].
Assuming now 8 signal candidates and zero background candidates, this method, i.e. tables provided in [44], yields:

$$N_{signal-events} \leq 14\ (95\%\,CL). \tag{5.1}$$

Using this upper limit of 14 events, one can determine an upper limit on the cross-section for the process:

$$\hat{\sigma}(\gamma p \to \omega\phi X) < \frac{N_{max}}{\prod BR_i \cdot F_{\gamma/e} \cdot L_{int} \cdot \prod \varepsilon_i}. \tag{5.2}$$

Here, $\hat{\sigma}$ denotes the cross-section only for the rapidity ranges given in section 4.6, namely $3.8 \leq Y \leq -2.7$ for the ϕ and $-1.7 \leq Y \leq 1.7$ for the ω. This is due to the detector acceptance and the limitations of ToyGen. N_{max} is the maximum number of expected events at a 95% confidence limit as explained above, BR_i are the branching ratios, $F_{\gamma/e}$ is the photon-flux factor (see equation 1.19 in subsection 1.5.2), L_{int} is the integrated luminosity of data passing the S50 subtrigger at levels one and four, and ε_i are the individual efficiencies. The exact values are:

$$\prod BR_i = BR(\phi \to K^+K^-) \cdot BR(\omega \to \pi^0\gamma) \cdot BR(\pi^0 \to \gamma\gamma)$$
$$= 0.492 \cdot 0.087 \cdot 0.988 = 0.042$$
$$\prod \varepsilon_i = \varepsilon_{geom.Acc.} \cdot \varepsilon_{etag.Acc.} = 0.024 \cdot 0.555 = 0.013$$
$$F_{\gamma/e} = 0.0136 \quad , \quad L_{int} = 18.929\,pb^{-1}$$

As explained in 4.3.2, the efficiency of the S50 subtrigger is assumed to be 100 %, after a cut on the hottest cluster. The e-tagger33 acceptance has been averaged over all events that may contribute to the signal-candidates, i.e. all events in histogram (c) in figure 5.5.
The so-determined upper limit on the cross-section is:

$$\hat{\sigma}(\gamma p \to \omega\phi X) < 99.5\,nb\ (95\%\,CL). \tag{5.3}$$

5.3 Systematic Uncertainties

In this section, the sources for the most influential systematic uncertainties and their effect on the upper limit will be considered.

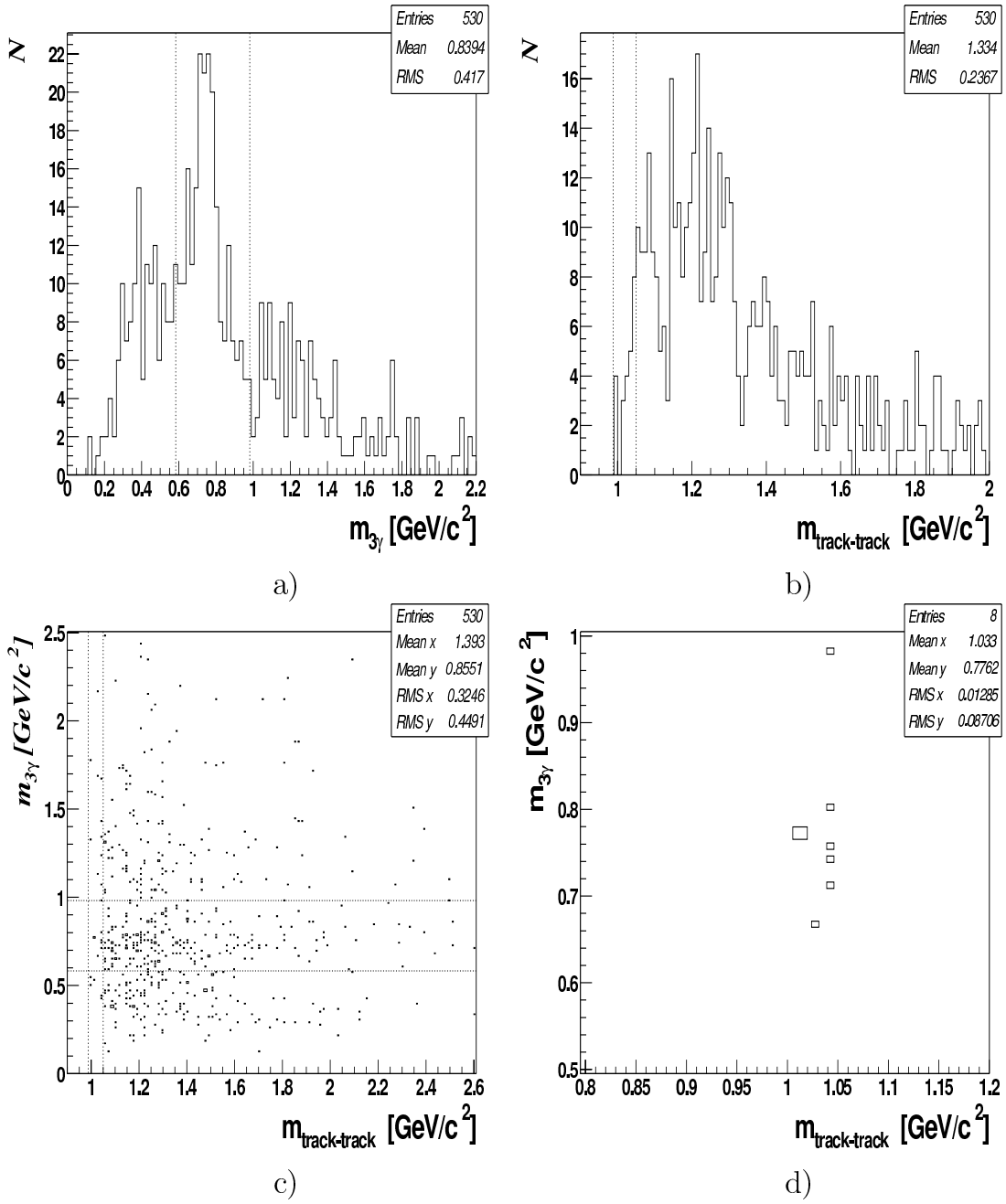

Figure 5.5: *Determination of ω-ϕ-candidates. (a) and (b) show the 3γ-, track-track-mass spectrum respectively. Marked are the applied mass windows for respective candidates. (c) displays both mass spectra simultaneously, (d) the remaining ω-ϕ-candidates after both mass-cuts.*

Cousins and Highland [45] provide a method to incorporate the systematic uncertainties into an upper limit. Again, further explanations can be found in [2]. The formula they derive is

$$\mu_{2sys} = \mu_2 + \frac{\mu_2 + b - N_0}{\mu_2 + b} \cdot \mu_2^2 \sigma_{sys}^2 / 2. \tag{5.4}$$

$\mu_{2\mathrm{sys}}$ hereby denotes the new upper limit for the expected number of events now incorporating the systematic uncertainties, μ_2 is the upper limit without systematics (14 here), b is the number of background events (0 here), N_0 is the number of signal events (8 here) and σ_{sys} denotes the overall systematic uncertainty.
The considered sources for the systematic uncertainty comprise

Central trackers The efficiency of verifying two kaon-tracks by means of the CJC in order to reconstruct a ϕ-candidate is analyzed in [46]. This analysis used data from 1996 to 1999, and the determined uncertainty can hence be considered as a fairly good estimate for this anlysis. The uncertainty on the cross-section is therein denoted as 10 %.

SpaCal and electron tagger The detection efficiency of the SpaCal has been thoroughly studied in [3] and [4]. These two analyses also studied mesons in multi-photon final states, using this calorimeter. The therein considered sources for uncertainties are the same as for this analysis. The given overall uncertainty of 13 % can be considered a good estimate.

Luminosity According to the official H1 luminosity summary table [47], the relative uncertainty on luminosity measurement for the years 1996 to 2000 varied between 1.1 and 1.5 %. An overall systematic uncertainty of 1.5 % will hence be assumed for luminosity measurement.

Added in quadrature, the estimate for the overall systematic uncertainty on the cross-section is 16 %.
Applying this value to equation 5.4, one obtains a new upper limit including systematics of

$$N_{signal-events,sys} \leq 15.06\ (95\%\, CL). \tag{5.5}$$

This converts into an upper limit for the cross-section of

$$\hat{\sigma}_{sys}(\gamma p \to \omega\phi X) < 107.1\, nb\ (95\%\, CL). \tag{5.6}$$

5.4 Improvement of the Upper Limit based on dE/dx-Information

In order to qualitatively judge the 8 event candidates, one can further take into account the available dE/dx-information. The term dE/dx-information relates to the information on energy deposition per length of a charged particle penetrating a drift chamber due to ionization. In this analysis, the dE/dx-analysis tool 'DDXMOD' ([48, 49]) was applied which provides the user with run-corrected dE/dx-data.

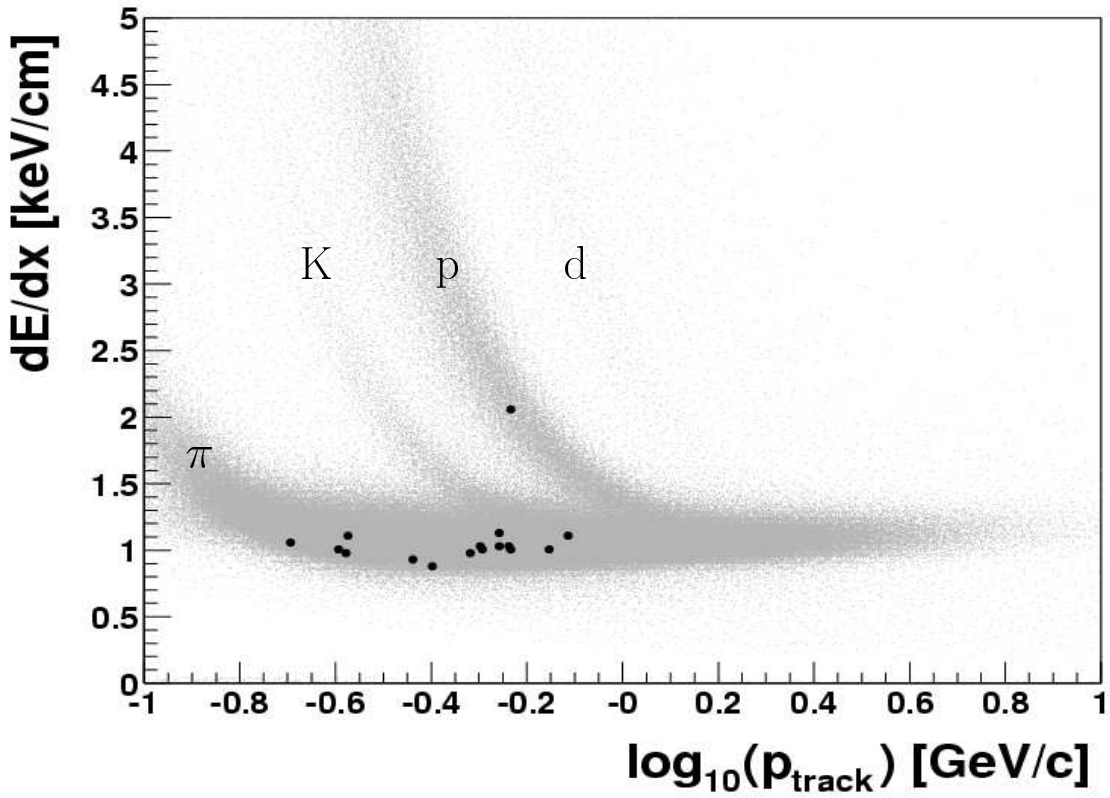

Figure 5.6: *dE/dx-evaluation of event candidates. The distribution of all tracks is indicated grey in the background. The identifiable bands are labelled with the respective particle-abbreviation upon. The 16 tracks belonging to the 8 event-candidates are marked in black.*

Figure 5.6 illustrates these 8 pairs of tracks, hence 16 entries. The distribution of all tracks in the sample is shown as the grey background. For those, no cuts were applied besides the ones at preselection level.
To conclude, the histogram indicates that only a few out of the 16 tracks will be consistent with the kaon-hypothesis. A qualitative estimate for the upper limit on the cross-section including these dE/dx-information is the purpose of this section.
Since the event signature demands two kaon-tracks, it is helpful to further evaluate the position of each pair of tracks individually in such a histogram. This has been done in the figures 5.7 and 5.8.
Now, those histograms where the track pairs are assumed to be inconsistent with the kaon-hypothesis have to be separated. This is merely performed via visual inspection and the result is shown in figure 5.7. In these distributions both track-entries are assumed to be farther than $\approx 2\sigma$ away from the kaon-band. In most events, one or both tracks are even farther than $\approx 3\sigma$ off. This results in a probability $p \lesssim 10^{-3}$ that both tracks originate from kaons. Hence, they will not be taken into account for the cross-section estimate. This qualitative estimate leaves 4 candidates instead of the remaining 8 candidates in 5.2. These 4 candidates are shown in 5.8.
The Cousins- and Feldman-algorithm yields for this case

$$N_{signal-events} \leq 8.6\ (95\%\, CL). \tag{5.7}$$

This results in an upper limit on the cross-section of

$$\hat{\sigma}(\gamma p \rightarrow \omega\phi X) < 61.2\, nb\ (95\%\, CL). \tag{5.8}$$

Including systematics as described in 5.3, the new upper limit on the number of signal events is

$$N_{signal-events,sys} \leq 9.1\ (95\%\, CL). \tag{5.9}$$

This yields an upper limit on the cross-section of

$$\hat{\sigma}_{sys}(\gamma p \rightarrow \omega\phi X) < 64.7\, nb\ (95\%\, CL). \tag{5.10}$$

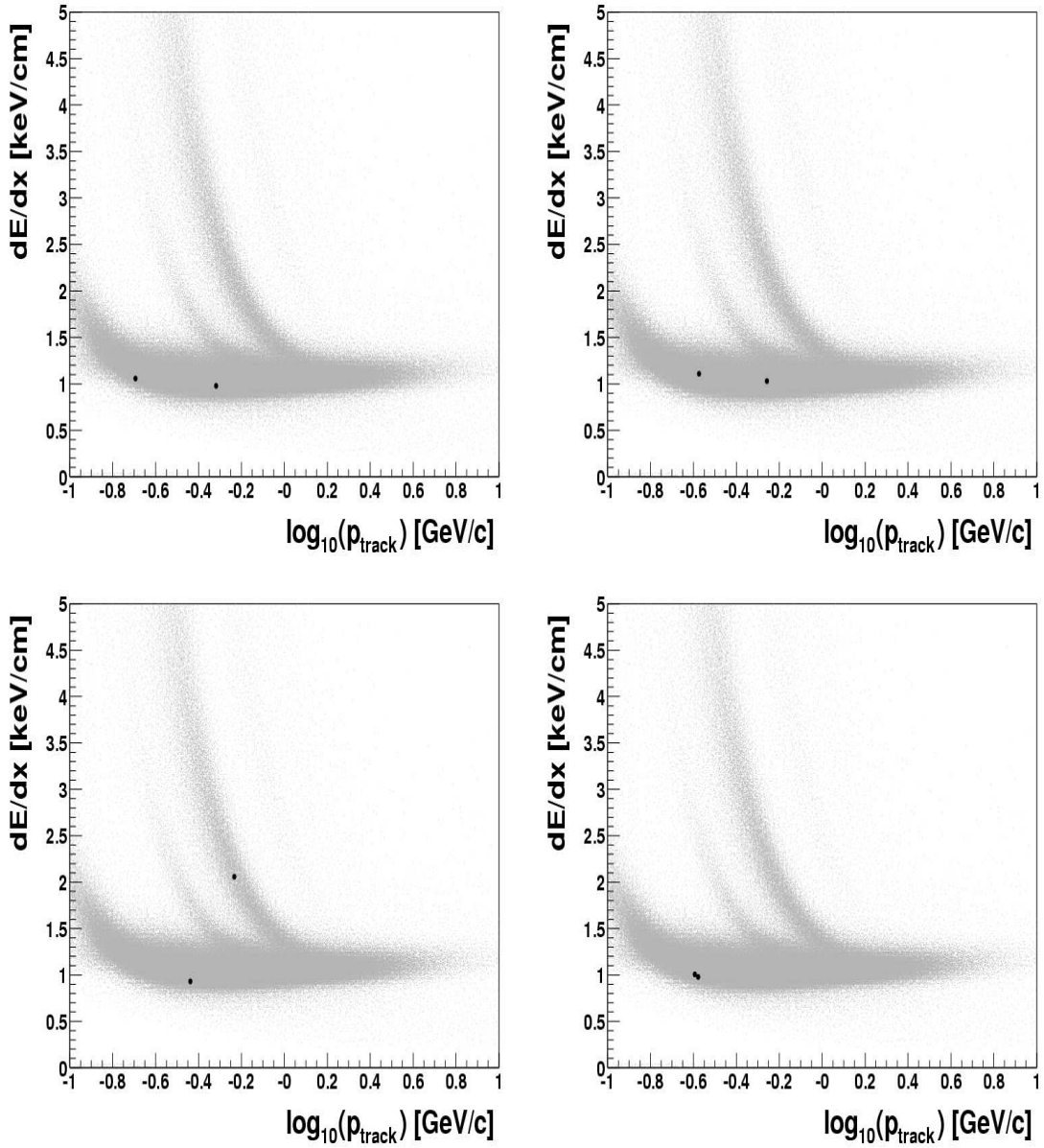

Figure 5.7: *dE/dx-evaluation of track-pairs of event-candidates I. The background in grey as well as the identifiable bands are further explained in figure 5.6. Each histogram represents one event-candidate, the two black marks in the front represent the two tracks per event-candidate. These four event-candidates have been selected by visual inspection to have their track-pairs too far from the K-band in order to be taken into account for this cross-section estimation.*

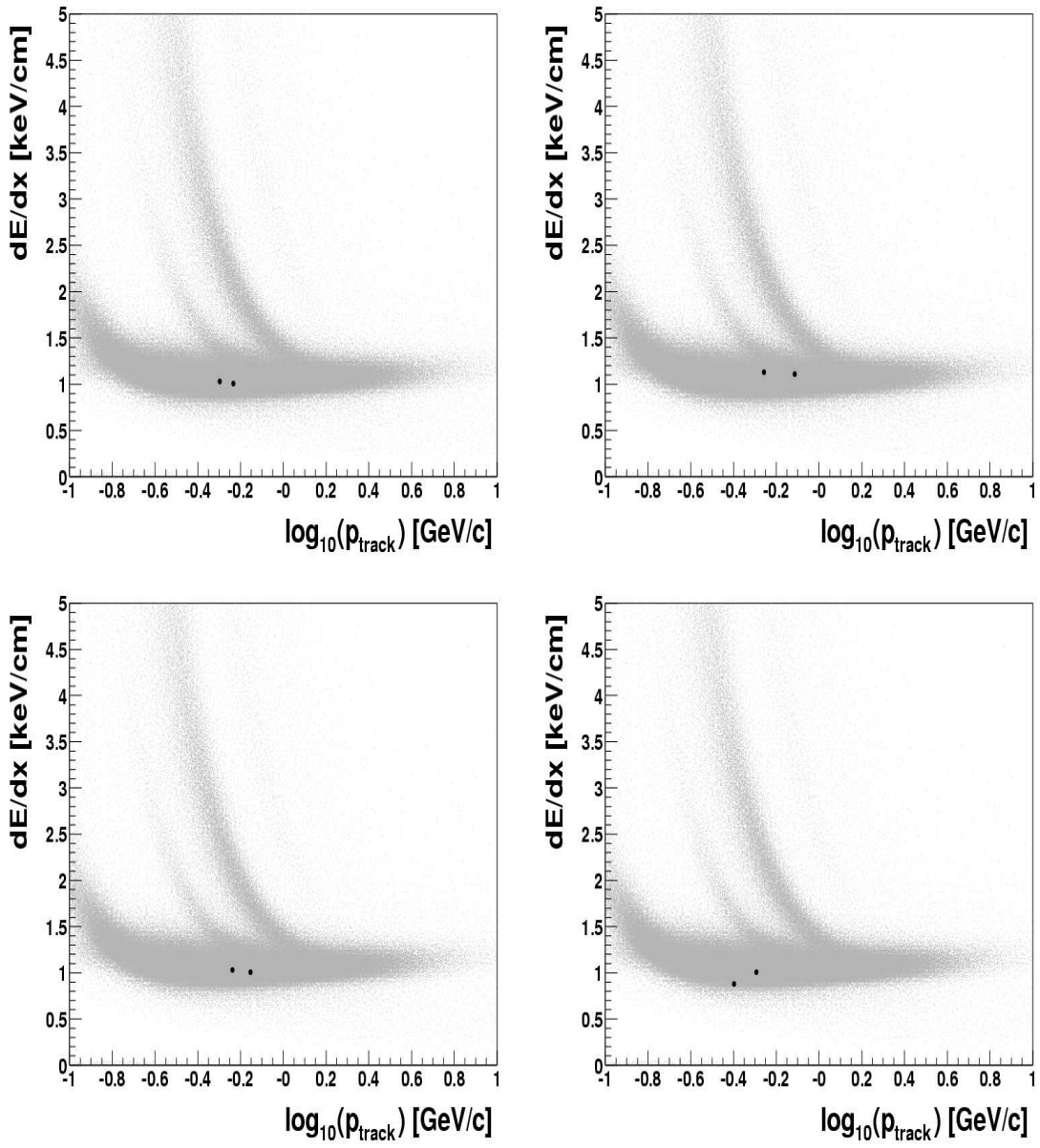

Figure 5.8: *dE/dx-evaluation of track-pairs of event-candidates II. Explanation of the histograms see figure 5.7. These four distributions out of eight show the event-candidates that are assumed to be consistent with the kaon-hypothesis.*

Appendix A

Requirements of Control Triggers for S50

The description below presents the main conditions for the selected control triggers for S50.

1996: S83 `(DCRPh_Tc && zVtx_sig && eTAG) && (!CIP_Backward)`

1996: S84 `(DCRPh_Tc && zVtx_sig && (LU_ET_44 && !LU_PD_low && !LU_WatVet)) && (!CIP_Backward)`

1997: S43 `(DCRPh_Ta && (zVtx_sig>1) && eTAG)`

1999: S85 `(LU_ET && !LU_PD_low)`

2000: S109 `(DCRPh_Ta && zVtx_Cls && !LAr_IF && (LU_ET_44 && !LU_PD_low && !LU_WatVet))`

In the above expressions, '&&' stands for logical 'and' and '!' means negation. The various trigger elements for each subtrigger are explained in the listing below.

`'DCRPh_Tc'` More than three central tracks are demanded. These tracks are compared to certain masks, i.e. patterns, that allow first evaluation. The number of masks that fit is related to the number of detected tracks.

`'zVtx_sig'` Again for central tracks. The hits in the proportional chambers CIP,COP and FPC are projected onto the r-z-plane and connecting lines are calculated. The points where these lines traverse the z-axis is entered in a histogram, the so-called 'z-vertex histogram'. If a central vertex occurs, a peak would be expected in such a distribution. This peak is demanded here with a certain significance.

`'CIP_Backward'` In the above description this condition is negated, hence used as a veto. Only very few tracks are allowed to pass the backward quarter of CIP.

Summarized, the S83 subtrigger goes for events with a central vertex, thus central tracks, and a detected electron in the tagger at 33 m.

`'LU_ET_44'` The energy deposited in the e-tagger at 44 meters is claimed to be above a certain threshold (here $\approx 10\,\mathrm{GeV}$).

`'LU_PD_low'` The energy deposited in the photon detector is demanded to exceed a certain limit (here $\approx 4\,\mathrm{GeV}$). Used as a veto here.

`'LU_WatVet'` This condition concerns the water Cerenkov-counter in front of the photon detector (also see subsection 2.2.5 for further information on the luminosity system). A certain energy threshold has to be exceeded in this Cerenkov-counter to ensure synchroton radiation is kept out of the photon detector and falsifies luminosity measurement. Used as a veto here.

The S84 is again aiming at central tracks, but in contrast to S83 the electron is demanded in the tagger at 44 m.

`'DCRPh_Ta'` Explanation see `'DCRPh_Tc'`, but more than one track is desired here.

`'zVtx_sig>1'` Explanation see `'zVtx_sig'`, but significance is demanded to be higher.

S43 is just like S83 going for central tracks and an electron in e-tagger33.

`'LU_ET'` The deposited energy in the e-tagger33 is requested to be inbetween two limits that are modified from time to time.

This subtrigger S85 demands an electron in the e-tagger at 33 m and very little energy in the photon detector.

`'zVtx_Cls'` Explanation see `'zVtx_sig'`, but all histogram entries are claimed to be within four neighbouring bins, i.e. a narrow peak is demanded. This is the case for low multiplicity events.

`'LAr_IF'` The sum over all transverse energy in the 'inner-forward' part of the Liquid Argon Calorimeter. In the above condition for subtrigger S109 used as a veto, hence such energy deposition must not occur.

S109 fires when low multiplicity events occur with an electron in the tagger at 44 m.

Epilog

During the last couple of years, several attempts to find evidence for the Odderon, the C=P=-1 partner of the Pomeron, at HERA were unsuccessful. Within the H1-group of the Kirchhoff-Institute at the University of Heidelberg, a number of analyses tried so.
O.Nix [1] and T.Golling [2] attempted to find hints for Odderon-induced exclusive photoproduction of π^0-mesons, C.v.Cube [3] and T.Berndt [4] were looking for such contributions in tensor meson production. These analyses determined upper limits on the cross-section which were significantly lower than theoretical predictions made by O.Nachtmann and H.G.Dosch [5, 6].
One possible explanation is that the coupling of the Odderon to the γ-meson vertex is a lot smaller than assumed [51]. This was the starting point for the submitted analysis. The reaction of choice was $\gamma p \to \omega\phi X$, as the above vertex is replaced by the well-known diffractive vertex γ-Pomeron-vector meson. The Odderon couples in turn to the proton and fuses with the Pomeron at a third vertex where also vector mesons could be created. No theoretical predictions have been made so far concerning this process though.
Evidence fo this reaction could not be found in the presented analysis. An upper limit on the cross-section, which refers to the limited phase-space expressed in terms of the laboratory frame rapidity Y ($3.8 \leq \mathrm{Y}_\phi \leq -2.7$ and $-1.7 \leq \mathrm{Y}_\omega \leq 1.7$), has been determined as $\hat{\sigma}(\gamma\mathrm{p} \to \omega\phi\mathrm{X}) < 107.1\,\mathrm{nb}$ (95% CL). It is shown in table A.1 along with the results of the preceding analyses mentioned above and the respective theoretical predictions. One finds that the result of this analysis is about in the

channel	limit [nb] (95% CL)	prediction [nb]
$\gamma p \to f_2 X$	12	21
$\gamma p \to a_2^0 X$	62	190
$\gamma p \to \pi^0 N^*$	74	200
$\gamma p \to \omega\phi X$	107	-

Table A.1: *Results of preceding and the present analysis and theoretical predictions.*

same order of magnitude as the other results.
One possibility to compare the obtained result to some reference figure, though, is to consider cross-sections from double-Pomeron exchange. Since Pomeron and Odderon are expected to have the same properties (besides their C- and P-parity),

one could roughly compare the order of magnitude of the upper limit derived in this analysis with a cross-section determined in double-Pomeron fusion in pp-collisions. This cross-section, provided in [50] and scaled down by a factor of ≈ 100 in order to account for the photoproduction process at HERA, is 79 nb. Hence, the limit on Pomeron-Odderon fusion is still of the same order of magnitude as expected in double-Pomeron exchange reactions in photoproduction at HERA.
Of course it is desirable to extrapolate the cross-section to the full phase-space that is available for this reaction. A very rough estimate can be done using ToyGen [35] with its standard parameters. It delivers $\sigma \approx 300\,\text{nb}$.
A possibility to further evaluate the remaining event-candidates presented in chapter 5 is to extend the use of the dE/dx-information. Instead of judging these event candidates via visual inspection, one could apply methods to judge them quantitatively and thus possibly improve the upper limit on the cross-section.
Possible next steps in order to further examine Odderon contributions in diffractive events at H1 would certainly involve reactions with bigger cross-sections. A possible reaction would be $\gamma p \rightarrow \rho^0 \phi X$. Firstly, the coupling of the photon to the ρ^0-vector meson is a factor 10 bigger compared to the ω. Secondly, this analysis detects only the decay photons of the ω-meson. This channel has a branching ratio of merely 8 %. The ρ^0 however decays predominantly into two pions. A technical problem would certainly be the detection of these two hadrons in the SpaCal. This hasn't been performed so far and would clearly necessitate pioneering work in backward calorimetry at H1.

Bibliography

[1] O.Nix, "Suche nach odderoninduzierten Beiträgen in exklusiver π^0-Produktion mit dem Detektor H1 bei HERA", Dissertation, University of Heidelberg (2001)

[2] T.Golling, "Search for Odderon Induced Contributions to Exclusive π^0 Photoproduction at HERA", Diploma Thesis, University of Heidelberg (2001)

[3] Ch.v.Cube, "Untersuchungen zur exklusiven Photoproduktion der Mesonen $b_1(1235)$ und $a_2(1320)$ in Multi-Photon-Endzuständen bei HERA", Diploma Thesis, University of Heidelberg (2001)

[4] T.Berndt, "Exclusive Pomeron- and Odderon Induced Photoproduction of ω and f_2 Mesons at HERA", Dissertation, University of Heidelberg (2002)

[5] E.Berger et al., Eur. Phys. J. **C9** (1999) 491

[6] E.Berger et al., Eur. Phys. J. **C14** (2000) 673

[7] T.Regge, Nuov. Cim. **14** (1959) 951

[8] P.D.B.Collins, "An introduction to Regge theory and high energy physics", Cambridge (1977)

[9] T.Regge, Nuov. Cim. **18** (1960) 947

[10] K.Goulianos, Phys. Rep. **101** (1983) 169

[11] A.Donnachie and P.V.Landshoff, Phys. Lett. **296** (1992) 227

[12] WA91-Collab., S.Abatzis et al., Phys. Lett. **B324**, (1994) 509

[13] A.Levy, "Low-x physics at HERA", DESY-97-013 (1997)

[14] L.Lukaszuk, B.Nicolescu, Lett. Nuov. Cim. **8** (1973) 405

[15] J.J.Sakurai, Phys. Rev. Lett. **22** (1969) 981

[16] S.V.Levonian, "Soft Interactions and Diffraction Phenomena", H1-11/96-504 (1996)

[17] H1-Collab., S.Aid et al., Z. Phys. **C69** (1995) 27

[18] C.W.von Weizsäcker, Z. Phys **88** (1934) 612

[19] E.J.Williams, Phys. Rev. **45** (1934) 729

[20] V.M.Budnev et al., Phys. Rep. **C15** (1975) 181

[21] HERA, "A proposal for a large Electron-Proton Colliding Beam Facility at DESY" (1981)

[22] H1 Collab., "The H1 Detector at HERA", DESY internal report H1-96-01 (1996)

[23] H1 Collab., I.Abt et al., Nucl. Instr. Meth. **A386** (1997) 310

[24] The H1 Spacal Group, R.D.Appuhn at al., Nucl, Instr. Meth. **A382** (1996) 395

[25] The H1 Spacal Group, R.D.Appuhn at al., Nucl, Instr. Meth. **A386** (1996) 397

[26] The H1 Spacal Group, T.Nicholls et al., Nucl. Instr. Meth. **A374** (1996) 149

[27] K.L.Hewitt, "The Detection and Triggering of Forward Muons using the H1 Detector", Diploma Thesis, University of Birmingham (1996)

[28] B.List, "Diffraktive J/ψ-Produktion in Elektron-Proton-Stößen am Speicherring HERA", Diploma Thesis, University of Berlin (1993)

[29] J.C.Bizot et al., "Status of Simulation for a Topological Level 2 Trigger", H1-02/92-212, DESY (1992)

[30] B.Müller, J.Reinhardt, M.T.Strickland, "Physics of Neural Networks", Springer, Berlin (1990)

[31] R.Hecht-Nielsen, "Neuro-Computing", Addison-Wesley (1991)

[32] A.Zell, "Simulation Neuronaler Netze", Addison-Wesley (1994)

[33] J.Meyer (ed.), "Guide to the Simulation Program H1SIM", H1 Software Notes 03-11/89

[34] R.Brun et al., "GEANT Long Writeup", CERN Program Library **W5013** (1994)

[35] T.Berndt, "ToyGen V 2.0", unpublished (2003)

[36] P.Bruni, G.Ingelman, "Diffractive Hard Scattering at e p and p Anti-p Colliders", DESY 93-187

[37] P.Bruni, G.Ingelman, "Diffractively Produced Hadronic Final States And The Pomeron Structure", TSL-ISV-92-0059

[38] UA8 Collab., A.Brandt et al., Eur. Phys. J. **C25** (2002) 361

[39] T.Berndt, "Notes on Double Diffractive Exchange at HERA and Elsewhere", (2003) unpublished

[40] T.Sjöstrand, Comp. Phys. Comm. **39** (1986) 347

[41] T.Sjöstrand, M.Bengtsson, Comp. Phys. Comm. **43** (1987) 367

[42] Particle Data Group, K.Hagiwara et al., Phys. Rev. **D66** (2002) 10001-1

[43] V.Boudry et al., "The Inclusive Electron Trigger for the SpaCal: Design and CERN-Test Results", H1-IN-430(03/1995) (1995)

[44] R.D.Cousins and G.J.Feldman, Phys. Rev. **D57** (1998) 3873

[45] R.D.Cousins and V.L.Highland, Nucl. Instr. Meth. **A320** (1992) 331

[46] S.Udluft, "Protondissoziative Photoproduktion von ϕ-Mesonen am H1-Experiment bei HERA", Dissertation, University of Munich (2000)

[47] "http://www-h1.desy.de/h1det/lumi/summary_tables/summary.html", Official H1-luminosity system homepage

[48] J.Steinhart, "Measurement of the Total $\bar{c}c$-Photoproduction Cross-Section by the Reconstruction of Λ_c-Baryons Using the Improved dE/dx-Particle Identification at the H1 Experiment at HERA", Dissertation, University of Hamburg (1999)

[49] "https://www-h1.desy.de/icas/Ddxmod/ddxmod_h1/ddxmod.html", DEDXMOD official homepage

[50] A.Breakstone et al., Z. Phys. **C48** (1990) 569

[51] H1 Collab., C.Adloff et al., Phys. Lett. **B544** (2000) 35

Acknowledgement

The last page of this thesis is dedicated to all those who contributed to the successful completion of this thesis. I would like to mention in particular

- Prof. Karlheinz Meier, who offered me the opportunity to work on this challenging topic. His steady belief in the success of the searches that have been, are and hopefully will be performed in this group, absolutely was a motivation.
- Prof. Hans-Christian Schultz-Coulon. His help for the past few months, especially for the past few days (...), was indispensable (even though his belief in these kind of quests might no be as 'unshakable' as ours...).
- Juergen Stiewe. His steady help throughout the past 12 months definitely are a major reason this analysis was led to a successful end. I can't cherish enough him spending his vacation in the office to help me with last-minute issues.
- Tommy Berndt for getting me started during the first months. Without his efforts to teach me (almost) all i needed in almost no time, much wouldn't have been possible.
- Filip Tomasz for spending hours on the phone answering my questions.
- Katja Krueger and Victor Lendermann. Their help for the recent months clearly helped to overcome some major obstacles on my way to the upper-limit ... Many thanks to Katja for reading over my chapters in no time!
- my family. Thanks for anything!